THEORY OF PHOTOCURRENTS IN TOPOLOGICAL INSULATORS

im Fachbereich Physik
der Freien Universität Berlin
eingereichte

DISSERTATION

von

ALEXANDRA JUNCK

Berlin, März 2015

ABSTRACT

Topological insulators constitute a new quantum phase of matter that is characterized by a band gap in the bulk, just like an ordinary insulator, but hosts gapless states on its surface. Illuminating a topological insulator by light is expected to lead to a unique current response due to the helical nature of the surface states. Such photocurrents flowing on the surface of a topological insulator will be spin-polarized and the ability to induce and control spin-polarized currents might make topological insulators valuable materials for spintronic devices. The surface photocurrent response would also be a tool for studying the dynamical properties of the topological surface states.

In this thesis, we investigate the theory of photocurrent generation and relaxation in topological insulators. We first study photocurrent generation within a pure surface state model and find that minimal coupling between light and electrons leads to a vanishing photocurrent. For a finite photocurrent one has to consider the small Zeeman coupling between the light and the electron spin.

Photocurrents on the surface of 3D topological insulators have been experimentally observed using laser energies larger than the bulk band gap. We thus extend our pure surface model and include the low-energy bulk states to account for excitations involving the surface Dirac cone and the bulk. We indeed find that photoinduced transitions between surface and bulk states can lead to a photocurrent which is several orders of magnitude larger than the effect in the pure surface model.

We also investigate photocurrent relaxation by carrier-carrier scattering. While such scattering processes cannot relax current in quadratically dispersing systems, they do affect the current in the linearly dispersing surface states. We study the limit of a single particle-hole pair and analyze how scattering affects the individual electron and hole contributions to the current. We find that the effect of carrier-carrier scattering on the individual electron and hole currents strongly depends on the position of the Fermi level, even leading to an amplification of the electron current for positive Fermi energy. This results in a suppression of the relaxation of photocurrents carried by electron-hole pairs.

ZUSAMMENFASSUNG

Topologische Isolatoren beschreiben eine neue Phase der Materie, welche eine Bandlücke im Volumen, an der Oberfläche jedoch metallische Zustände aufweist. Bestrahlt man einen topologischen Isolator mit Licht, erwartet man, dass die helikalen Oberflächenzustände zu einzigartigen Photoströmen führen. Photoströme auf der Oberfläche sind spinpolarisiert. Die Möglichkeit spinpolarisierte Ströme zu kontrollieren könnte topologische Isolatoren zu wertvollen Materialien für Spintronikanwendungen machen. Außerdem ließe sich mit Photoströmen die dynamischen Eigenschaften von topologischen Isolatoren untersuchen.

In der vorliegenden Arbeit untersuchen wir die Theorie der Anregung und Relaxation von Photoströmen in topologischen Isolatoren. Zuerst untersuchen wir die Anregung von Photoströmen in einem Modell nur für die Oberflächenzustände und finden, dass die minimale Kopplung zwischen Licht und Elektronen zu keinem Strom führt, sondern man die kleine Zeeman-Kopplung betrachten muss.

Photoströme wurden experimentell auf der Oberfläche von topologischen Isolatoren mit Laserenergien gemessen, welche die Bandlücke übersteigen. Wir erweitern daher unser Modell und betrachten zusätzlich die niederenergetischen Volumenzustände. Wir finden, dass Übergänge zwischen Volumen- und Oberflächenzuständen durch Photonenabsorption zu Photoströmen führen können, welche die Ströme im reinen Oberflächenmodell um mehrere Größenordnungen übersteigen.

Schließlich betrachten wir die Relaxation von Photoströmen durch Elektron-Elektron Streuung. Während Strom in Systemen mit quadratischer Dispersion durch solche Streuprozesse nicht relaxiert, wird Strom in den Dirac-Oberflächenzuständen davon beeinflusst. Wir untersuchen ein einzelnes angeregtes Elektron-Loch-Paar und analysieren, wie sich Streuprozesse auf den Elektronen- und Lochstrom auswirken. Wir zeigen, dass die einzelnen Effekte stark von der Fermienergie abhängen und der Elektronenstrom sich für positive Fermienergie sogar erhöht. Die Relaxation des Photostroms, der durch ein Elektron-Loch-Paar produziert wird, ist dadurch stark verlangsamt.

CONTENTS

INTRODUCTION

Discovering and understanding different phases of matter is one of the main principles of condensed matter physics. Two phases that we know from everyday life are, e.g., the liquid and solid phases of water. Landau's paradigm states that different phases of matter can be characterized by their broken symmetries. In the case of liquid and solid water, the liquid phase exhibits rotational symmetry when looking at the arrangement of atoms and molecules. An observer can rotate the system by any angle and the arrangement will look the same. The ice crystals of the solid phase, however, break this symmetry. The crystal structure is only invariant under rotations by specific angles, i.e., a multiple of 60 degrees.

The discovery of the quantum Hall effect [von Klitzing et al., 1980], led to the understanding that there are phases of matter that cannot be distinguished by a breaking of the underlying symmetry but instead by their topological order. The quantum Hall effect occurs in electronic systems that are confined to two dimensions and subject to a strong perpendicular magnetic field. Electrons are forced onto cyclotron orbits and the band structure is characterized by quantized Landau levels. These Landau levels are macroscopically degenerate and increasing the magnetic field increases the number of electronic states hosted by a single Landau level. An energy gap between the highest occupied and lowest unoccupied level occurs, just like in an ordinary insulator, when a certain number of Landau levels is filled and the rest are empty. This quantum Hall insulator (QHI) is, however, very different from a normal insulator. Applying an external electric field leads to drifting cyclotron orbits and a finite and quantized Hall conductivity $\sigma_{xy} = ne^2/h$ with integer n.

This remarkable quantization of the Hall conductivity can be understood in terms of Laughlin's argument [Laughlin, 1981]. Consider a quantum Hall sam-
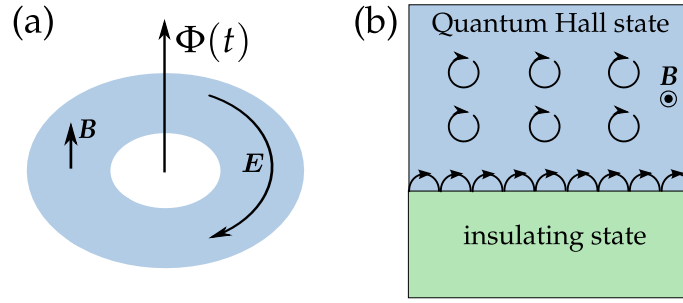
Figure 1.1: (a) Illustration of Laughlin's argument for the quantization of the Hall conductivity. Consider a quantum Hall sample in the geometry of an annulus with a perpendicular magnetic field B. An additional magnetic flux Φ is threaded trough the loop and varied in time. Laughlin argued that if the flux is changed adiabatically by a flux quantum h/e then an integer number of charges will be pumped across the annulus explaining the quantization of the Hall conductivity. (b) The perpendicular magnetic field forces the electrons onto cyclotron orbits inside the quantum Hall sample. At the edge between the QHI and a normal insulator the electrons perform skipping orbits, moving in one direction only.

ple in the geometry of an annulus with a uniform magnetic field everywhere perpendicular to the surface as illustrated in Fig. 1.1 (a). Now think of an additional magnetic flux threading the hole of the loop. If we vary this flux in time, we generate an electromotive force $\mathcal{E} = -d\Phi/dt$ and a corresponding electric field E around the circumference of the loop by Faraday's law. By the classical Hall effect, this produces a charge current along the radial direction. A change of Φ by one flux quantum h/e, however, maps the Hamiltonian of the system onto itself due to gauge invariance, requiring the transfer of an integer number of electrons across the annulus. Microscopically, the flux change shifts the individual wavefunctions such that, for n occupied Landau levels, n states at one edge are pushed above the Fermi energy while n states at the other edge are pushed below the Fermi energy. Since an adiabatic change of the flux cannot lead to excitations across the gap, thermal equilibrium is restored by transporting n electrons across the annulus. Since by this argument always an integer number of electrons is transferred from one edge to the other, the Hall conductivity is quantized. This argument was extended by Halperin [1982] who showed that quantum Hall systems exhibit one dimensional (1D) current-carrying edge states. Classically this can be understood within the cyclotron orbit picture where electrons at the edge perform skipping orbits and move along an edge as illustrated in Fig. 1.1 (b). Since electrons in a particular edge can move in one direction only,
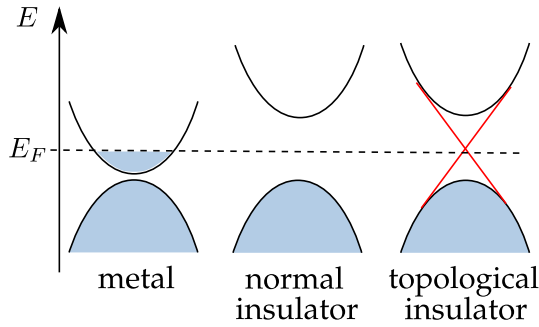
Figure 1.2: Band structure of a metal, an insulator, and a TI. In the case of a metal, the Fermi energy lies in the conduction band while in the case of an insulator the Fermi energy lies in the gap between valence and conduction band. A TI is characterized by a bulk band gap as in the insulator, and gapless metallic surface states that traverse the bulk gap (red lines).

they are insensitive to scattering by impurities explaining the perfectly quantized Hall conductivity.

These edge states at the sample boundary are a necessary consequence of the distinct topological orders of the quantum Hall system and a normal insulator. The number n describing the quantized Hall conductivity can actually be interpreted as a topological invariant, called a Chern number, which by definition is an integer. While for the quantum Hall system $n = 1, 2, 3, \ldots$ depending on the number of filled Landau levels, an ordinary insulator is characterized by $n = 0$. In the absence of a gap closing, the QHI cannot be turned into a normal insulating state by smooth deformations of the system parameters. Thus, at the boundary where the Chern number changes, the gap has to close leading to gapless topologically protected edge states.

1.1 DISCOVERY OF 2D AND 3D TOPOLOGICAL INSULATORS

The discovery of the integer quantum Hall effect in 1980 [von Klitzing et al., 1980] provided an example that a bulk band gap does not necessarily lead to an insulating state. This effect, however, requires the application of a strong magnetic field and a motivation for studying TIs was the question whether such a quantum Hall state could be induced in systems without a macroscopic magnetic field [Haldane, 1988]. Indeed, TIs constitute a new topological phase of matter which is induced by spin-orbit coupling and does not require an external

magnetic field. TIs are insulators in the sense that they exhibit a bulk band gap between the highest occupied and lowest empty band prohibiting the movement of charges in the bulk. On their surface (or edge in two dimensions), however, TIs have gapless metallic states similar to the edge states in the quantum Hall system [see Fig. 1.2].

A first example of such a phase in two dimensions was predicted in 2005. Kane and Mele [2005] proposed that spin-orbit coupling, if sufficiently strong, could induce a quantum spin Hall (QSH) effect in graphene without any external magnetic field. The QSH state is considered to be the first 2D TI that was understood [Moore, 2010]. This state is characterized by a bulk band gap in combination with conducting edge states that traverse the gap. The gapless edge states are spin-filtered, i.e., electrons with opposite spin propagate in opposite directions as illustrated in Fig. 1.3 (a). These edge states can be understood by an extension of Laughlin's argument given above. If spin is conserved, an adiabatic change of Φ by one flux quantum h/e [cf. Fig. 1.1 (a)] transports a spin $\hbar$ across the annulus. An adiabatic change in the flux, however, cannot excite a particle across the bulk band gap leading to the conclusion that there have to be gapless edge states [Kane and Mele, 2005]. If spin is not conserved, Laughlin's argument does not hold but edge states can nevertheless still exist. When time-reversal symmetry is preserved, the states in the same edge are Kramers pairs, i.e., a state and its time reversed. As long as time reversal symmetry is preserved, Kramers degeneracy ensures the crossing of the energy states at special points in the Brillouin zone, i.e., at the time-reversal invariant momenta (TRIM) such as $k = 0$. For an even number of Kramers pairs at one edge, the states can hybridize pairwise and form an energy gap as illustrated in Fig. 1.3 (b). For an odd number of Kramers pairs, however, even if perturbations induce hybridization, a single Kramers pair will always be left as long as the gap does not close [cf. Fig. 1.3 (c)]. For an odd number of Kramers pairs, the band structure can thus not be deformed adiabatically into that of a trivial insulator without closing the gap and the edge states are topologically protected. Elastic backscattering between the states in the same edge, i.e., between Kramers pairs, is prohibited and therefore electrons in edge states are insensitive to scattering from impurities.[1]

Physically, the nontrivial topology which leads to the edge states is based on the occurrence of a band inversion and the topological protection of the edge states can also be understood within the framework of the band theory of solids [Bloch, 1929]. A normal insulator exhibits a band gap between the highest occupied and

---

[1] Electron interactions can, in general, lead to inelastic backscattering and thus to a finite conductivity.
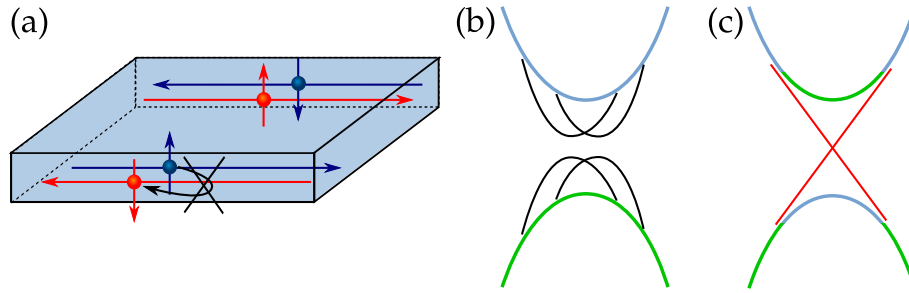
Figure 1.3: (a) Schematic illustration of a QSH insulator with topologically protected edge states. Electrons in the same edge but with opposite spin move in opposite directions. In the other edge the directions are reversed. As long as time-reversal symmetry is preserved, elastic backscattering between electrons in one edge is forbidden. (b) An even number of Kramers pairs in one edge can can hybridize leading to a trivial insulator state. (c) For an odd number of Kramers pairs a single gapless edge state will remain leading to a topologically nontrivial state. Physically this is connected to the occurrence of a band inversion.

lowest unoccupied state. In TI materials strong spin-orbit coupling can shift the energy bands such that there is a level crossing in the low-energy band structure leading to an inverted energy gap as illustrated in Fig. 1.4. If this band inversion occurs between conduction and valence band-edge states with opposite parity, it can lead to a TI phase that is topologically distinct from a normal insulator. This distinction is characterized by a Z_2 topological invariant which, in an inversion symmetric system, is related to the product of the parity eigenvalues of Kramers pairs of occupied bands at the TRIM [Fu and Kane, 2007]. A band inversion between states of opposite parity then indicates a change in the topological Z_2 invariant. As long as time-reversal symmetry is not broken, continuous deformations of the system parameters cannot turn a TI into a normal insulator without closing the energy gap. Thus, at the interface between a TI and a trivial insulator where the topological order changes, there have to be gapless modes. These gapless edge states (or surface states in three dimensions) are then protected by time-reversal symmetry.

The experimental observation of this new state of matter proved difficult at first. It was found that graphene has only very weak spin-orbit coupling [Yao et al., 2007; Huertas-Hernando et al., 2006; Min et al., 2006] resulting in a band gap which was too small to support observable TI behavior. Soon after, however, it was theoretically predicted [Bernevig et al., 2006] and experimentally observed [König et al., 2007] that 2D TIs can be realized in (Hg,Cd)Te quantum wells. In this system, a quantum phase transition occurs as a function of quantum well
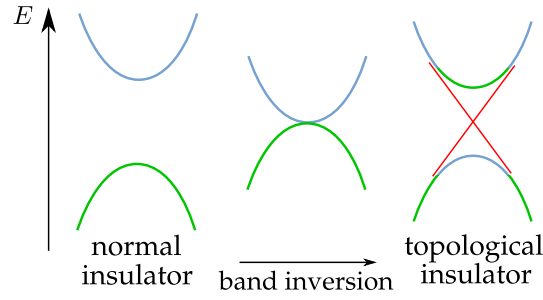
Figure 1.4: Schematic illustration of the band inversion that leads to topologically protected surface states (red). Initially the system is in a normal insulator state. In TIs strong spin-orbit coupling can induce a level shifting that leads to an inversion of the energy bands. As long as time reversal symmetry is preserved, the band structure of a 3D TI cannot be continuously deformed into that of a normal insulator without closing the energy gap.

thickness d_{QW}. For d_{QW} smaller than a critical thickness the system would exhibit trivial insulator behavior. For d_{QW} larger than a critical thickness, however, a band inversion occurs leading to a time-reversal invariant bulk insulating state with topologically protected edge states. The system would be a QSH insulator with a single pair of helical edge states.

Around the same time, topological insulators were theoretically predicted to also exist in three dimensions [Fu and Kane, 2007] and experimentally observed in $Bi_x Sb_{1-x}$ in an angle resolved photoemission spectroscopy (ARPES) experiment mapping the surface band structure [Hsieh et al., 2008]. Observation of the topological nature of possible 3D TIs by transport experiments, as conducted for the experimental observation of the 2D QSH insulator, proved difficult due to competing bulk contributions to the conductivity. With ARPES, however, it was possible to image the material's band structure and reveal whether surface Dirac bands exist. In ARPES, energetic photons are used to emit electrons from a material. The analysis of energy and momentum of these photoemitted electrons reveals information about the band structure of the system. Since surface states have no dispersion in the direction perpendicular to the surface in contrast to bulk states, it is possible to separate surface and bulk contributions by studying energy and momentum of the emitted electrons.

Following the discovery of the first 3D TI, other materials were predicted to be 3D TIs [Zhang et al., 2009a; Yan et al., 2010], and experimentally observed by ARPES [Hsieh et al., 2009a; Chen et al., 2009; Xia et al., 2009; Zhang et al., 2009b; Wang et al., 2011] and scanning tunneling spectroscopy [Zhang et al., 2009b;

Alpichshev et al., 2010]. Among the most promising candidates were Bi-based compounds, such as Bi_2Se_3 and Bi_2Te_3, which were coined 'second generation' materials by Moore [2009]. The 3D TI Bi_2Se_3 has many advantages over the first discovered material Bi_xSb_{1-x}. Bi_2Se_3 is a compound as opposed to an alloy and might thus be prepared with less disorder and with a higher degree of purity. While Bi_xSb_{1-x} has a complicated surface state structure, Bi_2Se_3 only exhibits a single pair of topologically protected surface states. In addition Bi_2Se_3 has a large band gap of ~ 0.3 eV (3600 K) making the topological behavior accessible at larger temperature or even room temperature for high purity samples [Xia et al., 2009]. Indeed, topological behavior was observed in Bi_2Se_3 up to room temperature and surface states traversing the bulk gap of Bi_2Se_3 were revealed using ARPES [Hsieh et al., 2009a]. The theoretical idealization of these surface states would be a single Dirac cone, making this topological insulator closely related to the Dirac electronic structure of graphene [Moore, 2010].

The intense attention this new state of matter has received from condensed matter physicists is rooted in its unique properties which for the edge or surface states are 'unlike any other known one- (1D) or two-dimensional (2D) electronic system' [Hasan and Kane, 2010]. Conventional charge transport is limited by dissipation induced by backscattering of carriers at, e.g., impurities or defects. 2D TIs exhibit 1D edge states that are protected against elastic backscattering by time-reversal symmetry leading to a low dissipation state.[2] The strong spin-orbit coupling in 3D TIs leads to a unique surface state spin structure. The surface states are helical, i.e., spin and momentum are locked perpendicular to each other such that each surface-momentum possesses a unique spin direction.

These fascinating properties of TIs, such as helical gapless surface states, lead to a variety of possible applications. When brought into contact with superconductors, TIs might be used to realize topological superconducting phases hosting Majorana modes [Fu and Kane, 2008]. Such Majorana bound states could be used to engineer new types of quantum bits suggesting a possible application of TIs in quantum computers. The topological surface states also lead to exotic optical phenomena. It was, e.g., predicted that when time-reversal symmetry is broken, gapped surface states cause giant Kerr rotations of polarized light [Tse and Mac-Donald, 2010]. The magneto-optical Kerr effect describes the change of the polarization of light that is reflected from a magnetic surface. The angle by which the polarization plane is rotated is directly related to the magnetization of the material. For incident linearly polarized light it was predicted that multiple internal

---

2 Strictly speaking this is only true for weak interactions. Electron interactions can preserve time-reversal symmetry and lead to inelastic backscattering.

reflections between the top and bottom surfaces of a thin film TI can enhance the rotation of the polarization plane leading to a large Kerr angle $\theta_K \simeq \pi/2$ [Tse and MacDonald, 2010]. Their gapless helical surface states also make TIs promising materials for optoelectronic applications such as transparent conductors [Peng et al., 2012] and wide-band photodetectors [Zhang et al., 2010b]. In addition, it has been proposed [Raghu et al., 2010; Hosur, 2011; Ganichev and Prettl, 2003] and experimentally observed [McIver et al., 2012; Duan et al., 2014] that a TI illuminated with light can exhibit an electric charge current on the surface, a so-called photocurrent.

1.2 PHOTOCURRENTS

Because of the spin-helical nature of the surface states, a surface charge current flowing in a TI is necessarily spin polarized. Such spin-polarized currents are an essential ingredient for spintronics where not only the charge but also the spin degree of freedom plays a role in electronic applications. Photocurrent generation on the surface of a TI would allow for the injection and manipulation of such spin-polarized currents, making TIs promising materials for spintronic devices. Last year, it was experimentally observed that a charge current flowing in a thin film TI can manipulate the magnetization of an adjacent ferromagnet, paving the way for the application of TIs in computer memory and logic [Mellnik et al., 2014]. As we will see in more detail later, photocurrents in TIs might also be used to distinguish between bulk and surface contributions in transport experiments where signatures of the topological behavior are often masked by additional bulk effects. Understanding the photocurrent response of TIs, thus, lays the groundwork for a variety of further research on TIs and their applications. Currents restricted to the surface would pave the way to study the surface states and topological behavior in transport experiments. The ability to inject and control spin-polarized currents would advance 3D TIs as possible materials for opto-spintronic devices.

1.2.1 *Photocurrent generation*

Photocurrents can be induced in materials by a variety of processes. If light excites electrons such that the distribution of excited carriers is symmetric in momentum space, no net current will flow since the contributions from carriers
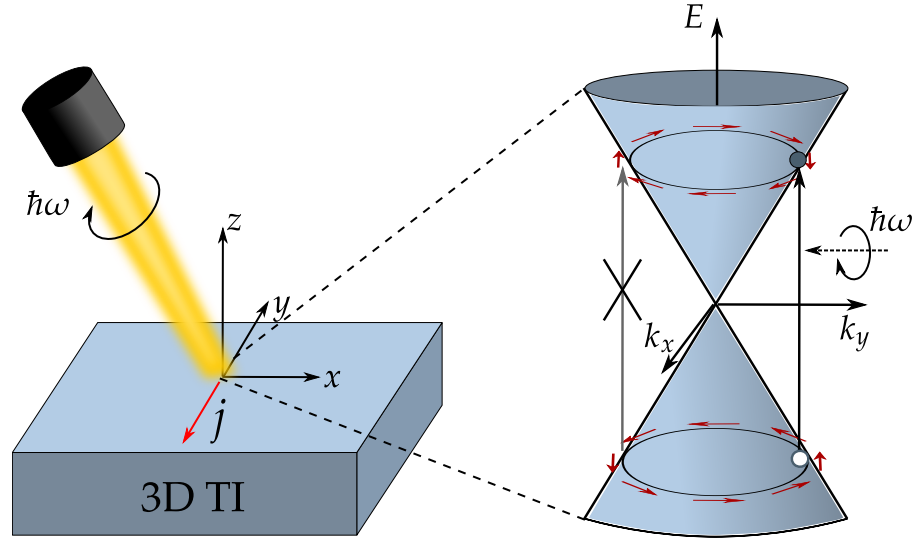
Figure 1.5: Schematic illustration of the photocurrent generation on TI surfaces. Left: Shining light onto a surface generates a photocurrent j. Right: Due to the helical spin structure of the surface states of TIs, circularly polarized light preferably interact with electrons at $+k$ but not at $-k$ exciting electrons asymmetric in momentum space. The resulting asymmetric carrier distribution leads to a net photocurrent.

at $\pm k$ cancel each other. A photocurrent can thus only be induced if the final distribution of excited carriers is asymmetric in momentum space. Without an external field which breaks the symmetry, this can happen, e.g., when scattering or relaxation processes of excited particles are asymmetric or when the transfer of photon momentum to the charge carriers leads to a shift or 'drag' of the excited carrier distribution. Even simpler one can imagine that the initial excitation of electrons by photon absorption occurs asymmetrically in momentum space leading to a net photocurrent. This last effect, i.e., the generation of a photocurrent by asymmetric excitations, will be the focus of Chaps. 4 and 5 of this thesis.

Microscopically, the possibility of such asymmetric excitations in 3D TIs can be easily motivated. In the widely used 3D TI Bi_2Se_3, the surface states, in an idealized model, can be described by a single Dirac cone [cf. Sec. 2.1]. The surface states are helical, i.e., electron spin and momentum are locked perpendicular to each other. Thus, electrons with the same energy but at opposite momenta have opposite spin. Light with energy less than the bulk band gap excites electrons within the Dirac cone. Circularly polarized light preferably couples to electrons with spins that are either aligned or anti-aligned to the wavevector q of the light

depending on the light's helicity [Meier and Zakharchenya, 1984] [cf. Sec. 2.2.3]. Thus, when shining circularly polarized light obliquely onto the surface of a TI, electrons with a spin component, say, parallel to q are preferably excited over electrons with a spin component anti-parallel to q. Since opposite spins correspond to opposite momenta, this leads to electrons being excited at, say, $+k$ but not at $-k$ as illustrated in Fig. 1.5. Changing the helicity of the light would then excite electrons at $-k$ but not at $+k$, reversing the direction of the induced current. Exciting surface electrons within the Dirac cone using circularly polarized light can thus lead to a carrier distribution which is asymmetric in momentum space and a net photocurrent. Based on the mechanism just explained, switching the polarization of the light between left- and right-circular polarization changes the sign of the induced photocurrent. In the bulk of a 3D TI a photocurrent response due to the described mechanism will vanish. The bulk states of TIs such as Bi_2Se_3 are spin-degenerate such that circularly polarized light would lead to equal excitations at both $+k$ and $-k$ with a no net current.

A photocurrent response has been observed experimentally on the surface of the 3D TI Bi_2Se_3 [McIver et al., 2012; Duan et al., 2014]. McIver et al. [2012] studied the dependence of the photocurrent on the light polarization and found a contribution which changes sign with the helicity of the light. Due to its importance for this thesis, this experiment will be reviewed in Chap. 3. While the authors report that the measured photocurrent has surface state origin, the microscopic mechanisms underlying the experimental observation are unclear. In Chaps. 4 and 5 we theoretically investigate the photocurrent generation on TI surfaces and shed light onto the microscopic processes involved in this effect.

Phenomenologically the photocurrent response to an electromagnetic wave can be described within the framework of the photogalvanic effect (PGE) [for a review see, e.g., Ganichev and Prettl [2003]]. In Sec. 2.2 we will see in detail based on symmetry arguments, that to leading order in the electric field amplitude the PGE vanishes in inversion symmetric systems. On TI surfaces, however, inversion symmetry is always broken and photocurrents can occur. Yet the crystal symmetry imposes constraints on their orientation and polarization dependence.

Indeed, 3D TIs such as Bi_2Se_3 obey bulk inversion symmetry and photocurrents are only allowed because inversion symmetry is broken by the surface.[3] This may actually prove to be a valuable tool for accessing surface properties even

_____

3 There exist other effects not considered in this thesis, such as the photon drag effect, that are allowed in inversion symmetric systems.

when the chemical potential is in the bulk valence or conduction band. Many 3D TIs (such as Bi_2Se_3) are naturally electron-doped which means that the chemical potential does not lie within the bulk band gap but inside the bulk conduction band. Observing topological behavior in transport experiments thus becomes difficult as surface effects are often masked by contributions from the metallic bulk. For instance, the widely used 3D TI Bi_2Se_3 is naturally n-type. When a cleaved surface is exposed to air, electron doping even increases due to surface charging effects that are caused by adsorbates from the environment or by migrating defects [Park et al., 2010; Hsieh et al., 2009b]. There have been experimental reports that the Fermi level in 3D TIs can be varied by additional doping or back gates [Checkelsky et al., 2009; Hsieh et al., 2009a; Chen et al., 2010] but preparing samples in a such a way that transport experiments single out the surface contributions proves difficult. A photocurrent signature with obvious surface origin might thus be a valuable tool.

Motivated by these ideas, this thesis provides a theoretical analysis of photocurrent generation in TIs. The mechanism described above [cf. Fig. 1.5] gives an intuitive picture of how photocurrents might be generated on TI surfaces and suggests that the microscopic origin of the experimentally measured photocurrent could be understood within a simple Dirac cone model. In Chap. 4 we therefore study the photocurrent generation within a pure surface state model. We calculate the photocurrent response due to asymmetric excitations within the Dirac cone and analyze the polarization dependence of the resulting current and its dependence on the angle of incidence of the light. Surprisingly we find, contrary to the earlier assumption, that a pure surface state model is not sufficient to explain the experimental observations even taking into account various corrections to the linear dispersion. Thus, understanding the effects of photocurrent generation in TIs requires a more advanced model.

In Chap. 5 we therefore extend our model to include the low energy bulk states [cf. Fig. 1.6]. While deep in the bulk the dominant photocurrent response should vanish due to inversion symmetry, this is not the case near the surface where light can induce transitions between surface and bulk states. Indeed, the experimental measurements of photocurrents where conducted with photon energies that exceed the bulk band gap [McIver et al., 2012; Duan et al., 2014]. We thus study the photocurrent response at the surface of a TI within a four-band model for the surface and bulk states [Liu et al., 2010] [cf. Sec. 2.1]. We analyze the dependence of the photocurrent on the angle of incidence of the light and on the light polarization and study the microscopic processes responsible for the photocurrent generation. We consider transitions between the surface Dirac cone
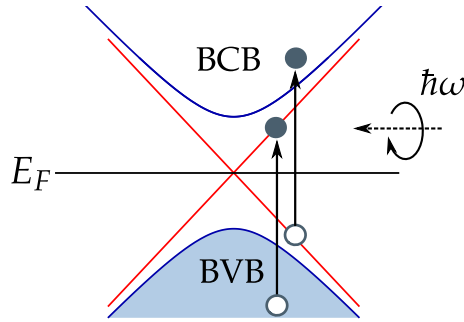
Figure 1.6: Photoinduced transitions between the spin-helical surface states (red) and the bulk states might lead to a net photocurrent. We will consider transitions from the bulk valence band (BVB) to the surface Dirac cone and from the Dirac cone into the bulk conduction band (BCB).

and the bulk valence band or the bulk conduction band as illustrated in Fig. 1.6 and study the dependence of the resulting photocurrent on the Fermi energy.

1.2.2 *Photocurrent relaxation*

For a comprehensive study of photocurrents in TIs, it is not sufficient to restrict the analysis to the generation of photocurrents. The magnitude of a photoresponse is, of course, governed by both the excitation process and the subsequent relaxation of the current. For a full understanding of surface photocurrents in TIs one therefore needs to study current relaxation in Dirac systems.

As described above, the photocurrent is carried by excited electron-hole pairs. Thus, scattering events that change the momentum of electron or hole can in principle affect the current. For quadratic dispersions, momentum conserving scattering events such as electron-electron scattering will not change the current. Indeed, momentum is proportional to velocity and thus current. Momentum conservation thus implies current conservation in quadratically dispersing systems. This argument does not hold for the linearly dispersing surface states of TIs. Here, momentum is no longer proportional to velocity and even momentum conserving scattering events can relax the current.

In Chap. 6 we will therefore present a detailed analysis of photocurrent relaxation in the surface states of TIs. We will focus on a perfectly linear dispersion such that our results are also applicable to other Dirac systems, e.g.,

graphene. In linearly dispersing systems, current relaxation can occur through, e.g., electron-electron (e-e), electron-phonon, or impurity scattering. Considering a sufficiently clean sample one might neglect impurity or disorder scattering. Also for sufficiently low temperatures one expects that e-e interaction dominates over electron-phonon scattering. At low temperatures, e-e scattering can be more effective than electron-phonon interactions in relaxing excited carriers in graphene if the particles are excited with low pump fluences below the optical phonon frequencies [Winzer et al., 2010; Kim et al., 2011; Song et al., 2011; Winzer and Malic, 2012; Song et al., 2013; Tani et al., 2012]. In Chap. 6 we will therefore study how e-e scattering affects the photocurrent in Dirac systems.

Energy relaxation of excited particles in linearly dispersing systems has already been studied in detail both theoretically [Cheianov and Fal'ko, 2006; Butscher et al., 2007; Stauber et al., 2007; Tse and Das Sarma, 2009; Winzer et al., 2010; Kim et al., 2011; Winzer and Malic, 2012; Song et al., 2013; Tomadin et al., 2013] and experimentally [Hsieh et al., 2011; Kumar et al., 2011; Breusing et al., 2011; Sobota et al., 2012; Hajlaoui et al., 2012; Tani et al., 2012; Gierz et al., 2013; Brida et al., 2013] and some interesting effects were discovered. It was predicted that e-e scattering can lead to carrier multiplication [Winzer et al., 2010; Winzer and Malic, 2012; Song et al., 2013]. When a highly excited electron interacts with the Fermi sea, it relaxes in small energy steps and in each step excites an electron from the Fermi sea to above the Fermi energy [Song et al., 2013] [cf. Fig. 1.7]. Depending on the pump fluence used to initially excite the particles, this 'relaxation cascade' [Song et al., 2013] can lead to a large number of excited electrons. For large pump fluences, competing scattering processes that do not lead to carrier multiplication such as electron-phonon scattering or electron-hole recombination become more effective [Winzer and Malic, 2012; Song et al., 2013]. Experimental observations of carrier multiplication were consequently reported for low pump fluences [Tani et al., 2012; Tielrooij et al., 2013; Plötzing et al., 2014].

While energy relaxation in Dirac system has been explored in detail, the question remains how current is affected by e-e scattering. Sun et al. [2012] analyzed the effect of a hot carrier background on photocurrents in graphene. The hot background was found to effectively reduce the photocurrent with a relaxation rate that is determined by the density of the thermal carrier background. In Chap. 6 we analyze current relaxation in a very different regime. Considering that e-e scattering may dominate for low pump fluences, we will study the limit of a single excited electron-hole pair that undergoes carrier-carrier scattering events as illustrated in Fig. 1.7. We will look at the relaxation dynamics of electron and hole independently and find surprising results. Scattering of electron and hole
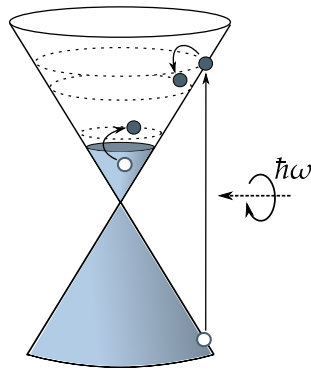
Figure 1.7: After photoexcitation creates an electron-hole pair, carrier-carrier scattering will relax the particles and affect the photocurrent. The excited electron, e.g., relaxes by exciting an electron from the Fermi sea to above the Fermi energy. Similar processes also exist for the hole.

can have a very different effect on the current and this effect strongly depends on the position of the Fermi level, specifically, whether it is above or below the Dirac point. We consider the effect of a single scattering event on the current and also study the limit of many scattering events when the excited carriers have completely relaxed.

THEORETICAL BACKGROUND

In this chapter we discuss some theoretical background that will be needed in the following chapters. A widely used 3D TI is Bi_2Se_3 due to its large band gap and simple surface structure, and we introduce a model Hamiltonian for this system in Sec. 2.1. We also give an overview of photogalvanic effects from the point of view of symmetry in Sec. 2.2 which provides a backdrop to the discussion in Chaps. 4 and 5.

2.1 MODEL 3D TOPOLOGICAL INSULATOR BI2SE3

In this section we discuss a model Hamiltonian for the 3D TI Bi_2Se_3. As discussed in the previous chapter, this 'second generation' [Moore, 2009] TI is well suited as a model system, due to its large band gap which makes topological behavior accessible at room temperature, and due to its relatively simple surface band structure involving a single Dirac cone in the idealized picture. We start our description of the material with the crystal structure and corresponding symmetry properties of Bi_2Se_3 crystals before studying the atomic orbitals. The presentation is based on Zhang et al. [2009a] and Liu et al. [2010].

2.1.1 *Crystal structure and symmetries*

Materials belonging to the Bi_2Se_3 family, including Bi_2Te_3, Sb_2Se_3, and Sb_2Te_3 have a rhombohedral crystal structure with space group D_{3d}^5 ($R\bar{3}m$). The crystal consists of layers stacked along the z-direction where each layer consists of either
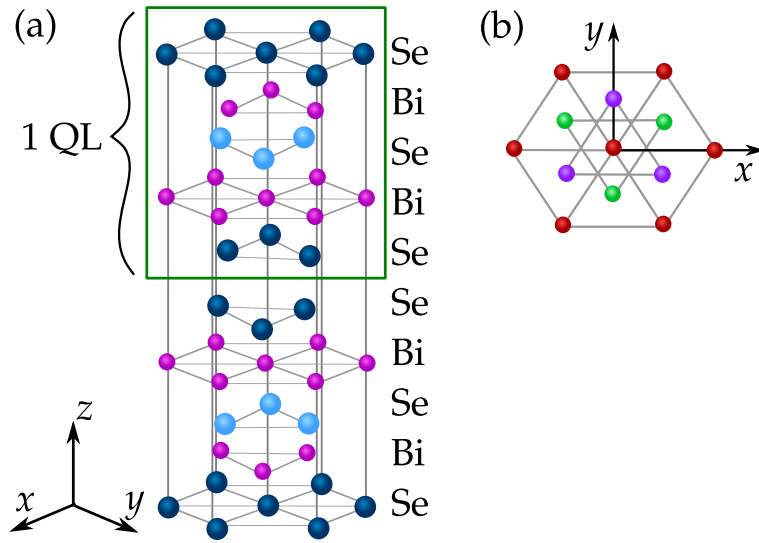
Figure 2.1: Lattice structure of Bi_2Se_3. a) Along the z-direction the lattice consists of al-
ternating layer of Bi and Se atoms. Five consecutive layers, termed quintuple
layer (QL), make up the building block of the lattice. b) Viewed from the top,
the 2D layers can be arranged in three different orientations leading to the
three-fold rotational symmetry and the mirror axis as explained in the text.

Bi and Se atoms as illustrated in Fig. 2.1 (a). The unit cell of Bi_2Se_3 contains five
atoms, two Bi atoms and three Se atoms, such that five consecutive atomic layers
taken together are the building block of the crystal. Within such a quintuple
layer (QL), Bi and Se layers alternate and coupling is strong due to chemical
bonds between Bi and Se, whereas the coupling between quintuple layers is
mediated only by weak van der Waals forces. Viewed from above, the crystal
structure can be seen as stacked triangular lattices which can have three possible
orientations as illustrated in Fig. 2.1 (b). The coordinate system is chosen such
that the z-direction is perpendicular to the atomic layers and the origin is taken
to be the Se site at the center of a QL. Choosing the binary axis with twofold
rotational symmetry to be the x-axis, the crystal has the following symmetries as
seen in Fig. 2.1: There is threefold rotational symmetry around the z-direction,
twofold rotational symmetry around the x-direction, and inversion symmetry
about the origin. In addition to the Se site at the origin, a single unit cell consists
of two equivalent Bi atoms (Bi and Bi') and two equivalent Se atoms (Se1 and
Se1'), related by inversion symmetry. When talking about surface states in the
following chapters we will always be considering the (111) surface of Bi_2Se_3
which describes a surface in the xy-plane as illustrated in Fig. 2.1 (b). Naturally,
inversion symmetry is broken at the surface and the crystal symmetry reduce

from D_{3d}^5 to C_{3v}. The surface thus exhibits three-fold rotational symmetry around the z-axis and a mirror symmetry about the y-axis.

In order to verify that a material is a 3D TI, one needs to know the states at all eight time-reversal invariant momenta [Fu et al., 2007]. *Ab initio* calculations [Zhang et al., 2009a] proved that Bi$_2$Se$_3$ is indeed a 3D TI and that its topological nature is rooted in a band inversion at the Γ point only. To understand the origin of the topological surface states of Bi$_2$Se$_3$ we can thus focus on the low energy physics near the Γ point.

The electronic configuration is $6s^2 6p^3$ for Bi and $4s^2 4p^4$ for Se. We are interested in a low-energy model for Bi$_2$Se$_3$ and it is thus sufficient to include only the outermost p orbitals. Combining the orbitals of the equivalent Bi and Se atoms, respectively, one can form bonding and anti-bonding states with definite parity. Taking into account all effects such as hybridization of orbitals and level shifts due to the crystal symmetry and resulting crystal field splittings but neglecting spin-orbit coupling (SOC), the energy of the Bi orbitals is higher than the Se orbitals [Liu et al., 2010]. As this neglects spin, the band structure is still topologically trivial. The atomic SOC Hamiltonian is given by

$$H_{\text{SOC}} = \alpha \boldsymbol{l} \cdot \boldsymbol{s}, \tag{2.1}$$

where

$$\alpha = \frac{\hbar}{4m_0^2 c^2} \frac{1}{r} \frac{\partial V}{\partial r} \tag{2.2}$$

is the spin-orbit coupling strength which depends on the crystal potential $V(\boldsymbol{r})$, and $\boldsymbol{l}$ and $\boldsymbol{s}$ describe orbital and spin angular momentum, respectively. Including SOC shifts the low-energy states and results in a level crossing of the low-energy Bi and Se states as illustrated in Fig. 2.2. Since the Bi and Se states have opposite parity, this crossing marks a band inversion and a topological phase transition from a normal insulator to a topological insulator [Zhang et al., 2009a]. This topological phase transition due to band inversion is thus analogous to the topological phase transition in HgTe quantum wells [Bernevig et al., 2006; König et al., 2007]. While in the quantum wells the phase transition was tuned by changing the well thickness, in Bi$_2$Se$_3$ the strong spin-orbit coupling drives the system into a topological-insulator phase. The band inversion in Bi$_2$Se$_3$ leads to the formation of gapless surface states near the Γ point. These surface states are topologically protected as long as time-reversal symmetry is not broken and consequently, smooth deformations of the band structure that do not close the band gap will not effect the surface states.
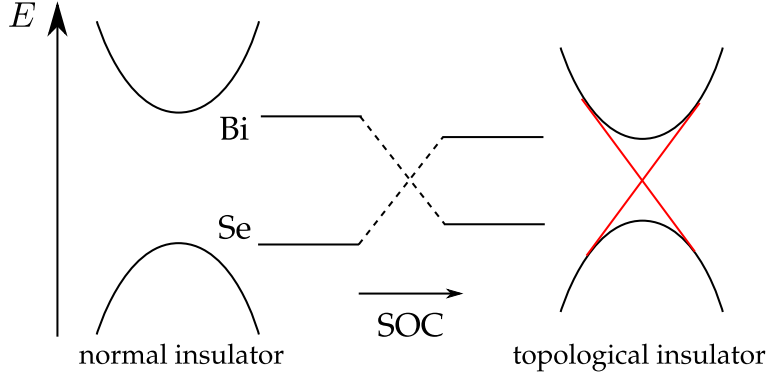
Figure 2.2: Schematic illustration of the origin of the topological nature of Bi$_2$Se$_3$. Without including spin-orbit coupling (SOC) Bi$_2$Se$_3$ would be a normal insulator. Including SOC the bandstructure near the Γ point exhibits a level crossing between states of opposite parity leading to the formation of a topological insulator with gapless surface states indicated in red.

Since the topological nature of Bi$_2$Se$_3$ is solely determined by the states near the Γ point the essential physics can be captured in an effective low energy model. The four lowest energy states are

$$|\text{Bi}^+, \pm\frac{1}{2}\rangle = a_\pm^B |\text{Bi}^+, p_z, \uparrow\downarrow\rangle + b_\pm^B |\text{Bi}^+, p_\pm, \downarrow\uparrow\rangle \tag{2.3}$$

$$|\text{Se}^-, \pm\frac{1}{2}\rangle = a_\pm^S |\text{Se}^-, p_z, \uparrow\downarrow\rangle + b_\pm^S |\text{Se}^-, p_\pm, \downarrow\uparrow\rangle, \tag{2.4}$$

where $|X, p_\pm, \sigma\rangle = \mp\frac{1}{2}\left(|X, p_x, \sigma\rangle \pm i|X, p_y, \sigma\rangle\right)$ and the superscript denotes parity. $a_\pm^{S,B}, b_\pm^{S,B}$ are hybridizations between states with equal total angular momentum and describe the distribution of weight on the different orbitals. Starting from these four states, Zhang et al. [2009a] constructed a Hamiltonian from the theory of invariants taking into account the crystal symmetries. In the basis $|\text{Bi}^+, \frac{1}{2}\rangle, |\text{Se}^-, \frac{1}{2}\rangle, |\text{Bi}^+, -\frac{1}{2}\rangle, |\text{Se}^-, -\frac{1}{2}\rangle$ the symmetry operations can be represented as follows: Time reversal becomes $\mathcal{T} = i\sigma_y K$, where σ denotes the spin Pauli matrices in spin space and K is complex conjugation. The threefold rotational symmetry about the z-axis becomes $\mathcal{R}_3 = e^{i(\Pi/2)\theta}$ with $\Pi = \sigma_z \otimes \mathbf{1}$ and $\theta = 2\pi/3$. Twofold rotation around the x-axis becomes $\mathcal{R}_2 = i\sigma_x \otimes \tau_z$ and inversion becomes $\mathcal{P} = \mathbf{1} \otimes \tau_z$, where τ acts in the basis of the Bi and Se sublattices. Note that 'spin' actually refers to total angular momentum $J = L + S$ since the $\pm 1/2$ in the basis $\{|\text{Bi}^+, \pm\frac{1}{2}\rangle, |\text{Se}^-, \pm\frac{1}{2}\rangle\}$ represent total angular momentum. It turns out, however, that the low energy states have orbital weight mostly on the p_z orbitals ($\sim 50 - 70\%$ [Zhang et al., 2013; Zhu et al., 2013]) with smaller contributions from the p_x and p_y orbitals ($\sim 30\%$ [Zhang et al., 2013; Zhu et al., 2013]). Thus we will continue to talk about 'spin' instead of total angular momentum.

Finally, up to cubic order in k the effective 4×4 Hamiltonian can be written as [Liu et al., 2010]

$$
\begin{aligned}
H_{eff} =& \epsilon_k \mathbf{1} \otimes \mathbf{1} + \mathcal{M}(\mathbf{k}) \mathbf{1} \otimes \tau_z + \mathcal{B}(k_z) k_z \mathbf{1} \otimes \tau_y + \mathcal{A}(k_\parallel)(\sigma_x k_y - \sigma_y k_x) \otimes \tau_x \\
& + \frac{R_1}{2}(k_+^3 + k_-^3)\sigma_z \otimes \tau_x + \frac{R_2}{2i}(k_+^3 - k_-^3)\mathbf{1} \otimes \tau_y,
\end{aligned}
\tag{2.5}
$$

where

$$
\epsilon_k = C_0 + C_1 k_z^2 + C_2 k_\parallel^2,
\tag{2.6}
$$

$$
\mathcal{M}(\mathbf{k}) = M_0 + M_1 k_z^2 + M_2 k_\parallel^2,
\tag{2.7}
$$

$$
\mathcal{B}(k_z) = B_0 + B_2 k_z^2,
\tag{2.8}
$$

$$
\mathcal{A}(k_\parallel) = A_0 + A_2 k_\parallel^2,
\tag{2.9}
$$

and $k_\parallel^2 = k_x^2 + k_y^2$ and $k_\pm = k_x \pm i k_y$. Numerical values for these parameters were obtained by Zhang et al. [2009a] using $\mathbf{k} \cdot \mathbf{p}$ theory. The basic idea behind this approximation method is to assume that the wavefunction is known at some special point in the Brillouin zone, here the Γ point at $\mathbf{k} = 0$, and to treat terms in the Hamiltonian that are proportional to $\mathbf{k} \cdot \mathbf{p}$ as a perturbation. Since the wavefunction at the Γ point can be obtained by *ab initio* calculations, this approximation provides a method of finding numerical values for the parameters in H_{eff}. Fig. 2.3 shows the bulk and surface states resulting from the Hamiltonian (2.5). One can easily deduce that the bulk states in the four-band model described by Eq. (2.5) are spin degenerate. There are two bands with opposite spin orientations at both positive and negative energy $\pm E$. The surface states, however, are not degenerate but exhibit a unique spin structure for positive and negative energy as we will see in the following section.

2.1.2 *Surface states in the four-band model*

In this section we show that solving the effective Hamiltonian (2.5) with appropriate boundary conditions gives indeed surface state solutions. For clarity of calculation, we only include terms in Eq. (2.5) that are essential for the existence of topological surface states. We thus study the simplified Hamiltonian

$$
H_0 = (M_0 + k_z^2 M_1) \mathbf{1} \otimes \tau_z + B_0 k_z \mathbf{1} \otimes \tau_y + A_0(\sigma_x k_y - \sigma_y k_x) \otimes \tau_x.
\tag{2.10}
$$
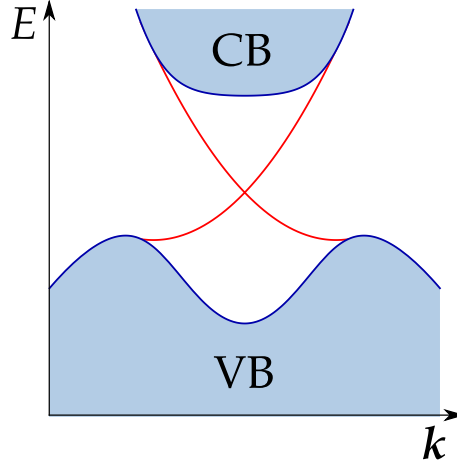
Figure 2.3: Band structure of Bi$_2$Se$_3$ obtained from Eq. (2.5). The shaded areas represent the bulk conduction band (CB) and valence band (VB). The bulk exhibits a band gap that is traversed by gapless surface states indicated in red.

We consider the semi-infinite half space $z > 0$ which corresponds to the (111) surface of Bi$_2$Se$_3$. Replacing k_z by $-i\partial_z$ we obtain the eigenvalue equation

$$H_0(k_z \to -i\partial_z)\Psi(z) = E\Psi(z), \tag{2.11}$$

whose solution describes the surface states and their energy dispersion. Looking at Hamiltonian (2.10) we see that there is only one term that is not a unit matrix in spin space, namely $A_0(\sigma_x k_y - \sigma_y k_x)$. The corresponding eigenvectors are easily determined,

$$A_0(\sigma_x k_y - \sigma_y k_x)\begin{pmatrix} \pm ie^{-i\phi} \\ 1 \end{pmatrix} = \pm A_0 k_\parallel \begin{pmatrix} \pm ie^{-i\phi} \\ 1 \end{pmatrix}, \tag{2.12}$$

where $\tan\phi = k_y/k_x$. The wavefunctions will thus have the form

$$\Psi_\uparrow(z) = \frac{1}{\sqrt{2}}\begin{pmatrix} ie^{-i\phi} \\ 1 \end{pmatrix} \otimes \chi(A_0, z) \tag{2.13}$$

$$\Psi_\downarrow(z) = \frac{1}{\sqrt{2}}\begin{pmatrix} -ie^{-i\phi} \\ 1 \end{pmatrix} \otimes \chi(-A_0, z), \tag{2.14}$$

with $\chi(\pm A_0, z)$ obeying

$$h_\pm(k_z \to -i\partial_z)\chi(\pm A_0, z) = E_\pm\chi(\pm A_0, z). \tag{2.15}$$

Here $h_\pm$ is a reduced 2×2 Hamiltonian given by

$$h_\pm = (M_0 + k_z^2 M_1)\tau_z + B_0 k_z \tau_y \pm A_0 k_\parallel \tau_x. \tag{2.16}$$

Inserting the trial wavefunction $\chi_\lambda e^{\lambda z}$ into the Schrödinger equation (2.15) yields four possible solutions for λ [Shan et al., 2010],

$$\lambda_\pm^2 = \frac{2M_0M_1 + B_0^2}{2M_1^2} \pm \sqrt{\frac{4B_0^2M_0M_1 + B_0^4}{4M_1^4} + \frac{E^2 - A_0^2k^2}{M_1^2}} \qquad (2.17)$$

with corresponding eigenvectors

$$\chi_\lambda(A_0) = \begin{pmatrix} \frac{A_0k - B_0\lambda}{E - M_0 + \lambda^2 M_1} \\ 1 \end{pmatrix}. \qquad (2.18)$$

A general wavefunction $\chi(z)$ is then a superposition of the four solutions $\chi_{\pm\lambda_\pm}$,

$$\chi(A_0, z) = \sum_{\alpha,\beta=\pm} \gamma_{\alpha,\beta}\chi(\alpha\lambda_\beta)e^{\alpha\lambda_\beta z}, \qquad (2.19)$$

where the coefficients $\gamma_{\alpha,\beta}$ are determined by boundary conditions.

Up until now the considerations were general and apply to surface states as well as bulk states near the surface. We now want to solve for the surface states using the open boundary conditions

$$\Psi(z = 0) = 0. \qquad (2.20)$$

If surface states exist they should, of course, be localized near the surface, i.e., the wavefunction should also obey

$$\Psi(z \to \infty) \to 0. \qquad (2.21)$$

With this condition the only non-zero coefficients in the superposition (2.19), will belong to λ with negative real part. Thus there will only be surface state solutions if at least two solutions for λ have a negative real part, otherwise we cannot fulfill the boundary conditions. Eq. (2.19) then gives a system of two equations with two unknowns which we can solve, leading to the energy solutions [Shan et al., 2010; Liu et al., 2010]

$$E = \pm A_0 k \qquad (2.22)$$

for $\chi(\pm A_0)$ respectively. The positive and negative energy surface states can now be simplified [Shan et al., 2010],

$$\Psi_\uparrow(z) = \frac{1}{\sqrt{N}} \begin{pmatrix} ie^{-i\phi} \\ 1 \end{pmatrix} \otimes \begin{pmatrix} 1 \\ 1 \end{pmatrix} \left(e^{-\lambda_+ z} - e^{-\lambda_- z} \right), \qquad (2.23)$$

$$\Psi_\downarrow(z) = \frac{1}{\sqrt{N}} \begin{pmatrix} -ie^{-i\phi} \\ 1 \end{pmatrix} \otimes \begin{pmatrix} 1 \\ 1 \end{pmatrix} \left(e^{-\lambda_+ z} - e^{-\lambda_- z} \right) \qquad (2.24)$$
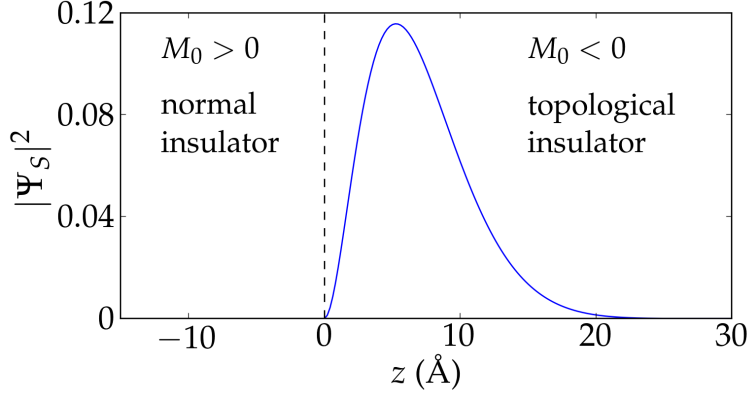
Figure 2.4: Surface state probability distribution as a function of z obtained from Eqs. (2.23)-(2.25). For $M_1 > 0$, $M_0 > 0$ leads to a normal insulator and $M_0 < 0$ to a TI. The surface state is clearly localized near the surface at $z = 0$ and falls off exponentially into the bulk of the TI. The results are the same for the positive and negative energy state. One can see that the surface state penetrates ~ 2 nm into the TI.

where $\Psi_\uparrow$ denotes the positive energy state and $\Psi_\downarrow$ the negative energy state, and [Liu et al., 2010]

$$\lambda_\pm = \frac{B_0}{2M_1} \pm \sqrt{\frac{B_0^2 + 4M_0M_1}{4M_1^2}}. \tag{2.25}$$

N is a normalization constant. The surface states have a unique spin structure which rotates around the Dirac cone, such that electrons at opposite momenta have opposite spin. For positive and negative energy the spin structure is inverted.

From Eq. (2.25) we see that topological surface states only exist if $M_0M_1 < 0$. For $M_0M_1 > 0$ we cannot fulfill the boundary conditions given by Eq. (2.20) and (2.21) and consequently no surface states exist. For Bi_2Se_3 the parameters obey $M_0 = -0.28$ eV< 0 and $M_1 = 6.86$ eV$\mathring{A}^2 > 0$ [Liu et al., 2010] such that Bi_2Se_3 indeed exhibits topological surface states at the domain wall with a trivial insulator.[1] For $M_1 > 0$, $M_0 < 0$ thus describes the necessary band inversion condition for Bi_2Se_3 to be a TI. Calculating the probability distribution illustrated in Fig. 2.4 shows that the surface states penetrate ~ 2 nm into the solid which corresponds to roughly two quintuple layers with $\sim 75\%$ contribution from the first QL and $\sim 25\%$ from the second QL from DFT analysis [Zhu et al., 2013].

---

[1] While obtaining the solution Eqs. (2.23)-(2.25) we already used that for Bi_2Se_3 $B_0/M_1 > 0$. For the opposite case one would, of course, have to change the signs in the exponents of the exponential functions.

2.1.3 *Effective 2D surface-state model*

We have shown that Bi₂Se₃ exhibits topological surface states and would like to obtain an effective surface Hamiltonian for them. The solution given by Eqs. (2.23) - (2.25) depends on the boundary conditions and parameters. The general form of the surface state wavefunction is, however, general, and we can always write the surface states as $\Phi_\uparrow = |\uparrow\rangle \otimes |\chi\rangle$ and $\Phi_\downarrow = |\downarrow\rangle \otimes |\chi\rangle$, where χ contains the information about material details, such as the boundary conditions. Projecting the Hamiltonian given by Eq. (2.5) onto the subspace defined by the basis $[\Phi_\uparrow, \Phi_\downarrow]$, one arrives at the effective surface Hamiltonian [Zhang et al., 2009a; Fu, 2009; Liu et al., 2010]

$$H_S = \tilde{C}_0 + \tilde{C}_2 k_\parallel^2 + v_F(\sigma_x k_y - \sigma_y k_x) + \frac{\lambda}{2}(k_+^3 + k_-^3)\sigma_z. \qquad (2.26)$$

The first two terms account for particle-hole asymmetry and the third gives the linear Dirac spectrum. The last term is a cubic warping term and describes deviations from linearity. As before, $k_\parallel^2 = k_x^2 + k_y^2$ and $k_\pm = k_x \pm i k_y$. This Hamiltonian is time-reversal symmetric, i.e., $\mathcal{T}^{-1} H_S(\boldsymbol{k}_\parallel)\mathcal{T} = H_S(-\boldsymbol{k}_\parallel)$. The states at $\pm \boldsymbol{k}_\parallel$ are Kramers partners, i.e., connected by time-reversal symmetry. Therefore, as long as time-reversal symmetry is preserved, backscattering between states with opposite momenta is forbidden. The energy dispersion of the surface electrons is given by

$$E_\pm = \tilde{C}_0 + \tilde{C}_2 k_\parallel^2 \pm \sqrt{v_F^2 k_\parallel^2 + \lambda^2 k_\parallel^6 \cos^2(3\phi)} \qquad (2.27)$$

and the surface states can be written as

$$\Psi_\pm = \frac{1}{\sqrt{N_\pm}} \begin{pmatrix} i v_F k_\parallel e^{-i\phi} \\ \pm E - \lambda k_\parallel^3 \cos(3\phi) \end{pmatrix} \qquad (2.28)$$

where $E = E_+$ and $N_\pm = v_F^2 k_\parallel^2 + \left(\pm E - \lambda k_\parallel^3 \cos(3\phi)\right)^2$ the normalization constant. For the particle-hole symmetric case without warping, i.e., for $\tilde{C}_0 = \tilde{C}_2 = \lambda = 0$, this reduces to a perfectly linear dispersion and the spin structure of the previous result given by Eqs. (2.23) and (2.24).
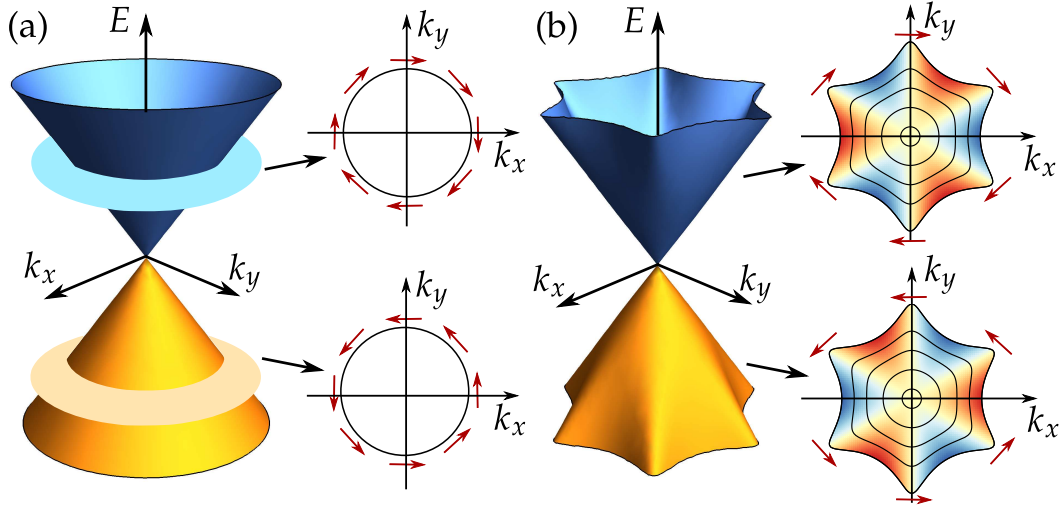
Figure 2.5: Dirac cone and spin structure of the surface states. (a) $\lambda = 0$, i.e., perfectly linear dispersion: Red arrows indicate the spin orientation which is purely in-plane and locked perpendicular to momentum. (b) $\lambda > 0$, i.e., including hexagonal warping: The constant energy contours acquire a hexagonal shape with stronger warping for larger energies. The red and blue shading illustrates the spin z-component which is tilted in and out of the plane due to warping.

Let us now look at the surface states more closely when including warping. The spin polarization in k-space is easily obtained,

$$\langle \Psi_+ | \sigma_x | \Psi_+ \rangle = \frac{2 v_F k_\| \sin \phi}{N_+} \left(E - \lambda k_\|^3 \cos(3\phi) \right) \tag{2.29}$$

$$\langle \Psi_+ | \sigma_y | \Psi_+ \rangle = -\frac{2 v_F k_\| \cos \phi}{N_+} \left(E - \lambda k_\|^3 \cos(3\phi) \right) \tag{2.30}$$

$$\langle \Psi_+ | \sigma_z | \Psi_+ \rangle = \frac{2 \lambda k_\|^3 \cos(3\phi)}{N_+} \left(E - \lambda k_\|^3 \cos(3\phi) \right). \tag{2.31}$$

In the absence of warping, $\lambda = 0$, the spin structure is purely in-plane and spin and momentum are locked perpendicular to each other. This case is illustrated in Fig. 2.5 (a) neglecting particle-hole asymmetry. We see how the spin rotates around the Dirac cone. Finite λ induces hexagonal warping in the constant energy contours which becomes more pronounced with increasing energy. For finite warping the spins acquire a component along the z-direction perpendicular to the surface. While rotating around the constant energy contour, the spins now tilt alternatingly in and out of plane as illustrated by the red and blue shading in Fig. 2.5 (b).

With this knowledge about the surface and bulk states of Bi_2Se_3, we can continue to study the photocurrent response of TIs. In the following section, we will discuss the photocurrent generation based on the photogalvanic effect and see how the photocurrent response is restricted by the crystal symmetries of Bi_2Se_3.

2.2 PHOTOGALVANIC EFFECTS

A finite photocurrent on the surface of a TI requires an excited carrier distribution which is asymmetric in momentum space. Phenomenologically this results from the low spatial symmetry of the crystal surface and can be explained within the framework of the photogalvanic effects that describe the direct current response of a homogeneous medium under uniform illumination.

Phenomena belonging to the class of photogalvanic effects (PGE) were first predicted and observed more than 40 years ago [for a review see, e.g., Belinicher and Sturman [1980]; Sturman and Fridkin [1992]; Ivchenko and Pikus [1997]]. One usually distinguishes between the circular PGE (CPGE), where the induced photocurrent changes sign when the helicity of the light is switched between left- and right-circular polarization, and the linear PGE (LPGE) that is independent of the light's helicity. The generation of a direct current by the CPGE or LPGE is based on asymmetric excitation or relaxation processes in the system and can only occur in media with sufficiently low spatial symmetry. Due to the intrinsic asymmetry, however, a photocurrent can be generated without the application of additional external fields. Another effect belonging to this class is the so-called photon drag effect, where the current is driven by transfer of momentum from the photons to the electrons.

The PGEs have been studied extensively in semiconductors and semiconductor quantum wells (QWs). Especially the CPGE has proved to be a powerful tool for studying non-equilibrium processes in semiconductor QWs revealing information about the relaxation dynamics of excited electrons, the spin splitting of the band structure, or the symmetry of the crystal [for a review see, e.g., Ganichev and Prettl [2003]; Ivchenko and Ganichev [2008]]. Photocurrents can be generated in QW structures where spin degeneracy is broken due to k-linear terms in the Hamiltonian, e.g., due to bulk inversion asymmetry or structural inversion asymmetry. In 3D TIs we expect that effects such as the CPGE or LPGE can induce photocurrents at the surface where the bulk inversion symmetry is broken.

The leading order dc electric current response to an oscillating electric field is of second order in the electric field amplitude and can be written as

$$j_\lambda = \sigma_{\lambda\mu\nu} E_\mu(\omega) E_\nu^*(\omega), \tag{2.32}$$

where we imply Einstein's summation convention. $\sigma_{\lambda\mu\nu}$ is the (third-rank) photocurrent conductivity tensor and $E_\beta(\omega) = E_\beta^*(-\omega)$ is the complex electric field amplitude, with the real oscillating electric field given by $\mathcal{E}(t) = \boldsymbol{E}(\omega)e^{i\omega t} + \boldsymbol{E}^*(\omega)e^{-i\omega t}$. Under spatial inversion, the product of the electric-field components remains invariant, i.e., $E_\mu(\omega)E_\nu^*(\omega) \to E_\mu(\omega)E_\nu^*(\omega)$, while the current changes sign, i.e., $j_\lambda \to -j_\lambda$. Any tensor describing a physical property of a system should be invariant with respect to its symmetry operations. Thus for an inversion symmetric system, $\sigma_{\lambda\mu\nu}$ should be invariant under spatial inversion. For odd-rank tensors, however, inversion symmetry leads to $\sigma_{\lambda\mu\nu} \to -\sigma_{\lambda\mu\nu}$. Thus $\sigma_{\lambda\mu\nu}$ has to vanish for inversion symmetric systems. Since the bulk of the 3D TI Bi_2Se_3 is inversion symmetric, a photocurrent response described by Eq. (2.32) can only be induced at the surface of the TI. The current j_λ, of course, has to be real so that $\sigma_{\lambda\mu\nu} = \sigma_{\lambda\nu\mu}^*$. This tells us that the real part of $\sigma_{\lambda\mu\nu}$ is symmetric and the imaginary part is antisymmetric in the last two indices. Making use of this property, we can write the photocurrent response (2.32) as

$$j_\lambda = \frac{i}{2} Im[\sigma_{\lambda\mu\nu}](E_\mu E_\nu^* - E_\nu E_\mu^*) + \frac{1}{2} Re[\sigma_{\lambda\mu\nu}](E_\mu E_\nu^* + E_\mu^* E_\nu). \tag{2.33}$$

The first term can be written as a cross product such that we get [Ganichev and Prettl, 2003]

$$j_\lambda = \gamma_{\lambda\mu} i(\boldsymbol{E} \times \boldsymbol{E}^*)_\mu + \chi_{\lambda\mu\nu}(E_\mu E_\nu^* + E_\mu^* E_\nu). \tag{2.34}$$

γ is related to the imaginary part of the tensor $\sigma_{\lambda\mu\nu}$ and $\chi_{\lambda\mu\nu} = \frac{1}{2} Re[\sigma_{\lambda\mu\nu}]$ is symmetric in the last two indices, $\chi_{\lambda\mu\nu} = \chi_{\lambda\nu\mu}$. In addition to these two contributions, the second order current response also includes a photon-drag current proportional to the photon momentum $\boldsymbol{q}$. The tensor $\sigma_{\lambda\mu\nu} = \sigma_{\lambda\mu\nu}(\boldsymbol{q})$ could depend on $\boldsymbol{q}$, $\sigma_{\lambda\mu\nu}(\boldsymbol{q}) = \sigma_{\lambda\mu\nu}(0) + T_{\lambda\delta\mu\nu}q_\delta$, where T is a fourth-rank tensor. This includes the photon-drag contribution $j_\lambda(\boldsymbol{q}) = T_{\lambda\delta\mu\nu}q_\delta E_\mu E_\nu^*$. Since T is a fourth-rank tensor, this contribution to the photocurrent is allowed in inversion symmetric systems such as bulk Bi_2Se_3. Microscopically, the photon drag effect originates from the photoexcitation from an initial state $\Psi_i(\boldsymbol{k}_0)$ to a final state $\Psi_f(\boldsymbol{k}_0 + \boldsymbol{q}) \approx \Psi_f(\boldsymbol{k}_0) + \frac{q}{k_0}\Psi_f'$, assuming $\frac{q}{k_0} \ll 1$. If vertical transitions, $\Psi_i(\boldsymbol{k}_0) \to \Psi_f(\boldsymbol{k}_0)$, induce a finite photocurrent, the contribution from the photon drag effect is expected to be small. The main interest of this thesis is therefore in the contributions in Eq. (2.34) and we will neglect the photon drag effect from here on. Although we have established that the current given by Eq. (2.34) vanishes in inversion symmetric systems, there can, of course, be terms of higher

order in the electric field and independent of the photon momentum even in inversion symmetric systems. To leading order, however, the photocurrent response to an oscillating electric field is given by Eq. (2.34) [Ganichev and Prettl, 2003].

2.2.1 *Symmetry analysis of CPGE and LPGE*

We now want to study Eq. (2.34) in more detail. The first term vanishes for linearly polarized light and describes the CPGE. This term changes sign when switching between left- and right-circular polarization. The second term is independent of the helicity of the light and describes the LPGE. The photocurrent response to polarized light is restricted by the symmetry properties of the given system and we have already discussed that the CPGE and LPGE vanish in inversion symmetric systems. When studying the photocurrent on the surface of a 3D TI such as Bi_2Se_3, the tensors γ and χ have to be invariant under the surface crystal symmetry operations. In the previous section we have seen that the (111) surface of Bi_2Se_3 exhibits three-fold rotational symmetry about the z-axis and is mirror symmetric about the yz-plane. Starting with γ, we can see by looking at Eqs. (2.33) and (2.34) that γ is actually a pseudotensor. Since γ has to be invariant under the described symmetry operations, the pseudotensor has to obey

$$\gamma = R\gamma R^T \tag{2.35}$$

$$\gamma = -M\gamma M^T, \tag{2.36}$$

where

$$R = \begin{pmatrix} \cos\left(\frac{2\pi}{3}\right) & -\sin\left(\frac{2\pi}{3}\right) & 0 \\ \sin\left(\frac{2\pi}{3}\right) & \cos\left(\frac{2\pi}{3}\right) & 0 \\ 0 & 0 & 1 \end{pmatrix} \tag{2.37}$$

describes the rotation by a multiple of angle $2\pi/3$ around the z-axis and

$$M = \begin{pmatrix} -1 & 0 & 0 \\ 0 & 1 & 0 \\ 0 & 0 & 1 \end{pmatrix} \tag{2.38}$$

describes the reflection about the yz-plane. Evaluating Eq. (2.35) and Eq. (2.36), ones find that γ has only two nonzero elements, i.e., $\gamma_{xy} = -\gamma_{yx} = \gamma$. The photocurrent from the CPGE thus simplifies to

$$j_{CPGE} = i\gamma \left[(E_z E_x^* - E_x E_z^*)\hat{x} - (E_y E_z^* - E_z E_y^*)\hat{y} \right]. \tag{2.39}$$

We can already see that the CPGE response of the Bi$_2$Se$_3$ surface vanishes for normally incident light, i.e., for $E_z = 0$.

We now turn to the second term in Eq. (2.34). As for γ, the crystal symmetry only allows some elements of χ to be nonzero. The surface crystal symmetry operations T, i.e., rotation by $2\pi n/3$ and reflection about the yz-plane, imply

$$\chi_{pqr} = T_{pl} T_{qm} T_{rn} \chi_{lmn}. \tag{2.40}$$

Remembering that χ is symmetric in the last two indices, one finds that χ only has four independent elements given by $\chi_{yyy} = -\chi_{yxx} = -\chi_{xxy} = -\chi_{xyx}$, $\chi_{zyy} = \chi_{zxx}$, $\chi_{yyz} = \chi_{yzy} = \chi_{xxz} = \chi_{xzx}$, and χ_{zzz}. All other elements vanish. The surface current from the LPGE then becomes[2]

$$j_x = -2\chi_{yyy} \left(E_x E_y^* + E_y E_x^* \right) + 2\chi_{yyz} \left(E_x E_z^* + E_z E_x^* \right), \tag{2.41}$$

$$j_y = 2\chi_{yyy} \left(|E_y|^2 - |E_x|^2 \right) + 2\chi_{yyz} \left(E_z E_y^* + E_y E_z^* \right). \tag{2.42}$$

2.2.2 *CPGE and LPGE for arbitrary polarization of light*

For light of arbitrary polarization, generated by a $\lambda/4$ waveplate [see App. A], and incident onto the surface with wavevector

$$\boldsymbol{q} = -q \begin{pmatrix} \sin\theta\cos\varphi \\ \sin\theta\sin\varphi \\ \cos\theta \end{pmatrix} \tag{2.43}$$

in terms of the polar angle θ and the azimuthal angle φ, the electric field can be written as

$$\mathcal{E}(t) = \frac{E_0}{2} e^{-i\omega t + i\boldsymbol{q}\boldsymbol{r}} \begin{pmatrix} -i\sin 2\alpha \sin\varphi + (1 - i\cos 2\alpha)\cos\theta\cos\varphi \\ i\sin 2\alpha \cos\varphi + (1 - i\cos 2\alpha)\cos\theta\sin\varphi \\ -(1 - i\cos 2\alpha)\sin\theta \end{pmatrix} + c.c, \tag{2.44}$$

where $c.c$ denotes complex conjugation. α describes the polarization state (P-linear polarization: $\alpha = 0$; left-circular: $\alpha = \pi/4$; P-linear: $\alpha = \pi/2$; right-circular: $\alpha = 3\pi/4$).

---

2 If the crystal axes do not coincide with the coordinate system used to describe the electric field components, i.e., if the two coordinate systems are oriented at an unknown angle β, one has to rotate χ by β before inserting it into Eq. (2.34). The presented currents are obtained for $\beta = 0$.

Inserting Eq. (2.44) into Eq. (2.39), the photocurrent from the CPGE becomes

$$j_{CPGE} \sim \sin 2\alpha \sin \theta \begin{pmatrix} -\sin \varphi \\ \cos \varphi. \end{pmatrix} \tag{2.45}$$

We see that the current changes sign when switching between left-circular ($\alpha = \pi/4$) and right-circular ($\alpha = 3\pi/4$) polarized light. An important result of Eq. (2.45) is that j_{CPGE} always flows perpendicular to the plane of incidence of the light.

For the LPGE we find the following contributions for light of arbitrary polarization parametrized by α:

$$j_{LPGE} = j_{LPGE,1} \sin 4\alpha + j_{LPGE,2} \cos 4\alpha + j_{LPGE,3}, \tag{2.46}$$

where the direction and magnitude of $j_{LPGE,i}$ depend on the angle of incidence of the light. We see that the contribution to the current originating from the LPGE does not change sign when switching the light's helicity between left-circular ($\alpha = \pi/4$) and right-circular ($\alpha = 3\pi/4$) polarization, i.e., is helicity-independent, and can in general flow in any direction.

In combination, the photocurrent from the CPGE and LPGE perpendicular to the plane of incidence of the light can thus in general be written as

$$j_\perp = C \sin 2\alpha + L_1 \sin 4\alpha + L_2 \cos 4\alpha + D. \tag{2.47}$$

This dependence of the surface photocurrent on the light polarization has been experimentally observed in Bi_2Se_3 [McIver et al., 2012] and will be the focus of Chap. 3. The coefficient C denotes the helicity-dependent contribution from the CPGE and is proportional to the tensor-element γ [cf. Eq. 2.39]. The helicity-independent contributions L_1, L_2, and D originate from the LPGE and thus depend on the non-vanishing elements of χ. Note that the polarization dependence is not unique in the sense that higher-order contributions to the photocurrent, e.g., from the photon-drag effect, can give similar terms.

2.2.3 *Microscopic origin of the CPGE*

It is well known that circularly polarized light can induce a spin-polarized excited carrier distribution in semiconductor systems due to angular momentum selection rules. The sign of the spin polarization then depends on the helicity of

the light. In the spin-helical surface states, any spin-polarized distribution is also asymmetric in momentum space and would carry a net current.

Microscopically, the CPGE occurs due to asymmetric excitation or relaxation processes, as mentioned above. Within the basic mechanism of photocurrent generation, light excites electrons asymmetrically in momentum space. In this section we explain the principle of how such asymmetric excitations using circularly polarized light can occur in spin-helical materials based on the model Hamiltonian of the (111) surface of Bi_2Se_3. While the CPGE in spin-helical systems can be motivated by the following argument, the LPGE usually has more complex origin and depends on the detailed system parameters as indicated by Eq. (2.46).

As seen in Chap. 2, the simplest Hamiltonian for a surface in the xy-plane can be written as [Liu et al., 2010]

$$H = v_F(k_y \sigma_x - k_x \sigma_y), \tag{2.48}$$

where v_F is the Fermi velocity, k_i the in-plane momentum and σ_i describes the electron spin. This Hamiltonian describes linearly dispersing states with an in-plane spin structure locked perpendicular to momentum.

To leading order, the interaction between the surface electrons and light is described by minimal coupling $k \to k - \frac{e}{\hbar}A$, where A is the vector potential of the light and q the photon momentum. For normally incident left circularly polarized light, adopting the convention to determine the handedness by looking in the direction of propagation of the light, the vector potential is given by

$$A = A_0 \begin{pmatrix} \cos(qz - \omega t) \\ -\sin(qz - \omega t) \end{pmatrix}, \tag{2.49}$$

such that the interaction Hamiltonian can be written as

$$
\begin{aligned}
H_{\text{int}} &= -\frac{ev_F}{\hbar}(A_y \sigma_x - A_x \sigma_y) \\
&= -\frac{A_0 ev_F}{2\hbar} \left\{ -ie^{i\omega t - iqz}(\sigma_x - i\sigma_y) + ie^{-i\omega t - iqz}(\sigma_x + i\sigma_y) \right\}.
\end{aligned} \tag{2.50}
$$

The first term in Eq. (2.50) describes the emission and the second the absorption of a photon. Changing the helicity of the light, i.e., taking $\omega \to -\omega$, interchanges the two terms. We see that the interaction with the light is described by spin raising and lowering operators reflecting that the light's spin angular momentum is quantized along the z-direction, i.e., along q. If we vary the angle of incidence of the light, the quantization axis rotates accordingly. Spin-selection rules thus
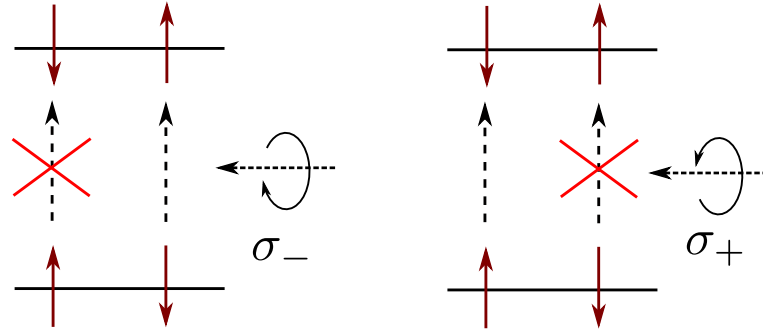
Figure 2.6: While left circularly polarized light preferentially induces transitions from spin-down states to spin-up states but not from spin-up to spin-down, the effect of right circularly polarized light is exactly opposite. For electrons that have opposite spin at opposite momenta this mechanism might lead to excitations which are asymmetric in momentum space.

require that circularly polarized light preferentially couples to spins that are either aligned or anti-aligned to its wavevector, depending on helicity. The effect of the interaction with normally incident circularly polarized light is schematically illustrated in Fig. 2.6. This suggests that for a helical spin structure with spin-momentum locking, as exhibited by the surface electrons of TIs such as Bi_2Se_3, circularly polarized light can excite surface electrons asymmetrically around the Dirac cone and thereby induce a net electric current. Changing the helicity of the light would then change the direction of the current.

This expectation is actually not borne out by the simple model described by Eqs. (2.48) and (2.50). The spin structure of the surface electrons is completely in-plane while the interaction only contains spin raising or lowering operators in the z-direction, i.e., perpendicular to the surface. The light will thus excite carriers symmetrically in momentum space, producing no net current. This can also be seen from symmetry considerations. The Hamiltonian (2.48) is rotationally symmetric about the z-axis and normally incident circularly polarized light does not break this rotational symmetry. Therefore there is no preferred direction for current flow and no net charge current. This result is also in agreement with the symmetry analysis of the previous sections. In Eq. (2.39) we found that a finite z-component of the light field is needed to induce a helicity-dependent photocurrent but the vector potential given by Eq. (2.49) only has in-plane components.

Shining light onto the TI surface at a finite oblique angle breaks the rotational symmetry of the system as seen in Eq. (2.39). Moreover, there are many correc-

tions to the Hamiltonian (2.48), such as hexagonal warping which tilts the spin out of the plane. The z-component of the electron spin has opposite signs for states at $\pm k$ and for positive and negative energies [Fu, 2009; Zhang et al., 2010a; Wang et al., 2011].

As we will review in the following section, photocurrents have indeed been observed on the surface of Bi_2Se_3.

PHOTOCURRENT EXPERIMENTS ON TOPOLOGICAL INSULATORS

As explained in the previous chapter, inversion symmetry is broken at the surface of a 3D TI and one expects a photocurrent response when the surface is illuminated by light. Microscopically, circularly polarized light should excite the spin-helical surface electrons asymmetrically in momentum space leading to a net helicity-dependent photocurrent. Helicity-independent currents could be generated by the LPGE. By the spin-momentum locking, a charge current flowing on the surface would be spin polarized which makes TIs interesting materials for spintronic applications.

When studying transport properties of 3D TIs in experiment one is frequently confronted with the problem that Bi_2Se_3 is naturally n-type with a Fermi level in the bulk conduction band. Transport signatures are thus dominated by bulk contributions masking the topological surface states [Taskin and Ando, 2009; Checkelsky et al., 2009; Peng et al., 2010; Analytis et al., 2010]. Photocurrents that originate from the intrinsic asymmetry near the surface of a 3D TI might therefore prove to be a valuable tool.

In the experimental search for photocurrents in TIs, a large CPGE was first observed in HgTe quantum wells where the structural inversion asymmetry leads to strong Rashba spin-orbit coupling [Wittmann et al., 2010]. The first experiment to measure a helicity-dependent photocurrent on the surface of a 3D TI was performed in 2011 by the Gedik group at MIT [McIver et al., 2012], motivating further experiments on photocurrents in TIs [Kastl et al., 2012; Duan et al., 2014; Kastl et al., 2015a,b]. Due to its importance to this thesis and its comprehensive analysis, we will review the experiment performed by McIver et al. [2012] in detail in the following section.
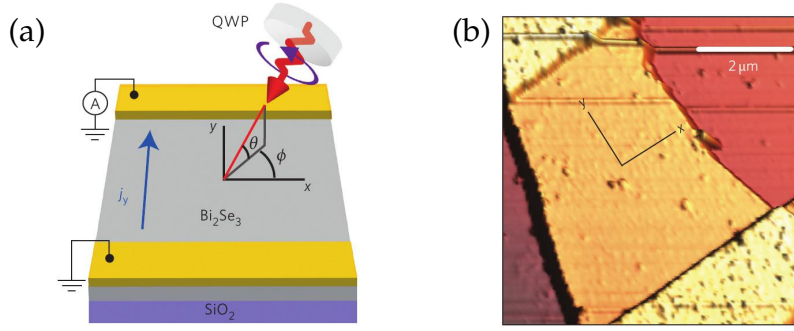
Figure 3.1: (a) Schematic illustration of the experimental setup. Bi_2Se_3 is illuminated by light at an arbitrary angle of incidence and the current is measured along the y-direction. (b) AFM image of a 120 nm thick Bi_2Se_3 device in a two-terminal geometry. Reprinted with permission from [McIver et al., 2012]. Copyright 2011 by Nature Publishing Group.

3.1 EXPERIMENTAL EVIDENCE OF SURFACE PHOTOCURRENTS IN BI2SE3

All the results and figures presented in this section were obtained by McIver et al. [2012].

3.1.1 *Set-up and sample details*

In their experiment McIver et al. [2012] measured photocurrents on the surface of unbiased Bi_2Se_3 devices. The general setup and an AFM image of a typical sample are illustrated in Fig. 3.1. The measurement was done in a two-terminal setup where the current is measured only along the y-direction while varying the laser polarization as well as the angle of incidence. Typical sample sizes were 3.5 μm in width (along x), 5 μm in length (along y), and 120 nm in thickness. As mentioned in Sec. 2.1, the surface states of Bi_2Se_3 extend $\sim$ 2 nm into the bulk, which means that coupling between surfaces can be neglected. Magneto-transport measurements at low temperatures (4 K) show that the samples were electron doped with a bulk carrier density of $n \sim 2 \cdot 10^{17}$ cm^{-3} and a bulk carrier mobility of $\mu \sim 6000 - 8000$ cm^2/Vs.

Figure 3.2: (a) When the laser spot is located directly at the sample center at $y = 0$, laser heating is isotropic excluding possible thermoelectric currents due to heat gradients. (b) The current for the laser spot at $y = 0$ exhibits the linear dependence on the light's intensity characteristic of a photocurrent. Reprinted with permission from [McIver et al., 2012]. Copyright 2011 by Nature Publishing Group.

3.1.2 *Excluding thermoelectric effects*

To induce the photocurrent a 795 nm (1.56 eV) laser was used. The spot size of 100 μm covered the entire sample. Since Bi$_2$Se$_3$ is well known as a good thermoelectric material, a thermoelectric current due to laser heating might mask the intrinsic photocurrent response. In order to rule out thermoelectric contributions to the current, the center of the laser spot was placed directly at the sample center at $y = 0$ so that laser heating should be isotropic [see Fig. 3.2 (a)]. The authors measured the dependence of the resulting current as function of laser intensity as illustrated in Fig. 3.2 (b). Using low laser intensities to minimize laser heating, the current exhibited a linear dependence on the laser intensity which is characteristic of a photocurrent response. At high intensities ~ 1 kW/cm^2, strong deviations from linearity were observed. Systematic photocurrent measurements were thus conducted in the low-intensity regime with $I = 60$ W/cm^2.
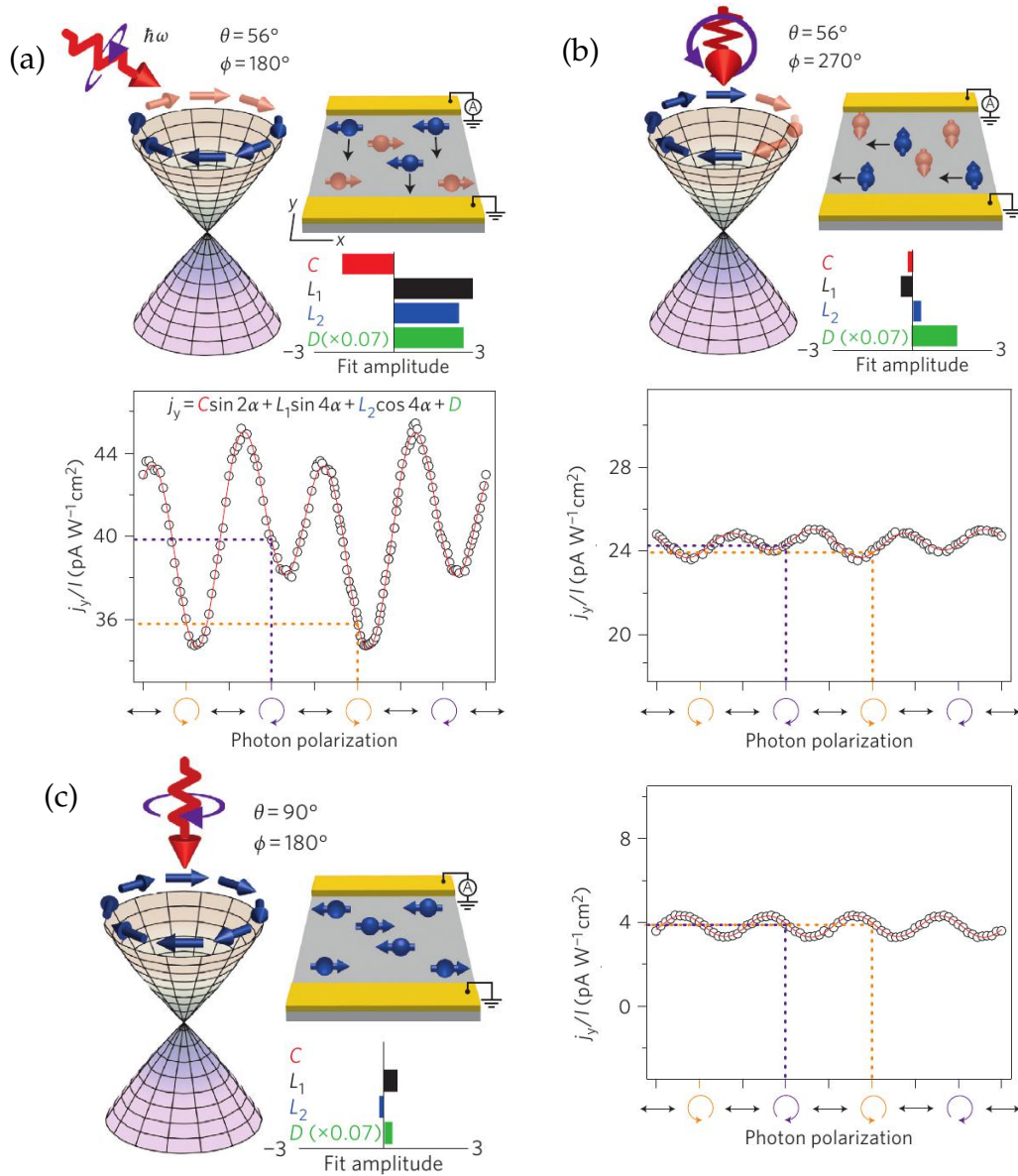
Figure 3.3: Measured photocurrent for various angles of incidence for (a) light obliquely incident perpendicular to the measurement direction, (b) parallel to the measurement direction, and (c) for normal incidence. A significant helicity-dependent contribution to the current is only be measured when light is obliquely incident perpendicular to the measurement direction. Reprinted with permission from [McIver et al., 2012]. Copyright 2011 by Nature Publishing Group.

3.1.3 *Results and interpretation*

The measured laser induced photocurrent response consists of four contributions [cf. Eq. (2.47)]:

$$j_y(\alpha) = C \sin 2\alpha + L_1 \sin 4\alpha + L_2 \cos 4\alpha + D. \qquad (3.1)$$

The coefficients C, L_1, L_2, and D were determined by a fits to the measurement. The angle α describes the degree of polarization [cf. Eq. (2.44)] (*P*-linearly polarized: $\alpha = 0$: left-circular: $\alpha = \pi/4$; *P*-linear: $\alpha = \pi/2$; right-circular: $\alpha = 3\pi/4$). This polarization dependence of the measured photocurrent is consistent with the symmetry analysis in the previous chapter given by Eqs. (2.45) and (2.46). C can thus be identified as the helicity-dependent component of the current, as this contribution changes sign with helicity and vanishes for linear polarization. The contribution L_1 vanishes for circularly polarized light and the contribution L_2 is the same for left- or right-circularly polarized light. The contributions L_1 and L_2 are thus both helicity-independent while the contribution D is completely polarization independent.

The magnitude of the various contributions strongly depends on the angle of incidence of the laser. The results are illustrated in Fig. 3.3 for three different angles of incidence. For oblique incidence in the *xz*-plane [Fig. 3.3 (a)] the photocurrent has a finite helicity-dependent contribution. C, L_1, and L_2 are of the same order of magnitude and the polarization independent background D is approximately two orders of magnitude larger. For oblique incidence in the *yz*-plane [Fig. 3.3 (b)] the photocurrent is reduced and the helicity-dependent contribution becomes negligible. For normal incidence [Fig. 3.3 (c)] the photocurrent is reduced even further and there is no helicity-dependent contribution.

The helicity dependence in combination with the strong dependence on the angle of incidence, indicates that the photocurrent proportional to C originates from the surface states. The dependence of the helicity-dependent photocurrent on the angle of incidence is in complete agreement with the symmetry analysis given by Eq. (2.45). The helicity-dependent contribution C vanishes for normal incidence and flows perpendicular to the plane of incidence, i.e., C vanishes when light is incident in the *yz*-plane parallel to the measurement direction.

This behavior of the helicity-dependent contribution can also be understood from a microscopic point of view. Surface state electrons in 3D TIs at opposite momenta have opposite spin. Circular polarized light interacts preferably

with spins that are either parallel or antiparallel to the wavevector of the light depending on the helicity [Meier and Zakharchenya, 1984] [cf. Sec. 2.2.3]. This means that left circularly polarized light preferably excites electrons at, say, $+k$ but not at $-k$, creating asymmetric excitations in momentum space. Changing the helicity of the light would then preferably excite electrons at $-k$ but not at $+k$ creating a current that flows in the opposite direction. In total this would lead to a helicity-dependent current which agrees with the observations. In addition, we know that electron spin and momentum are locked perpendicular to each other and that the spins lie mostly in-plane. Circularly polarized light incident in the xz-plane preferably couples to spins that also lie in the xz-plane. Due to spin-momentum locking this would create a helicity-dependent current along the y-direction, in agreement with the results of Fig. 3.3 (a). Circularly polarized light incident in the yz-plane would induce a helicity-dependent current along the x-direction. Since the experimental setup only captures current flowing along the y-direction, there should be no helicity-dependent contribution, in agreement with the experiment. Last, for normal incidence of the laser, electrons with spin along the z-direction would be preferably excited. Since the spin-structure is, however, mostly in-plane, normal incidence would lead to excitations that are isotropic in momentum space [cf. Sec. 2.2.3]. Even with warping which tilts the spins out of plane, the spin structure has a trigonal symmetry around the Dirac cone, due to the rotational symmetry of the crystal surface [cf. Fig. 2.1]. Excitations would reflect this symmetric in momentum space, which precludes a finite charge current. Thus for normal incidence there should indeed be no helicity-dependent photocurrent.

The observed helicity-dependent photocurrent C is therefore in agreement with a surface-state origin. We have, however, not yet discussed whether such a contribution can also originate from the bulk. Naively, the helicity-dependent contribution cannot have bulk origin, since the bulk of Bi_2Se_3 is inversion symmetric and a CPGE is not allowed. The crystal exhibits inversion symmetry, the bulk states are spin-degenerate, and thus cannot induce a helicity-dependent photocurrent. Real Bi_2Se_3 samples, however, experience band bending near the surface when being exposed to the environment after cleaving, leading to the formation of a two-dimensional electron gas (2DEG) at the inversion layer [Xia et al., 2009; Hsieh et al., 2009a; Bianchi et al., 2010]. This 2DEG coexists with the Dirac cone near the surface. The resulting electric field in the inversion layer induces Rashba spin-splitting [Xia et al., 2009; Bianchi et al., 2010] and spin-split QW states can also induce a CPGE [Ganichev and Prettl, 2003]. McIver et al. [2012] argue that the measured response is unlikely to originate from the 2DEG. ARPES measurements of the band structure were performed after cleaving in UHV and several
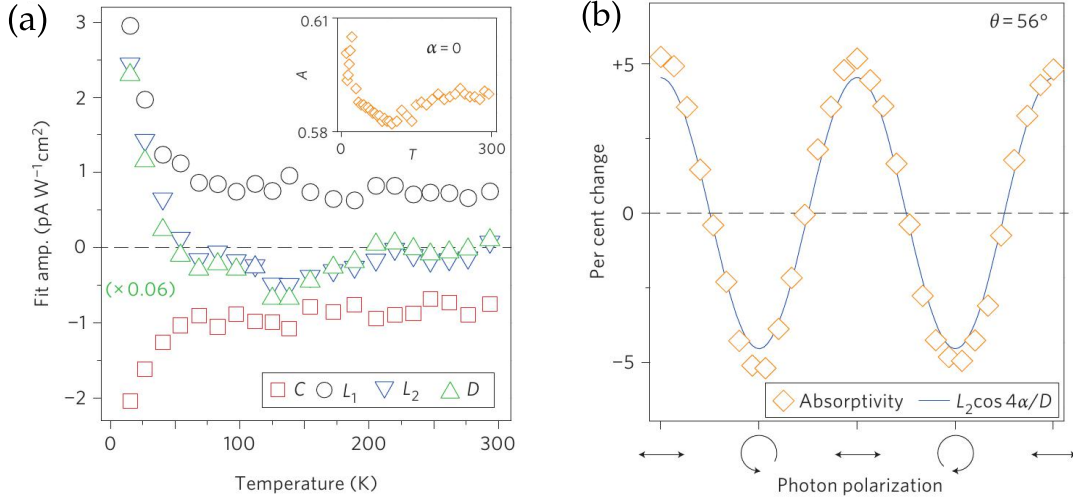
Figure 3.4: (a) Temperature dependence of the various contributions to the photocurrent. Inset: optical absorptivity of P-polarized light at oblique incidence as a function of temperature. (b) Dependence of the change in absorptivity as a function of light polarization measured at room temperature. Reprinted with permission from [McIver et al., 2012]. Copyright 2011 by Nature Publishing Group.

hours later at room temperature and no evidence for Rashba split bands was found. Even though the device fabrication might induce additional electron doping, the helicity-dependent photocurrent response from the Rashba split bands is expected to be small [Yazyev et al., 2010]. The reason is that, in contrast to the helical Dirac surface states, the 2DEG has two Fermi surfaces with opposite spin polarizations. Electrons that have the same spin can propagate in opposite directions and thus there is a cancellation effect between left and right movers. For Rashba SOC $\alpha\hbar(\mathbf{k} \times \sigma)_z$, the current would be proportional to the SOC coupling strength α. For the Dirac surface states, in contrast, the current would be proportional to the Fermi velocity v_F. Since one expects $\alpha \ll v_F$ [Xia et al., 2009; Chen et al., 2009], the only way the CPGE from the 2DEG could dominate the response is if the inversion layer protrudes far into the bulk. An estimate of the inversion layer depth from the bulk carrier density, average effective mass and dielectric constant lead to penetration lengths of the inversion layer that are similar to the penetration lengths of the surface states and McIver et al. [2012] conclude that the CPGE from the surface states is expected to dominate the response.

The magnitude of the photocurrent is actually temperature dependent since the transition probability is affected by the thermal broadening of the interband transitions based on electron-phonon interactions [Lautenschlager et al., 1987] and

by the broadening of the Fermi distribution function. To analyze the origin of the other contributions L_1, L_2, and D to the photocurrent, the temperature dependence of the various components was studied. The results are illustrated in Fig. 3.4 (a). The similar behavior of C and L_1 indicate that L_1 may also have surface-state origin. L_2 and D show a similar temperature dependence, but the behavior differs from that of C and L_1. Thus L_2 and D probably share the same origin. This is further corroborated by analyzing the dependence of the absorptivity on photon polarization. Fig. 3.2 (b) shows that the absorptivity is well fitted by $L_2/D \cos 4\alpha$. Since the absorptivity is connected to the bulk index of refraction [Hecht, 1998], L_2 and D are concluded to have bulk origin.

3.2 SUMMARY

In their experiment McIver et al. [2012] measured surface photocurrents in the 3D TI Bi_2Se_3. They analyzed the polarization dependence of the current and found a contribution that changes sign when switching between left- and right-circular polarization. This helicity-dependent contribution to the photocurrent vanishes when the laser is incident parallel to the measurement direction. The polarization dependence of the current is consistent with the phenomenological model of the CPGE discussed in Chap. 2 and a Dirac cone origin. Further experimental evidence of surface photocurrents on Bi_2Se_3 was obtained by Duan et al. [2014]. Using a similar experimental setup as discussed above, Duan et al. [2014] reported the observation of a helicity-dependent photocurrent response with Dirac cone origin.

Since both experiments used photon energies larger than the bulk band gap, a Dirac cone origin of the contributions C and L_1 implies that these photocurrents are generated by transitions between surface and bulk states, i.e., excitations from the bulk valence band into the surface Dirac cone or from the Dirac cone into the bulk conduction band. Since L_2 and D are concluded to have bulk origin, they should be generated by transitions from the bulk valence band into the bulk conduction band. The LPGE, however, vanishes in the inversion symmetric bulk and thus L_2 and D are probably generated by higher-order processes, such as the photon-drag effect. C and L_1, on the other hand, can originate from the CPGE and LPGE, respectively.

In order to understand the microscopic origin of C and L_1, in Chap. 5 we theoretically study the photocurrent generation in the regime where the photon

energy exceeds the band gap and consider transitions that involve the surface Dirac cone. This analysis is, however, analytically involved and in Chap. 4 we will therefore first consider the regime where excitations take place within the Dirac cone. The band gap of Bi_2Se_3 is large, ~ 300 meV, and for a Fermi level near the Dirac point THz radiation would excite electrons from the lower to the upper part of the Dirac cone. CPGE and LPGE are allowed and we expect a photocurrent response. Thus, before including the bulk states in Chap. 5, we give a detailed analysis of photocurrent generation within a pure surface-state model in the following chapter.

4

PHOTOCURRENT RESPONSE OF TOPOLOGICAL INSULATOR SURFACE STATES

The helical nature of surface states is expected to lead to a rather unique photocurrent response to electromagnetic radiation [Raghu et al., 2010; Hosur, 2011; Ganichev and Prettl, 2003]. In order to understand the microscopic processes involved, we study the photocurrent generation within a minimal model of a TI surface and focus on the current induced by asymmetric excitations in momentum space [cf. Fig. 4.1 (a)].

The content and results of this chapter were previously published as [Junck et al., 2013].

4.1 INTRODUCTION

Our model is motivated by Bi_2Se_3, the 3D TI used in the experiment, and we focus on the surface states in this chapter. In the first part, we consider the interaction with circularly polarized light before generalizing to arbitrary polarization at the end of the chapter.

The surface crystal structure of Bi_2Se_3 exhibits trigonal rotational symmetry which precludes a photocurrent response for normally incident circularly polarized light [cf. Chap. 2]. We therefore consider oblique incidence of the light which breaks the rotational symmetry [cf. Fig. 4.1 (c)]. Microscopically, one then expects that circularly polarized light leads to excitations that occur asymmetrically in momentum space [cf. Sec. 2.2.3, Fig. 4.1 (a)] and thus to a photocurrent response as experimentally observed by McIver et al. [2012].

We find, however, that the photocurrent for the usual minimal coupling between light and electrons, $\boldsymbol{p} \to \boldsymbol{p} - e\boldsymbol{A}$, vanishes in a pure surface-state model even for oblique incidence. While this may seem surprising, we show that a symmetry analysis explains the vanishing photocurrent. Only when we include the small Zeeman coupling between the surface-electron spin and the magnetic field of the light do we find a photocurrent response in the pure surface-state model. The leading contribution results from an interference between orbital and Zeeman coupling and is helicity independent. We also find a helicity-dependent contribution to the photocurrent as measured in the experiment and suggested by the simple mechanism illustrated in Fig. 4.1 (a). This contribution is, however, very small as it is quadratic in the Zeeman coupling.

The photocurrent response of the surface states of Bi_2Se_3 to circularly polarized light has been studied previously. Hosur [2011] considered normal incidence and included an in-plane magnetic field to break the rotational symmetry. He found a leading order contribution to the photocurrent $\sim \lambda B^2$, with warping λ [Fu, 2009; Wang et al., 2011; Basak et al., 2011] and magnetic field B. We find, however, that to the order considered by Hosur [2011], the photocurrent actually vanishes. A finite photocurrent response for minimal coupling requires additional perturbations to the Dirac spectrum such as a momentum-dependent correction to the Fermi velocity [Fu, 2009].

4.2 PERFECT DIRAC CONE

Before presenting the full analysis including the Zeeman coupling and the in-plane magnetic field, we now first consider the perfect Dirac cone for obliquely incident circularly polarized light. We choose the surface to lie in the xy-plane and motivated by the (111) surface of Bi_2Se_3, we consider the model Hamiltonian [cf. Sec. 2.1]

$$H = v_F(p_x \sigma_y - p_y \sigma_x),$$ (4.1)

where v_F is the Fermi velocity. The chemical potential and the energy $\hbar\omega$ of the incident radiation are tuned such that electrons are only excited within the Dirac cone within the bulk band gap ($E_{\text{gap}} = 0.3$ eV for Bi_2Se_3 [Xia et al., 2009; Zhang et al., 2009a]) [cf. Fig. 2.3]. This Hamiltonian is particle-hole symmetric, $H|\boldsymbol{p}, \pm\rangle = \pm E|\boldsymbol{p}, \pm\rangle$, with

$$E = v_F p.$$ (4.2)
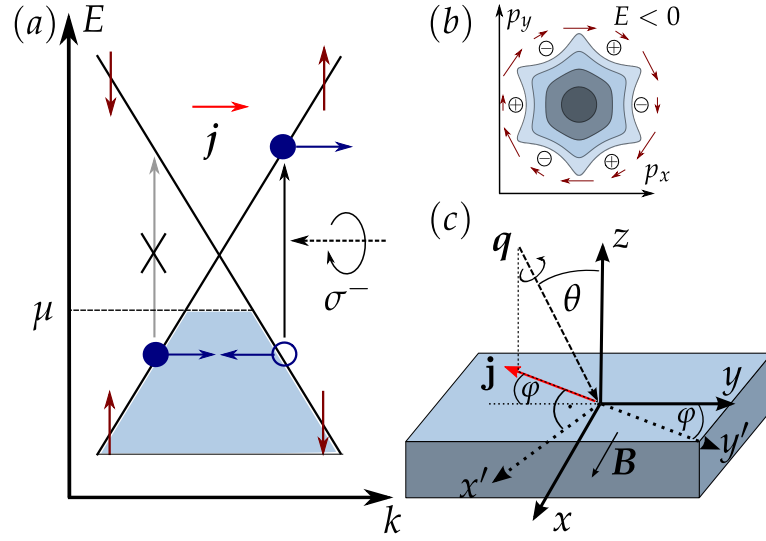
Figure 4.1: (a) Basic principle for the generation of a helicity-dependent photocurrent (cf. Fig. 2.6). The spin direction is indicated by dark red arrows and filled and empty circles indicate electrons and holes, respectively. Circularly polarized light leads to spin-dependent transitions and electrons are excited asymmetrical in momentum space. (b) Illustration of the warping effect on the constant energy contours. Lighter colors/shades correspond to larger absolute values of energy. The in-plane spin orientation is again indicated by dark red arrows, circles with $+(-)$ indicate positive (negative) spin z-component. (c) Illustration of the orientation of the surface, the direction of the incident light q, and the resulting main contribution to the current j.

We consider left-circularly polarized light obliquely incident onto the sample as illustrated in Fig. 4.1 (c),

$$
A(t) = \frac{A_0}{2} e^{-i\omega t + iqr}
\begin{pmatrix}
\cos\varphi + i\cos\theta\sin\varphi \\
-\sin\varphi + i\cos\theta\cos\varphi \\
i\sin\theta
\end{pmatrix} + c.c,
\tag{4.3}
$$

with polar angle $\theta \in [0, \pi/2]$ and the azimuthal angle φ defined from the negative y-axis, such that light is incident in the yz-plane for $\varphi = 0$, i.e., a mirror plane of the sample. The direction of propagation of the light q is given by

$$
\hat{q} =
\begin{pmatrix}
\sin\theta\sin\varphi \\
\sin\theta\cos\varphi \\
-\cos\theta
\end{pmatrix}.
\tag{4.4}
$$

For $\varphi = 0$, $\boldsymbol{q}$ lies in the yz-plane at an angle θ from the positive z-axis, such that $\hat{\boldsymbol{q}} = \sin\theta\,\hat{\boldsymbol{y}} - \cos\theta\,\hat{\boldsymbol{z}}$ [see Fig. 4.1]. The interaction Hamiltonian for minimal coupling between light and electrons, $\boldsymbol{p} \to \boldsymbol{p} - e\boldsymbol{A}$, is then given by

$$H' = -e\frac{\partial H}{\partial \boldsymbol{p}} \cdot \boldsymbol{A}. \tag{4.5}$$

The contributions of the vector potential $\propto e^{\pm i\omega t}$ lead to the emission and absorption of photons, respectively. In order to distinguish these processes we write the interaction Hamiltonian as $H' = H'_+ + H'_-$ with $H'_\pm \propto A_\pm = A_0 e^{\pm i\omega t}$ corresponding to the recombination (H_+) and creation (H_-) of electron-hole pairs by emission and absorption of photons.

4.2.1 *Derivation of the photocurrent density*

For a system without spin degeneracy the current density in two dimensions can be written as

$$\boldsymbol{j} = -e\sum_{\beta=\pm}\sum_{\boldsymbol{p}} \boldsymbol{v}_{\boldsymbol{p},\beta}(n_{\boldsymbol{p},\beta} - n^0_{\boldsymbol{p},\beta}), \tag{4.6}$$

where $\pm$ denotes the positive- and negative-energy band, respectively, $n_{\boldsymbol{p},\beta}$ ($n^0_{\boldsymbol{p},\beta}$) is the distribution function (equilibrium distribution function) of momentum state $\boldsymbol{p}$ in band β, and $\boldsymbol{v}_{\boldsymbol{p},\beta}$ is the velocity of a particle in state $\boldsymbol{p}$ in band β. The expression for the current given by Eq. (4.6) only contains deviations from equilibrium $n_{\boldsymbol{p}} - n^0_{\boldsymbol{p}}$ since filled bands do not carry a net charge current. We can determine the out-of-equilibrium distribution $n_{\boldsymbol{p},\pm}$ by studying the Boltzmann equation

$$\frac{dn_{\boldsymbol{p},\pm}}{dt} = \pm\Gamma_{|\boldsymbol{p},-\rangle\to|\boldsymbol{p},+\rangle}(n^0_{\boldsymbol{p},-} - n^0_{\boldsymbol{p},+}) + I_{\text{relax}}\left[n_{\boldsymbol{p},\pm}\right], \tag{4.7}$$

where we consider vertical transitions in momentum space as usual, i.e., we neglect the photon momentum. Here Γ is the transition rate from state $|\boldsymbol{p},-\rangle$ in the lower band to state $|\boldsymbol{p},+\rangle$ in the upper band, i.e., it describes processes that fill the state $|\boldsymbol{p},+\rangle$. $I_{\text{relax}}\left[n_{\boldsymbol{p},\pm}\right]$ is a collision integral that describes relaxation of particles in state $|\boldsymbol{p},\pm\rangle$ and that in general can be of complicated form. For small deviations from equilibrium, however, we can apply the relaxation time approximation. Assuming that momentum relaxation occurs on a much faster

timescale than energy relaxation and that electrons and holes relax at the same rate, the collision integral becomes

$$I_{\text{relax}}\left[n_{p,\pm}\right] = -\frac{n_{p,\pm} - n_{p,\pm}^0}{\tau_p},$$ (4.8)

where τ_p is the momentum relaxation time. The steady-state solution of the Boltzmann equation in relaxation time approximation thus gives

$$n_{p,\pm} - n_{p,\pm}^0 = \pm\tau_p\,\Gamma_{|p,-\rangle\to|p,+\rangle}(n_{p,-}^0 - n_{p,+}^0).$$ (4.9)

The transition rate Γ can be calculated using Fermi's Golden Rule. For $T = 0$, the equilibrium distribution functions become Heaviside stepfunctions and $(n_{p,-}^0 - n_{p,+}^0)$ in Eq. (4.9) is only nonzero if the state $|p, -\rangle$ is occupied and the state $|p, +\rangle$ is unoccupied. This implies that the chemical potential has to lie between the energies of the two states participating in the transition [cf. Fig. 4.1] which gives a condition for the minimum photon energy required to induce transitions.

Assuming $\hbar\omega/2 > |\mu|$ for the photon energy with μ measured from the Dirac point, the current density becomes

$$j = -\frac{4\pi e \tau_p}{\hbar} \sum_p v_{p,+} |\langle p, +|H'_-|p, -\rangle|^2 \delta(2E - \hbar\omega),$$ (4.10)

where we used that $v_{p,+} = -v_{p,-}$ and $E_{p,+} = -E_{p,-} = E$ due to particle-hole symmetry.

4.2.2 *Vanishing photocurrent response*

Using Eqs. (4.1)-(4.5) the photocurrent density given by Eq. (4.10) can be evaluated in a straightforward manner leading to

$$j \propto \int_0^{2\pi} d\phi \begin{pmatrix} \cos\phi \\ \sin\phi \end{pmatrix} |A_x \sin\phi - A_y \cos\phi|^2 = 0,$$ (4.11)

where $\tan\phi = p_y/p_x$ and $A_{x,y}$ are the in-plane components of the vector potential. Thus, the photocurrent from the CPGE and LPGE vanishes for arbitrary angles of incidence.

The surprising result that even for oblique incidence circularly polarized light does not lead to a net photocurrent for orbital coupling, can be explained by the symmetry of the problem. The symmetry analysis in Chap. 2 revealed that the CPGE requires a nonzero z-component of the electric field, i.e.,

$$j_{CPGE} = i\gamma \left[(E_z E_x^* - E_x E_z^*)\hat{x} - (E_y E_z^* - E_z E_y^*)\hat{y} \right]. \tag{4.12}$$

For the full rotational symmetry of the Dirac cone, the current from the LPGE becomes [cf. Eq. (2.42)]

$$j_{LPGE} = 2\chi_{yyz} \left(E_x E_z^* + E_z E_x^* \right) \hat{x} + 2\chi_{yyz} \left(E_z E_y^* + E_y E_z^* \right) \hat{y}, \tag{4.13}$$

i.e., also requires a finite E_z. The interaction Hamiltonian in Eq. (4.5), $H' = -ev_F(A_x\sigma_y - A_y\sigma_x)$, however, does not contain any dependence on A_z and by $E = -\partial_t A$ also no dependence on E_z.

Microscopically the Hamiltonian (4.1) is invariant under the unitary transformation

$$\mathcal{U} = e^{i\pi\left(\hat{L}_z + \frac{1}{2}\sigma_z\right)}, \tag{4.14}$$

which describes a rotation of π about the z-axis in orbital and spin space. Under this transformation we find

$$\mathcal{U}H\mathcal{U}^\dagger = H \tag{4.15}$$

$$\mathcal{U}H'\mathcal{U}^\dagger = -H' \tag{4.16}$$

$$\mathcal{U}\hat{j}\mathcal{U}^\dagger = \mathcal{U}\frac{\partial H}{\partial \boldsymbol{p}}\mathcal{U}^\dagger = -\hat{j}. \tag{4.17}$$

While the current changes sign, the right hand side of Eq. (4.10) remains invariant under this transformation and we find $j = -j$. Thus the photocurrent has to vanish.

4.3 PERFECT DIRAC CONE WITH ZEEMAN COUPLING

An electromagnetic wave, however, is not only described by an electric-field component through $E = -\partial_t A$ but also through a magnetic field given by $\nabla \times A$. Considering the small Zeeman coupling between light and electron spin in addition to the minimal coupling, the interaction Hamiltonian becomes

$$H' = -e\frac{\partial H}{\partial \boldsymbol{p}} \cdot A - g_s\mu_B(\nabla \times A) \cdot \hat{\boldsymbol{\sigma}}, \tag{4.18}$$

where g_s is the spin g-factor, μ_B the Bohr magneton, $\hat{\sigma}$ the vector of Pauli matrices and H is given by Eq. (4.1). Usually one expects that the orbital coupling is the dominant mechanism and that Zeeman coupling is strongly suppressed with respect to the leading contribution. Quantitatively the relative magnitude of Zeeman and orbital coupling can be estimated as $\sim \hbar q/2mv_F = \hbar\omega/2mv_F c$. For a photon energy of $\hbar\omega = 0.1$ eV and a Fermi velocity of $v_F = 5 \cdot 10^5$ m/s [Liu et al., 2010], this ratio is of order $\sim 10^{-5}$. Indeed orbital coupling is clearly the dominant excitation process. As we have shown above, orbital coupling, however, leads to a vanishing photocurrent. We therefore include Zeeman coupling into our analysis.

A straightforward evaluation of the photocurrent given by Eq. (4.10) with the interaction Hamiltonian Eq. (4.18) leads to

$$j_x \propto iev_F \left(B_z^* A_y - B_z A_y^* \right) - ig_s\mu_B \left(B_x B_z^* - B_x^* B_z \right) \qquad (4.19)$$

$$j_y \propto -iev_F \left(B_z^* A_x - B_z A_x^* \right) - ig_s\mu_B \left(B_y B_z^* - B_y^* B_z \right). \qquad (4.20)$$

Using the vector potential Eq. (4.3) we find a finite photocurrent that is given by

$$\boldsymbol{j}^{(0)} = - C\bar{v}_Z \sin\theta \left(\hat{\boldsymbol{y}}' - \bar{v}_Z \hat{\boldsymbol{x}}' \right), \qquad (4.21)$$

where $C = \frac{e^3 E_0^2 v_F \tau_p}{8\omega\hbar^2}$, $\bar{v}_Z = \frac{g_s\hbar\omega}{2mcv_F}$, and $\hat{\boldsymbol{x}}'$, $\hat{\boldsymbol{y}}'$ define a rotated coordinate system such that $\boldsymbol{A}$ is incident in the $y'z$-plane [cf. Fig. 4.1 (c)]. Note that these two contributions to the current along $\hat{\boldsymbol{x}}'$ and $\hat{\boldsymbol{y}}'$, i.e., perpendicular and parallel to the plane of incidence of the light, have very different polarization dependencies. $j_{y'}^{(0)}$ is helicity independent and results from interference of orbital and Zeeman coupling. $j_{x'}^{(0)}$ is purely induced by the Zeeman coupling, thus much smaller than $j_{y'}^{(0)}$, and helicity dependent. As we will see below, the helicity-independent contribution $j_{y'}^{(0)}$ can also be generated by S-linearly polarized light, i.e., by light which is linearly polarized perpendicular to the plane of incidence. The helicity-dependent contribution $j_{x'}^{(0)}$ vanishes for linear polarization. Both contributions to the current vanish for $\theta = 0$, i.e., for normal incidence.

We can also estimate the currents given by Eq. (4.21) quantitatively. For a laser power of 1 W/mm^2 as well as the parameters $g = g_s = 1$ and $v_Z = \frac{g_s\hbar\omega}{2mc} = 29$ m/s we find $j_{y'}^{(0)} \sim 10$ μA/m and $j_{x'}^{(0)} \sim 1$ nA/m for the current densities parallel and perpendicular to the plane of incidence, respectively. While for normal

incidence the current completely vanishes, for oblique incidence the dominant contribution is by far the helicity-independent current in the y'-direction since $\bar{v}_Z \sim 10^{-5}$ [cf. Fig. 4.1].

4.3.1 *Symmetry analysis*

The photocurrent given by Eqs. (4.19)-(4.21) can be explained by the following symmetry considerations. In Sec. 2.2 we discussed the symmetry properties of the CPGE and LPGE which are quadratic in the electric field. The Zeeman coupling is proportional to the photon momentum by $\boldsymbol{B} = \nabla \times \boldsymbol{A} \propto q$ and is thus a photon drag contribution. Since we consider vertical transitions in momentum space, we do not have to consider the full fourth-rank photon drag tensor (or even fifth rank for terms of order $\sim q^2$) but can phenomenologically describe the photocurrent response to the magnetic field analogously to the discussion of the CPGE and LPGE in Sec. 2.2.[1] Specifically the photocurrent response to first and second order in the magnetic field can be written as

$$j_\lambda^{(B)} = \tau_{\lambda\mu\nu}^{(1)} \left(E_\mu B_\nu^* + E_\mu^* B_\nu \right) + i\tau_{\lambda\mu\nu}^{(2)} \left(E_\mu B_\nu^* - E_\mu^* B_\nu \right) \tag{4.22}$$

$$j_\lambda^{(B^2)} = \gamma_{\lambda\mu}^{(B)} i (\boldsymbol{B} \times \boldsymbol{B}^*)_\mu + \chi_{\lambda\mu\nu}^{(B)} (B_\mu B_\nu^* + B_\mu^* B_\nu), \tag{4.23}$$

where $\boldsymbol{\tau}^{(1,2)}$ are real third-rank pseudotensors, $\gamma^{(B)}$ is a real second-rank pseudotensor, and $\chi^{(B)}$ is a real third-rank tensor. Under the surface crystal symmetry operations of Bi$_2$Se$_3$, i.e., three-fold rotational symmetry about the z-axis and a mirror plane in the yz-plane, $\gamma^{(B)}$ and $\chi^{(B)}$ transform exactly as shown for the CPGE and LPGE in Sec. 2.2.1. For the pseudotensor $\boldsymbol{\tau}^{(1,2)}$ we find four independent elements, $\tau_{xxx} = -\tau_{yyx} = -\tau_{yxy} = -\tau_{xyy}$, $\tau_{xyz} = -\tau_{yxz}$, $\tau_{xzy} = -\tau_{yzx}$, and $\tau_{zxy} = -\tau_{zyx}$. Under full rotational symmetry we additionally find $\tau_{xxx} = -\tau_{yyx} = -\tau_{yxy} = -\tau_{xyy} = 0$.

Thus under full rotational symmetry we find

$$\begin{aligned} j_x^{(B)} =& \tau_{xyz}^{(1)} (E_y B_z^* + E_y^* B_z) + i\tau_{xyz}^{(2)} (E_y B_z^* - E_y^* B_z) \\ &+ \tau_{xzy}^{(1)} (E_z B_y^* + E_z^* B_y) + i\tau_{xzy}^{(2)} (E_z B_y^* - E_z^* B_y), \end{aligned} \tag{4.24}$$

$$\begin{aligned} j_y^{(B)} =& -\tau_{xyz}^{(1)} \left(E_x B_z^* + E_x^* B_z \right) - i\tau_{xyz}^{(2)} \left(E_x B_z^* - E_x^* B_z \right) \\ &- \tau_{xzy}^{(1)} \left(E_z B_x^* + E_z^* B_x \right) - i\tau_{xzy}^{(2)} \left(E_z B_x^* - E_z^* B_x \right) \end{aligned} \tag{4.25}$$

---

1 Note that we also calculated the photon drag contribution from minimal coupling and transitions $|\boldsymbol{p}, -\rangle \to |\boldsymbol{p} + \boldsymbol{q}, +\rangle$ but find that the current is at least of cubic order in the photon momentum.

and

$$j_x^{(B^2)} = i\gamma^{(B)}(B_z B_x^* - B_x B_z^*) + 2\chi_{yyz}^{(B)}(B_x B_z^* + B_z B_x^*), \tag{4.26}$$

$$j_y^{(B^2)} = i\gamma^{(B)}(B_z B_y^* - B_y B_z^*) + 2\chi_{yyz}^{(B)}(B_y B_z^* + B_z B_y^*). \tag{4.27}$$

One can see that for normal incidence, $B_z = E_z = 0$, the photocurrent vanishes.

Considering again the microscopic transformation given by Eq. (4.14), we find that additional contributions to the current have to vanish. Under the transformation (4.14) the interaction Hamiltonian including Zeeman coupling behaves as

$$\mathcal{U}H'\mathcal{U}^\dagger = -H'(-B_z), \tag{4.28}$$

with $B_z = (\nabla \times A)_z$. The transformation of the interaction Hamiltonian is no longer described by just an overall minus sign, but the z-component of the magnetic field also acquires a minus sign. Thus we find that non-vanishing currents of the form $j \propto B_z^{2n+1}$ with integer n are allowed. For the leading order photocurrent we obtain

$$j \propto B_z, \tag{4.29}$$

in agreement with our calculated result given by Eqs. (4.19) and (4.20). By this symmetry, all currents in Eqs. (4.24) and (4.25) that are independent of B_z have to vanish and the photocurrent response to the magnetic field simplifies to

$$j_x^{(B+B^2)} = \tau_{xyz}^{(1)}(E_y B_z^* + E_y^* B_z) + i\gamma^{(B)}(B_z B_x^* - B_x B_z^*)$$
$$+ i\tau_{xyz}^{(2)}(E_y B_z^* - E_y^* B_z) + 2\chi_{yyz}^{(B)}(B_x B_z^* + B_z B_x^*) \tag{4.30}$$

$$j_y^{(B+B^2)} = -\tau_{xyz}^{(1)}(E_x B_z^* + E_x^* B_z) + i\gamma^{(B)}(B_z B_y^* - B_y B_z^*)$$
$$- i\tau_{xyz}^{(2)}(E_x B_z^* - E_x^* B_z) + 2\chi_{yyz}^{(B)}(B_y B_z^* + B_z B_y^*). \tag{4.31}$$

The first lines in the Eqs. (4.30) and (4.31) exactly constitute our result presented in Eqs. (4.19) and (4.20) when considering $E = -\partial_t A$. We find that the current linear in the Zeeman coupling, i.e., linear in B, is helicity-independent, while the contribution quadratic in the Zeeman coupling is helicity-dependent. One might be able to explain the vanishing of the remaining terms in the second lines by considering symmetries that affect the helicity of the light.

One could have anticipated the helicity-dependence of the result (4.21) by again considering the symmetry of the problem. We know that the (111) surface of Bi$_2$Se$_3$ has trigonal rotational symmetry (including warping) and a mirror axis along the y-direction [Fu, 2009]. For oblique incidence, consider light that is

incident in the yz-plane. Reflection about the mirror axis along y changes the helicity. In addition, the reflection changes the sign of a current along the x-direction while a current along the y-direction remains invariant. Thus, a helicity-dependent current can only flow along the x-direction, i.e., perpendicular to the plane of incidence, while a helicity-independent current can flow only in the y-direction, i.e. parallel to the plane of incidence. Without warping, $\lambda = 0$, the system has full rotational symmetry and the only directionality is provided by the vector potential. Consequently, when the vector potential is rotated away from the yz-plane, the current will rotate accordingly.

These results can also be deduced by studying the interaction Hamiltonian. For a perfect Dirac spectrum and $\varphi = 0$, the relevant interaction Hamiltonian given by Eq. (4.18) becomes

$$H'_- \sim v_F \left(\sigma_y - i \cos\theta \sigma_x \right) - v_Z \left(\sigma_x + i \cos\theta \sigma_y + i \sin\theta \sigma_z \right), \qquad (4.32)$$

where the first term describes the orbital coupling and the second the Zeeman interaction. For normal incidence ($\theta = 0$), both orbital and Zeeman coupling are proportional to the spin raising operator the z-direction, $\sigma_+ = \sigma_x + i\sigma_y$. Since for $\lambda = 0$ all spins lie in plane, excitations take place isotropically around the Dirac cone. We arrive at the expected result that for normal incidence no net current is induced. For oblique incidence ($\theta \neq 0$), the orbital coupling is proportional to a sum of spin raising and lowering operators in the z-direction since $\sigma_y - i \cos\theta \sigma_x = -i/2[\sigma_+(1 + \cos\theta) - \sigma_-(1 - \cos\theta)]$. For an in-plane spin distribution this again excites electrons isotropically around the Dirac cone and we see that the orbital coupling by itself cannot generate a finite photocurrent. The Zeeman coupling, however, includes for oblique incidence a term $\sigma_x + i \sin\theta \sigma_z = i/2[(\sigma_z - i\sigma_x)(1 + \sin\theta) - (\sigma_z + i\sigma_x)(1 - \sin\theta)]$, which is a sum of spin raising and lowering operators in the y-direction. Since the spin lowering operator $\sigma_z - i\sigma_x$ has the larger coefficient for $\theta > 0$, the Zeeman coupling preferably excites spins with momentum in the negative x-direction [cf. Fig 4.1 (b)], generating a current in the x-direction in agreement with Eq. (4.21). Analogously we can study the interplay between the orbital and Zeeman interaction. Here the dominant contribution is given by the spin lowering operator in the x-direction, $\sigma_y - i\sigma_z$. The interplay between the orbital and Zeeman coupling preferably excites electrons with momentum along the positive y-direction, generating a current in the negative y-direction. Thus our result for the perfect Dirac cone given by Eq. (4.21) can be understood by studying the interaction Hamiltonian.

4.4 CORRECTIONS TO THE PERFECT DIRAC CONE

So far we have shown that within the pure surface-state model a finite photocurrent response can be induced by including orbital as well as Zeeman coupling between light and electrons. Since we would like to compare our results to existing literature [Hosur, 2011], we now turn to a full analysis that includes perturbations to the perfect Dirac cone and an in-plane external magnetic field as studied by Hosur [2011].

We consider the model Hamiltonian

$$H = v(p_x\sigma_y - p_y\sigma_x) + \frac{\lambda}{2}(p_+^3 + p_-^3)\sigma_z - g\mu_B B\sigma_x, \tag{4.33}$$

where $v = v_F + \Lambda p^2$ with the Fermi velocity v_F, g denotes the g-factor, $p_\pm = p_x \pm ip_y = pe^{\pm i\phi}$, and $\sigma_\pm = \sigma_x \pm i\sigma_y$. λ is the cubic warping [Fu, 2009; Zhang et al., 2010a; Wang et al., 2011], Λ parametrizes a correction to the Fermi velocity [Fu, 2009; Basak et al., 2011], and B denotes the external magnetic field taken along the x-direction. For quantitative estimates, we use $\lambda = 50.1$ eV $\text{Å}^3/\hbar^3$ [Liu et al., 2010], and $\Lambda \sim 10$ eV $\text{Å}^3/\hbar^3$, where we assumed that $\Lambda p_F^3 \sim 1\%$ of half the band gap energy. This Hamiltonian is particle-hole symmetric, $H|\boldsymbol{p}, \pm\rangle = \pm E|\boldsymbol{p}, \pm\rangle$, with

$$E = \sqrt{p^2v^2 + p^6\lambda^2\cos^2(3\phi) + 2Bg\mu_B pv\sin(\phi) + B^2g^2\mu_B^2}. \tag{4.34}$$

As above, we consider circularly polarized light incident at an arbitrary angle given by Eq. (4.3). The interaction Hamiltonian is still given by Eq. (4.18) where H is now given by Eq. (4.33).

4.4.1 *Calculation of the photocurrent*

In order to calculate the photocurrent, we need to evaluate Eq. (4.10). Since we now included various corrections to the linear dispersion, one has to be careful when evaluating the current response and we will outline the calculation in the following. We will start with the integrand $v_{\boldsymbol{p},+}|\langle\boldsymbol{p}, +|H'_-|\boldsymbol{p}, -\rangle|^2$ before addressing the δ-function. We then proceed to the entire integral in Eq. (4.10).

Calculating the integrand in Eq. (4.10) is expedited by using projection operators $\hat{P}_{\pm}$ onto the two bands given by

$$\hat{P}_{\pm} = |\boldsymbol{p}, \pm\rangle\langle\boldsymbol{p}, \pm| = \frac{1}{2} \pm \frac{H}{2E}, \tag{4.35}$$

where E is the full energy with all corrections to the perfect Dirac spectrum given by Eq. (4.34). With these projection operators, the integrand in Eq. (4.10) becomes

$$-v_{p,+}|\langle\boldsymbol{p}, +|H'_-|\boldsymbol{p}, -\rangle|^2 = \langle\boldsymbol{p}, -|H'_+|\boldsymbol{p}, +\rangle\langle\boldsymbol{p}, +|H'_-|\boldsymbol{p}, -\rangle\langle\boldsymbol{p}, -|\frac{\partial H}{\partial \boldsymbol{p}}|\boldsymbol{p}, -\rangle$$

$$= \mathrm{tr}\left[\hat{P}_- H'_+ \hat{P}_+ H'_- \hat{P}_- \frac{\partial H}{\partial \boldsymbol{p}}\right]. \tag{4.36}$$

In the first step, we used that the transition $|\boldsymbol{p}, +\rangle \to |\boldsymbol{p}, -\rangle$ ($|\boldsymbol{p}, -\rangle \to |\boldsymbol{p}, +\rangle$) happens via emission (absorption) of a photon and is therefore mediated by the coupling involving A_+ (A_-). The minus sign is included by taking the expectation value with respect to the lower band, as $v_{p,+} = -v_{p,-}$. In the second step, we used that the expectation value of an operator can be written as

$$\langle\boldsymbol{p}, \pm|\hat{O}|\boldsymbol{p}, \pm\rangle = \mathrm{tr}[\hat{P}_{\pm}\hat{O}] = \mathrm{tr}\left[\left(\frac{1}{2} \pm \frac{H}{2E}\right)\hat{O}\right]. \tag{4.37}$$

In order to calculate Eq. (4.36) explicitly, we need to write out the interaction Hamiltonian given by Eq. (4.18). We would like to separate terms which create/annihilate a photon and write the interaction Hamiltonian in terms of $A_{\pm}$. For clarity, we will present the calculation for $\varphi = 0$. The calculation for arbitrary angle of incidence is relegated to App. B. The vector potential for left-circular polarization and $\hat{\boldsymbol{q}} = \sin\theta\,\hat{\boldsymbol{y}} - \cos\theta\,\hat{\boldsymbol{z}}$ is given by

$$\boldsymbol{A}(t) = A_0[\cos(\boldsymbol{q}\cdot\boldsymbol{r} - \omega t)\hat{\boldsymbol{x}} - \sin(\boldsymbol{q}\cdot\boldsymbol{r} - \omega t)(\hat{\boldsymbol{x}} \times \hat{\boldsymbol{q}})]$$

$$= \frac{A_-}{2}e^{i\boldsymbol{q}\cdot\boldsymbol{r}}(\hat{\boldsymbol{x}} + i\cos\theta\,\hat{\boldsymbol{y}} + i\sin\theta\,\hat{\boldsymbol{z}}) + c.c. \tag{4.38}$$

with $A_-^* = A_+$. We can read off that $A_x = \frac{1}{2}(A_+ + A_-)$ and $A_y = \frac{1}{2i}\cos\theta(A_+ - A_-)$. With these expressions and $\partial H/\partial p_x = v_x$ as well as $\partial H/\partial p_y = v_y$, the orbital part of the interaction Hamiltonian becomes

$$\frac{\partial H}{\partial p_x}A_x(t) + \frac{\partial H}{\partial p_y}A_y(t) = \frac{1}{2}\{A_+\left[v_x - i\cos\theta v_y\right] + A_-\left[v_x + i\cos\theta v_y\right]\}. \tag{4.39}$$

In order to calculate the Zeeman term, we note that

$$\nabla \times \boldsymbol{A} = \frac{1}{2}A_-\big[i\boldsymbol{q} \times (\hat{\boldsymbol{x}} + i\cos\theta\,\hat{\boldsymbol{y}} + i\sin\theta\,\hat{\boldsymbol{z}})\big]e^{i\boldsymbol{q}\cdot\boldsymbol{r}} + c.c.$$

$$= \frac{q}{2}A_-\big[-\hat{\boldsymbol{x}} - i\cos\theta\,\hat{\boldsymbol{y}} - i\sin\theta\,\hat{\boldsymbol{z}}\big]e^{i\boldsymbol{q}\cdot\boldsymbol{r}} + c.c.$$

$$= -q\boldsymbol{A}. \tag{4.40}$$

For right-circularly polarized light we would obtain the opposite sign in the last line of Eq. (4.40), i.e., $\nabla \times \boldsymbol{A}_{\mathrm{RCP}} = q\boldsymbol{A}_{\mathrm{RCP}}$. With Eq. (4.40) the Zeeman coupling becomes

$$(\nabla \times \boldsymbol{A}) \cdot \hat{\boldsymbol{\sigma}} = -\frac{q}{2}A_-(\sigma_x + i\cos\theta\sigma_y + i\sin\theta\sigma_z) + c.c. \tag{4.41}$$

Inserting Eqs. (4.39) and (4.41) into the interaction Hamiltonian given by Eq. (4.18), we find

$$H' = -\frac{e}{2}A_-\Big\{v_x + i\cos\theta v_y - v_Z(\sigma_x + i\cos\theta\sigma_y + i\sin\theta\sigma_z)\Big\} + c.c., \tag{4.42}$$

where $v_Z = \frac{g_s\hbar\omega}{2mc}$ is helicity dependent, i.e., changes sign under $\omega \to -\omega$. The integrand can now be explicitly written as

$$-v_{\boldsymbol{p},+}|\langle\boldsymbol{p},+|H'|\boldsymbol{p},-\rangle|^2 = \frac{e^2}{4}\mathrm{tr}\Big\{\hat{P}_-A_+\big[v_x - i\cos\theta v_y - v_Z\Sigma_-\big]$$

$$\hat{P}_+A_-\big[v_x + i\cos\theta v_y - v_Z\Sigma_+\big]\hat{P}_-v_x\Big\}\hat{\boldsymbol{x}}$$

$$+ \frac{e^2}{4}\mathrm{tr}\Big\{\hat{P}_-A_+\big[v_x - i\cos\theta v_y - v_Z\Sigma_-\big]$$

$$\hat{P}_+A_-\big[v_x + i\cos\theta v_y - v_Z\Sigma_+\big]\hat{P}_-v_y\Big\}\hat{\boldsymbol{y}} \tag{4.43}$$

where $\Sigma_\pm = \sigma_x \pm i\cos\theta\sigma_y \pm i\sin\theta\sigma_z$. Eq. (4.43) is exact and contains all perturbations to the perfect Dirac spectrum arising from the interaction matrix element and the velocity.

In addition to being careful with the definition of the velocity, we must also ensure that the argument of the δ-function in Eq. (4.10) contains the perturbations of the pure Dirac spectrum.[2] The energy E is angle dependent and we cannot easily perform the angular integration. We thus express the δ-function as

$$\delta(2E - \hbar\omega) = 4E\delta\left(4E^2 - \hbar^2\omega^2\right) = 4E\int_{-\infty}^{\infty}\frac{d\eta}{2\pi}e^{i\eta(4E^2 - \hbar^2\omega^2)}, \tag{4.44}$$

---

2 At this point, the calculation by Hosur [2011] was not carefully done, missing important contributions to the current and leading to an incorrect final result.

where we used that E and $\hbar\omega$ are defined as positive. We expand the δ-function to first order in λ and Λ and second order in B. The angular integration can now be evaluated in a straightforward manner and we find

$$j \simeq \frac{4\pi e\tau_p}{\hbar} \int d\eta \int \frac{dp\, p}{(2\pi\hbar)^2} \left[\Xi^{(0)}(p) + \eta \Xi^{(1)}(p) + \eta^2 \Xi^{(2)}(p) \right] e^{i\eta[4(pv_F)^2 - (\hbar\omega)^2]},$$

(4.45)

where $\Xi^{(i)}(p)$ are functions of momentum and λ, Λ, and B. The expressions for $\Xi^{(i)}(p)$ are long without providing much insight and will not be presented here. The integral over η is simplified by writing $\eta \rightarrow -i\frac{\partial}{\partial(\hbar\omega)^2}$ for the factors of η in the brackets, and then first carrying out the η-integral for each term separately. The remaining integrals can now be done since the angular dependence of the eigenstates has been eliminated. The integration over η in combination with the exponential factor can now be resubstituted by a δ-function. Using $\delta(4(pv_F)^2 - \xi) = \frac{1}{8v_F^2 p}\delta\left(p - \frac{\sqrt{\xi}}{2v_F}\right)$ with $\xi = (\hbar\omega)^2$, Eq. (4.45) becomes

$$j \simeq \frac{4e\pi\tau_p}{\hbar} \frac{1}{(2\pi\hbar)^2} \frac{1}{8v_F^2} \left\{ \Xi^{(0)}\left(\frac{\sqrt{\xi}}{2v_F}\right) + i\frac{\partial}{\partial\xi}\Xi^{(1)}\left(\frac{\sqrt{\xi}}{2v_F}\right) - \frac{\partial^2}{\partial\xi^2}\Xi^{(2)}\left(\frac{\sqrt{\xi}}{2v_F}\right) \right\},$$ (4.46)

which can be easily evaluated.

4.4.2 *Results*

Above we have only studied the perfectly linear Dirac dispersion without external fields. When we include perturbations to this simple model like the hexagonal warping λ, the correction to the Fermi velocity Λ, or an in-plane magnetic field B, we find additional helicity-dependent as well as helicity-independent contributions to the photocurrent, as listed in Tabs. 4.1 and 4.2. We introduce dimensionless constants $\bar{v}_Z$, $\bar{\lambda}$, $\bar{\Lambda}$, and $\bar{B}$ to estimate the relative magnitude of the various contributions (see caption of Tab. 4.1). For $B = 0$, there is only a single additional contribution to the response given by $j_{\text{hd},x'}^{(\Lambda)}$. This current results from pure Zeeman coupling, is helicity-dependent, and flows in the x'-direction perpendicular to the plane of incidence of the light. For Λ estimated as 1% of half the band gap energy, we find $\bar{\Lambda} \sim 10^{-3}$. Thus, $j_{\text{hd},x'}^{(\Lambda)}/j_{x'}^{(0)} \sim \bar{\Lambda} \sim 10^{-3}$, and the leading contribution in x'-direction, i.e., perpendicular to the plane of incidence, is helicity-dependent. The overall leading response, however, is still $j_{y'}^{(0)}$, i.e., is helicity-independent and flows parallel to the plane of incidence.

$j_{hd}^{(X)}$	prefactor	x'	y'
0	$C\bar{v}_Z^2 \sin\theta$	1	—
λ	—	—	—
Λ	$-\frac{C}{4}\bar{v}_Z^2 \bar{\Lambda}\sin\theta$	1	—
B_1	$\frac{9C}{8}\bar{v}_Z\bar{\lambda}\bar{B}\sin(2\theta)$	$\cos(2\varphi)$	$\sin(2\varphi)$
B_2	$3C\bar{v}_Z^2\bar{\lambda}\bar{B}^2\cos\theta$	$\cos\varphi$	$\sin\varphi$
ΛB_1	$C\bar{v}_Z\bar{B}\bar{\Lambda}$	$\cos\varphi$	$\cos^2\theta\sin\varphi$
ΛB_2	$\frac{15C}{2}\bar{\lambda}\bar{B}^2\bar{\Lambda}\cos\theta$	$\cos\varphi$	$\sin\varphi$
ΛB_3	$-\frac{27C}{16}\bar{v}_Z\bar{\lambda}\bar{B}\bar{\Lambda}\sin(2\theta)$	$\cos(2\varphi)$	$\sin(2\varphi)$
ΛB_4	$-C\bar{v}_Z^2\bar{B}^2\bar{\Lambda}\sin\theta$	$2+\cos(2\varphi)$	$\sin(2\varphi)$
ΛB_5	$-\frac{27C}{4}\bar{v}_Z^2\bar{\lambda}\bar{B}^2\bar{\Lambda}\cos\theta$	$\cos\varphi$	$\sin\varphi$

Table 4.1: Helicity-dependent corrections to the current induced by various perturbations. $\bar{v}_Z = v_Z/v_F \sim 10^{-5}$, $\bar{\lambda} = \lambda(\hbar\omega)^2/(v_F^3) \sim 10^{-2}$, $\bar{\Lambda} = \Lambda(\hbar\omega)^2/(v_F^3) \sim 10^{-3}$, and $\bar{B} = g\mu_B B/(\hbar\omega) \sim 10^{-4}B/$T are dimensionless parameters and C is given in the text below Eq. (4.21).

$j_{hi}^{(X)}$	prefactor	x'	y'
0	$-C\bar{v}_Z \sin\theta$	—	1
λ	—	—	—
Λ	—	—	—
B_1	$3C\bar{v}_Z\bar{\lambda}\bar{B}^2\cos\theta$	$\sin\varphi$	$-\cos\varphi$
B_2	$\frac{3C}{8}\bar{v}_Z^2\bar{\lambda}\bar{B}\sin(2\theta)$	$-\sin(2\varphi)$	$\cos(2\varphi)$
ΛB_1	$\frac{C}{4}\bar{B}\bar{\Lambda}$	$-(3+\cos^2\theta)\sin\varphi$	$(1+3\cos^2\theta)\cos\varphi$
ΛB_2	$\frac{C}{4}\bar{v}_Z^2\bar{B}\bar{\Lambda}\sin^2\theta$	$\sin\varphi$	$\cos\varphi$
ΛB_3	$\frac{33C}{4}\bar{v}_Z\bar{\lambda}\bar{B}^2\bar{\Lambda}\cos\theta$	$-\sin\varphi$	$\cos\varphi$
ΛB_4	$\frac{17C}{32}\bar{v}_Z^2\bar{\lambda}\bar{B}\bar{\Lambda}\sin(2\theta)$	$\sin(2\varphi)$	$-\cos(2\varphi)$

Table 4.2: Helicity-independent corrections to the current induced by various perturbations. Parameters as in Tab. 4.1. C is given in the text below Eq. (4.21).
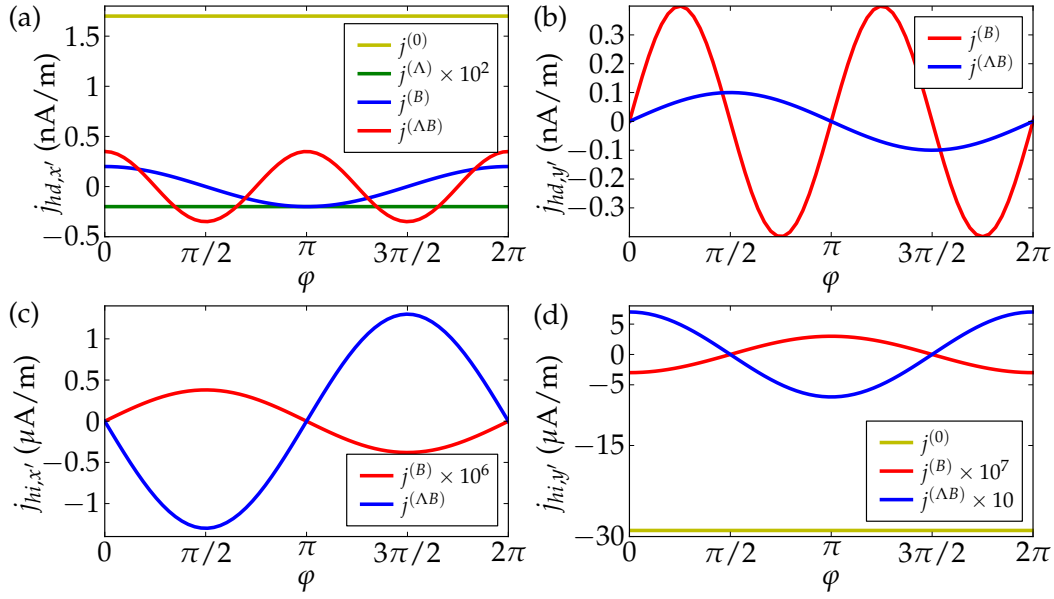
Figure 4.2: Current as a function of azimuthal angle of incidence φ of the vector potential. hd (hi): helicity dependent (independent). We choose $\theta = 0.98$ and the other parameters are as given in the text. When a magnetic field is applied the photocurrent response acquires strong angle dependences.

When we include an external magnetic field, we break the rotational symmetry of the problem and other helicity-independent and dependent contributions to the photocurrent emerge. An important results is, that symmetry no longer requires that helicity-independent and -dependent currents have to flow parallel and perpendicular to the plane of incidence, respectively. For a magnetic field of strength $B = 1$ T, the leading helicity-dependent contribution is $j_{\text{hd}}^{(B_1)}$ and in general has components in the x'- and y'-direction. This contribution arises from interference of orbital and Zeeman coupling and has a relative magnitude of $j_{\text{hd}}^{(B_1)}/j_{x'}^{(0)} \sim \bar{\lambda}\bar{B}/\bar{v}_Z \sim 10^{-1}$. The leading helicity-independent contribution is $j_{\text{hi}}^{(\Lambda B_1)}$ and also has components parallel and perpendicular to the plane of incidence. This current is induced by pure orbital coupling, i.e., it remains finite when Zeeman coupling is neglected. If the plane of incidence does not coincide with the yz-plane [cf. Fig. 4.1], the current $j_{\text{hi}}^{(\Lambda B_1)}$ has finite components along the x'- and the y'-direction with relative magnitude $j_{\text{hi}}^{(\Lambda B_1)}/j_{y'}^{(0)} \sim \bar{B}\bar{\Lambda}/\bar{v}_Z \sim 10^{-2}$ and $j_{\text{hi},x'}^{(\Lambda B_1)}/j_{\text{hd},x'}^{(0)} \sim \bar{B}\bar{\Lambda}/\bar{v}_Z^2 \sim 10^3$. In this case, the overall dominant response both parallel and perpendicular to the plane of incidence is helicity-independent. $/j_{x'}^{(0)}$ remains the leading helicity-dependent contribution.

For normal incidence, i.e., $\theta = \varphi = 0$, many contributions vanish and in the absence of an external magnetic field, there is no photocurrent response. Even including B, the helicity-dependent photocurrent is greatly reduced with respect to the case of oblique incidence since $j_{x'}^{(0)}$ vanishes for $\theta = 0$. The leading helicity-dependent contributions are $j_{\mathrm{hd},x}^{(\Lambda B_1)}$ and $j_{\mathrm{hd},x}^{(\Lambda B_2)}$ which flow parallel to the magnetic field with relative magnitude $j_{\mathrm{hd},x}^{(\Lambda B_1)}/j_{x'}^{(0)} \sim \bar{B}\bar{\Lambda}/\bar{v}_Z \sim 10^{-2}$ and $j_{\mathrm{hd},x}^{(\Lambda B_2)}/j_{x'}^{(0)} \sim \bar{\lambda}\bar{B}^2\bar{\Lambda}/\bar{v}_Z^2 \sim 10^{-3}$. $j_{\mathrm{hd},x}^{(\Lambda B_2)}$ is the only helicity-dependent current induced by pure orbital coupling. This result differs from the photocurrent obtained by Hosur [2011] in the additional factor of Λ. As before, the leading helicity-independent current is $j_{\mathrm{hi}}^{(\Lambda B_1)}$ which flows perpendicular to the magnetic field. Thus, for normal incidence including a magnetic field, the leading response parallel to the magnetic field is helicity-dependent while the leading response perpendicular to the magnetic field is helicity-independent.

The various contributions to the current as listed in Tabs. 4.1 and 4.2 depend strongly on the angle of incidence of the laser. Changing the azimuthal angle φ of the vector potential has significant effect on what is the leading contribution in a given direction. Fig. 4.2 shows the dependence of the different contributions on φ for $\theta = 0.98$. The current $j^{(0)}$ in independent of the azimuthal angle of incidence but the corrections that depend on the magnetic field B have a strong angular dependence. The dominant contribution parallel to the plane of incidence, i.e, in the y'-direction, is $j_{y'}^{(0)}$ and is not affected by changes in φ. As mentioned above, the dominant contribution perpendicular to the plane of incidence, however, i.e., in the x'-direction, changes significantly with the azimuthal angle. For light incident in the yz-plane, i.e, for $\varphi = 0$ or $\varphi = \pi$, the leading current is helicity-dependent and given by $j_{x'}^{(0)}$. For other values of φ the large helicity-independent current $j_{\mathrm{hi},x'}^{(\Lambda B_1)}$ is the dominant contribution along x'.

4.5 ARBITRARY POLARIZATION

In this section we generalize our results and consider arbitrarily polarized light incident onto the sample as illustrated in Fig. 4.1 (c),

$$\boldsymbol{A}(t) = \frac{A_0}{2} e^{-i\omega t + i\boldsymbol{q}\boldsymbol{r}} \begin{pmatrix} \sin 2\alpha \cos\varphi + (i + \cos 2\alpha) \cos\theta \sin\varphi \\ -\sin 2\alpha \sin\varphi + (i + \cos 2\alpha) \cos\theta \cos\varphi \\ (i + \cos 2\alpha) \sin\theta \end{pmatrix} + c.c, \quad (4.47)$$

with polar angle $\theta \, \epsilon \, [0, \pi/2]$ and the azimuthal angle φ defined from the negative y-axis, such that light is incident in the yz-plane for $\varphi = 0$, i.e., a mirror plane of the sample. α varies the polarization state with period π [cf. App. A] (P-polarized: $\alpha = 0$; left-circular: $\alpha = \pi/4$; P-polarized: $\alpha = \pi/2$; right-circular: $\alpha = 3\pi/4$).

As we are interested in comparing the calculated photoresponse to the experimental findings of McIver et al. [2012], we need to analyze the general polarization dependence of the current. The calculation presented above can be performed in an analogous way for arbitrary light polarization and the photocurrent for the ideal Dirac spectrum takes the form

$$ \boldsymbol{j}^{(0)} = - C\bar{v}_Z \left[\frac{1}{2} \left(1 - \cos 4\alpha \right) \sin\theta \, \hat{\boldsymbol{y}}' + \left(\frac{1}{4} \sin 4\alpha \sin 2\theta - \bar{v}_Z \sin 2\alpha \sin\theta \right) \hat{\boldsymbol{x}}' \right]. $$

$$ (4.48) $$

For $\alpha = \pi/4$ we recover the original result of Eq. (4.21) and see that current in the y'-direction is helicity-independent whereas the current in the x'-direction is helicity-dependent. For P-polarized light the current completely vanishes. In addition to the helicity-independent contribution along the y'-direction and the helicity-dependent contribution along x', we find another helicity-independent contribution to the current which flows perpendicular to the plane of incidence of the light. This contribution is $\sim \sin 4\alpha$ and is only nonzero for elliptically polarized light. It results from interference of orbital and Zeeman coupling and is thus of the same order of magnitude as the helicity-independent contribution $j_{y'}^{(0)} \sim 10 \ \mu\text{A}/\text{m}$. Note that this helicity-independent contribution perpendicular to the plane of incidence does not violate the symmetry of the system as discussed above since it vanishes for circularly polarization.

Using Eq. (4.47) we can calculate the total photocurrent response to P-polarized light including the corrections to the ideal Dirac spectrum. For $\alpha = 0$ the light is P-linearly polarized in the direction $\hat{\boldsymbol{x}} \times \hat{\boldsymbol{q}}$ parallel to the plane of incidence. The resulting contributions to the current are listed in in Tab. 4.3. The vector potential for S-polarized light for $\hat{\boldsymbol{q}} = \sin\theta \, \hat{\boldsymbol{y}} - \cos\theta \, \hat{\boldsymbol{z}}$ and $\varphi = 0$, is given by

$$ \boldsymbol{A}_S(t) = A_0 \cos(\boldsymbol{q}\boldsymbol{r} - \omega t) \, \hat{\boldsymbol{x}}. $$

$$ (4.49) $$

and the resulting currents are listed in Tab. 4.4. The currents from S- and P-linearly polarized light are, of course, helicity independent. As mentioned above, the overall largest contribution to the photocurrent, which is helicity independent and in the direction opposite to the direction of propagation of the incident

$j_P^{(X)}$	prefactor	x'	y'
0	—	—	—
λ	$\frac{3C}{4}\bar{v}_Z\bar{\lambda}\cos\theta$	$-\sin(3\varphi)$	$\cos(3\varphi)$
Λ	$\frac{5C}{8}\bar{v}_Z\bar{\lambda}\bar{\Lambda}\cos\theta$	$\sin(3\varphi)$	$-\cos(3\varphi)$
B	$6C\bar{v}_Z\bar{\lambda}\bar{B}^2\cos\theta$	$\sin\varphi$	—
ΛB_1	$\frac{C}{2}\bar{B}\bar{\Lambda}$	$-\cos^2\theta\sin\varphi$	$3\cos^2\theta\cos\varphi$
ΛB_2	$\frac{C}{2}\bar{v}_Z^2\bar{B}\bar{\Lambda}$	$\sin\varphi$	$\cos\varphi$
ΛB_3	$\frac{3C}{2}\bar{v}_Z\bar{\lambda}\bar{B}^2\bar{\Lambda}\cos\theta$	$-9\sin\varphi + 5\sin(3\varphi)$	$\cos\varphi[7-10\cos(2\varphi)]$

Table 4.3: Photocurrent response for P-polarized light. As before, $\bar{v}_Z = v_Z/v_F \sim 10^{-5}$, $\bar{\lambda} = \lambda(\hbar\omega)^2/(v_F^3) \sim 10^{-2}$, $\bar{\Lambda} = \Lambda(\hbar\omega)^2/(v_F^3) \sim 10^{-3}$, and $\bar{B} = g\mu_B B/(\hbar\omega) \sim 10^{-4}B/\text{T}$ are dimensionless parameters and C is given in the main text.

light, can be induced by S-polarized light. Note that without an external magnetic field, also for linearly S- or P-polarized light a net photoresponse is only induced when Zeeman coupling is included. Without the Zeeman coupling, the leading response is linear in the external magnetic field B and the correction to the Fermi velocity Λ for both S- and P-polarization.

For linearly polarized light and arbitrary angle of incidence we obtain helicity-independent currents that are perpendicular to the plane of incidence even without an external magnetic field, i.e., $j_{S,P,x'}^{(\lambda,\Lambda)}$. This does not violate the symmetry of our problem since these contributions vanish when the plane of incidence coincides with one of the symmetry axes of the crystal, located at $\varphi = n\pi/3$ for integer n [cf. Fig. 2.1 (b)]. Indeed, since these are the leading order contributions perpendicular the plane of incidence for linearly polarized light, the angle dependence of the current reflects the crystal symmetry and could be used as a probe of the underlying crystal structure.

4.6 PARTICLE-HOLE ASYMMETRY

For completeness we still need to discuss the effect of particle-hole asymmetry on the photocurrent response. One can show that in the present model particle-hole asymmetry will have no effect on the current. In general, i.e., for electrons

$j_S^{(X)}$	prefactor	x'	y'
0	$-C\bar{v}_Z\sin\theta$	—	1
λ	$\frac{3C}{8}\bar{v}_Z\bar{\lambda}\cos\theta$	$\sin(3\varphi)$	$-\cos(3\varphi)$
Λ	$\frac{5C}{16}\bar{v}_Z\bar{\lambda}\bar{\Lambda}\cos\theta$	$-\sin(3\varphi)$	$\cos(3\varphi)$
B_1	$3C\bar{v}_Z\bar{\lambda}\bar{B}^2\cos\theta$	—	$-\cos\varphi$
B_2	$\frac{3C}{8}\bar{v}_Z^2\bar{\lambda}\bar{B}\sin(2\theta)$	$-\sin(2\varphi)$	$\cos(2\varphi)$
ΛB_1	$\frac{C}{4}\bar{B}\bar{\Lambda}$	$-3\sin\varphi$	$\cos\varphi$
ΛB_2	$-\frac{C}{4}\bar{v}_Z^2\bar{B}\bar{\Lambda}\cos^2\theta$	$\sin\varphi$	$\cos\varphi$
ΛB_3	$\frac{3C}{4}\bar{v}_Z\bar{\lambda}\bar{B}^2\bar{\Lambda}\cos\theta$	$-[2\sin\varphi + 5\sin(3\varphi)]$	$9\cos\varphi + 5\cos(3\varphi)$
ΛB_4	$\frac{17C}{32}\bar{v}_Z^2\bar{\lambda}\bar{B}\bar{\Lambda}\sin(2\theta)$	$\sin(2\varphi)$	$-\cos(2\varphi)$

Table 4.4: Photocurrent response for S-polarized light. Parameters as in Tab. 4.3.

and holes moving with different velocities, the expression for the photocurrent given by Eq. (4.10) becomes

$$j_{\text{PHA}} = \frac{2\pi\tau_p}{\hbar}\sum_{\boldsymbol{p}}\left(-ev_{\boldsymbol{p}}^{(e)} + ev_{\boldsymbol{p}}^{(h)}\right)|\langle\boldsymbol{p},+|H'_-|\boldsymbol{p},-\rangle|^2\delta(E_+ - E_- - \hbar\omega)$$

$$= -\frac{2\pi e\tau_p}{\hbar}\sum_{\boldsymbol{p}}\left(\frac{\partial E_+}{\partial\boldsymbol{p}} - \frac{\partial E_-}{\partial\boldsymbol{p}}\right)|\langle\boldsymbol{p},+|H'_-|\boldsymbol{p},-\rangle|^2\delta(E_+ - E_- - \hbar\omega), \quad (4.50)$$

where now the energy is given by

$$E_\pm = \frac{p^2}{2m} \pm \sqrt{p^2v^2 + p^6\lambda^2\cos^2(3\phi) + 2Bg\mu_B pv\sin(\phi) + B^2g^2\mu_B^2}, \qquad (4.51)$$

with $v = v_F + \Lambda p^2$ as before. One can see that Eq. (4.50) is independent of the particle-hole asymmetry. In the first parenthesis, the corrections to the velocities for electrons and holes cancel each other because the particle-hole asymmetric term enters both energies with the same sign. The same argument applies to the δ-function. For the transition rate one can see that only the orbital interaction depends on the particle-hole asymmetric term [cf. Eq. (4.18)]. Thus we can neglect the Zeeman coupling. The term in the orbital interaction Hamiltonian that results from the particle-hole asymmetry is proportional to the identity matrix. For vertical transitions, however, the initial and final states $|\boldsymbol{p},\pm\rangle$ are orthogonal. The interaction matrix element thus vanishes for the particle-hole asymmetric contribution and the current response is not affected by particle-hole asymmetry.

Motivated by experiments [McIver et al., 2012; Duan et al., 2014], we studied the photocurrent response in topological insulators. We focused on the photocurrent response of the topological surface states and find that pure orbital coupling between light and electrons does not induce a photocurrent in the absence of an external magnetic field. The leading response for obliquely incident circularly polarized light is induced by an interplay between orbital and Zeeman coupling. This contribution is helicity-independent and in the plane of incidence. We find that the helicity-dependent photocurrents are quadratic in the Zeeman coupling and thus very small. Pure orbital coupling can only induce a net photogalvanic charge current when both band curvature and in-plane external magnetic field are included.

When studying the polarization dependence of the photocurrent response we also find a helicity-independent contribution which flows perpendicular to the plane of incidence of the light. Thus the contributions of the photocurrent that flow perpendicular to the direction of propagation of the light, i.e., the contributions proportional to $\sin 2\alpha$ and $\sin 4\alpha$, qualitatively agree with the two contributions identified in the experiment to have surface origin, i.e., C and L_1. Since Zeeman coupling is required, the resulting currents are, however, very small and especially the helicity-dependent contribution is several orders of magnitude smaller than the experimentally observed currents.

Our results suggest that in order to understand the experimental findings one has to extend the theory to include the bulk bands, the photon drag effect, or thermoelectric effects originating from inhomogeneous laser excitation. As a photon energy of 1.5 eV was used in the experiment [McIver et al., 2012], which exceeds the bulk band gap, it is natural to extend the model to include the bulk states. As discussed in Chap. 2, photocurrents from the CPGE or LPGE cannot originate from the inversion symmetric bulk. Transitions between spin-degenerate bulk states can thus only contribute through higher order effects to the measured photocurrent. The same is not true, however, for transitions between the helical surface states and the spin-degenerate bulk states, e.g., when electrons from the Dirac cone are excited into the bulk conduction band. In the following chapter, we therefore extend the surface model discussed above to include bulk states and calculate the photocurrent response when one considers transitions between surface and bulk states.

BULK CONTRIBUTIONS TO THE PHOTOCURRENT IN TOPOLOGICAL INSULATORS[1]

In the previous chapter we analyzed the photocurrent response of TIs within a pure surface state model and found only a remarkably small photocurrent response. In this chapter we will extend the analysis to include the low-energy bulk states. This is especially relevant when photocurrents are induced using photon energies that exceed the bulk band gap, as in the experiment discussed in Chap. 3 [McIver et al., 2012]. Photon absorption can then, depending on the Fermi level, lead to transitions from the bulk valence band (BVB) to the bulk conduction band (BCB), from the bulk valence band (BVB) into the surface Dirac cone, or from the surface Dirac cone into the BCB as illustrated in Fig. 5.1. While the spin degeneracy and crystal inversion symmetry of the bulk prevent a photocurrent response due to the CPGE or LPGE [cf. Sec. 2.2], this is not the case for transitions between the spin-split surface states and bulk states near the surface where inversion symmetry is broken. Thus a full analysis of the photoresponse of TIs has to take into account the photoexcitation between surface and bulk states.

We include the low energy bulk states within a minimal four band model [Zhang et al., 2009a; Liu et al., 2010] and find that indeed transitions between surface and bulk states, e.g., transitions from the surface Dirac cone into the bulk conduction band, can lead to a finite photocurrent. We find that circularly polarized light leads to transitions between surface and bulk states that occur asymmetrically in momentum space, inducing a net current. In the pure surface state model the absorption of circularly polarized photons led to spin-flip transitions within the Dirac cone. Here, we find that the transitions between surface and bulk states that generate a net photocurrent are spin-conserving, i.e., they occur between

---

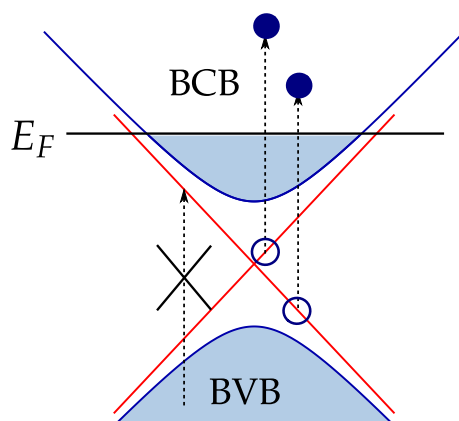[1] This chapter is based on joint work with Gil Refael and Felix von Oppen.

Figure 5.1: Depending on the Fermi energy various transitions have to be taken into account. For a Fermi level inside the bulk conduction band (BCB), e.g., only excitations from the surface states into the unoccupied bulk states are allowed. Transitions from the bulk valence band (BVB) into the surface states are blocked by Pauli's principle. Transitions from the BVB into the BCB might also be allowed for sufficiently energetic light. Due to the inversion symmetry and spin degeneracy of the bulk these transitions will, however, only contribute through higher order effects, e.g., the photon drag effect, not considered here.

states with the same spin orientation. The fact that we are considering transitions into bulk states also implies that the photocurrent is not completely spin polarized. In the pure surface state model excited carriers moving in the same direction must have the same spin and the resulting photocurrent was necessarily spin polarized. The bulk states, however, are spin degenerate hosting co-moving electrons with opposite spin orientations.

5.1   MODEL

We generalize the model of the previous section to include photoinduced transitions between surface and bulk states. In order to do so we consider the full 3D bulk model Hamiltonian given by Eq. (2.5). For simplicity, we restrict ourselves to the essential parts and neglect particle-hole asymmetry, terms quadratic in the in-plane momentum $k_{\parallel}$, and cubic terms in the momentum k_z perpendicular to the surface. We will consider the 3D TI to be in the half space $z > 0$. An obvious way to model the surface of the 3D TI would be to study the interface between the TI and the vacuum at $z > 0$. This model, however, requires most of
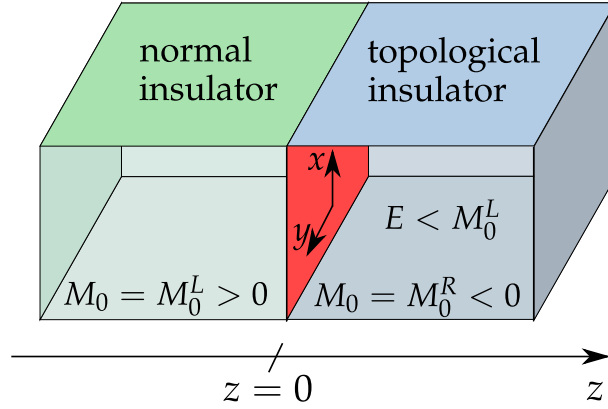
Figure 5.2: Schematic illustration of the finite step boundary condition for modeling the surface. For $z < 0$ we have a normal insulator with $M_0 = M_0^L > 0$ and for $z > 0$ we have a TI with $M_0 = M_0^R < 0$. The surface at $z = 0$ indicated in red then exhibits gapless surface states. We consider the regime $E < M_0^L$, i.e., electrons are not photoemitted from the TI.

the parameters in the Hamiltonian given by Eq. (2.5) to jump at $z = 0$. This leads to awkward boundary conditions for the wavefunction which make the analysis analytically involved.

An alternative approach to model the surface, is to study the interface between a TI and a trivial insulator, which is adiabatically connected to the vacuum. As we have seen in Chap. 2, the band inversion condition for the 3D TI Bi$_2$Se$_3$ is given by $M_0 < 0$. For the interface between a TI and a normal insulator it is thus sufficient to consider a jump in the mass M_0, from the normal insulator with $M_0 > 0$ at $z < 0$ to the TI with $M_0 < 0$ at $z > 0$.

The resulting Hamiltonian is given by [Zhang et al., 2009a; Liu et al., 2010]

$$H = (M_0(z) + M_1 k_z^2)\mathbf{1} \otimes \tau_z + B_0 k_z \mathbf{1} \otimes \tau_y + A_0(\sigma_x k_y - \sigma_y k_x) \otimes \tau_x, \qquad (5.1)$$

with a position-dependent mass

$$M_0(z) = \begin{cases} M_0^L > 0, & z \leq 0 \\ M_0^R < 0, & z > 0. \end{cases} \qquad (5.2)$$

For $M_1, B_0 > 0$ [Liu et al., 2010] this describes a topological insulator in the half space $z > 0$ and a trivial insulator in the half space $z < 0$, as illustrated in Fig. 5.2.

First, we need to determine the surface and bulk wavefunctions for this surface model which we will do in the following sections. In Chap. 2 we showed that the general form of the solution of

$$H(k_z \rightarrow -i\partial_z)\psi = E\psi \tag{5.3}$$

is given by

$$\psi_{\uparrow\downarrow}(z, \lambda) \sim \begin{pmatrix} \pm i e^{-i\phi} \\ 1 \end{pmatrix} \otimes \chi_{\uparrow\downarrow}(\lambda) e^{\lambda z}, \tag{5.4}$$

with

$$\chi_{\uparrow\downarrow}(\lambda) = \begin{pmatrix} \frac{\pm A_0 k_\parallel - B_0 \lambda}{E - M_0 + \lambda^2 M_1} \\ 1 \end{pmatrix}, \tag{5.5}$$

where the upper sign corresponds to $\psi_\uparrow, \chi_\uparrow$ and the lower sign to $\psi_\downarrow, \chi_\downarrow$. The first vector in the tensor product of Eq. (5.4) describes the spin degree of freedom. Spin is locked perpendicular to momentum and rotates around the Dirac cone. Spins of $\psi_{\uparrow\downarrow}$ are orthogonal to each other. λ can take the four possible values

$$\lambda_\pm^2 = \frac{2M_0 M_1 + B_0^2}{2M_1^2} \pm \sqrt{\frac{4B_0^2 M_0 M_1 + B_0^4}{4M_1^4} + \frac{E^2 - A_0^2 k_\parallel^2}{M_1^2}}. \tag{5.6}$$

In the most general form, the wavefunction can then be written as a superposition of the four possible contributions,

$$\Psi_{\uparrow\downarrow}(z) = \sum_{\alpha, \beta = \pm} \gamma_{\alpha,\beta} \psi_{\uparrow\downarrow}(z, \alpha\lambda_\beta), \tag{5.7}$$

where the coefficients $\gamma_{\alpha,\beta}$ are determined by boundary conditions and normalization. The wavefunctions have to obey the boundary conditions

$$\Psi^L(z = 0) = \Psi^R(z = 0) \tag{5.8}$$

$$\frac{d\Psi^L}{dz}\bigg|_{z=0} = \frac{d\Psi^R}{dz}\bigg|_{z=0}, \tag{5.9}$$

where $\Psi^{L/R}$ describes the wavefunction for $z < 0$ and $z > 0$, respectively. The wavefunctions also have to obey the orthonormality relations

$$\int_{-\infty}^{\infty} dz \, |\Psi_S(z)|^2 = 1 \tag{5.10}$$

for the surface states and

$$\int_{-\infty}^{\infty} dz \Psi_B^\dagger(k_z, z)\Psi_B(k_z', z) = \delta(k_z - k_z') \tag{5.11}$$

for the bulk states.

5.1.1 *Surface states*

For the surface states, $\lambda_\pm$ are complex with a finite real part. To ensure normalizability the wavefunction has to vanish at $\pm\infty$, i.e., $\Psi^L_S(z \to -\infty) = 0$ and $\Psi^R_S(z \to \infty) = 0$. The surface-state wavefunctions thus become

$$\Psi^L_{S,\uparrow\downarrow} = \begin{pmatrix} \pm ie^{-i\phi} \\ 1 \end{pmatrix} \otimes \Xi^L_{S,\uparrow\downarrow} \tag{5.12}$$

with

$$\Xi^L_{S,\uparrow\downarrow} = \frac{1}{\sqrt{N_S}} \left[a^L_S \, \chi^L_{S,\uparrow\downarrow}(\lambda^L_{S,+}) e^{\lambda^L_{S,+}z} + b^L_S \, \chi^L_{S,\uparrow\downarrow}(\lambda^L_{S,-}) e^{\lambda^L_{S,-}z} \right] \tag{5.13}$$

in the trivial insulator and

$$\Psi^R_{S,\uparrow\downarrow} = \begin{pmatrix} \pm ie^{-i\phi} \\ 1 \end{pmatrix} \otimes \Xi^R_{S,\uparrow\downarrow}, \tag{5.14}$$

with

$$\Xi^R_{S,\uparrow\downarrow} = \frac{1}{\sqrt{N_S}} \left[a^R_S \, \chi^R_{S,\uparrow\downarrow}(-\lambda^R_{S,+}) e^{-\lambda^R_{S,+}z} + b^R_S \, \chi^R_{S,\uparrow\downarrow}(-\lambda^R_{S,-}) e^{-\lambda^R_{S,-}z} \right], \tag{5.15}$$

in the TI. Here, $Re[\lambda^{L/R}_{S,\pm}] > 0$, N_S is a normalization constant, $a^{L/R}_S, b^{L/R}_S$ are complex coefficients, and

$$\chi^{L/R}_{S,\uparrow\downarrow}(\lambda) = \begin{pmatrix} \frac{\pm A_0 k_\parallel - B_0 \lambda}{E_S - M^{L/R}_0 + \lambda^2 M_1} \\ 1 \end{pmatrix}. \tag{5.16}$$

Inserting Eqs. (5.12)-(5.16) into the boundary conditions given by Eqs. (5.8) and (5.9), we find that these can only be fulfilled for

$$E_S = \pm A_0 k, \tag{5.17}$$

where the upper sign corresponds to state $\Psi_{S,\uparrow}$ and the lower sign to state $\Psi_{S,\downarrow}$. The boundary conditions Eqs. (5.8) and (5.9) together with the normalizability thus give the expected linear surface-state dispersion with $\Psi_{S,\uparrow}$ and $\Psi_{S,\downarrow}$ representing the positive- and negative-energy surface states, respectively. The expressions for the coefficients do not give any further insight and can be found in App. C.1.

As seen in Chap. 2, for $E_S = \pm A_0 k$ the surface state in the TI simplifies to

$$\Xi_S^R = \Xi_{S,\uparrow\downarrow}^R = \frac{1}{\sqrt{N_S}} \begin{pmatrix} 1 \\ 1 \end{pmatrix} \left[a_S^R e^{-\lambda_{S,+}^R z} + b_S^R e^{-\lambda_{S,-}^R z} \right] \tag{5.18}$$

with

$$\lambda_{S,\pm}^R = \frac{B_0}{2M_1} \pm \sqrt{\frac{B_0^2 + 4M_0^R M_1}{4M_1^2}}. \tag{5.19}$$

The wavefunction in the trivial insulator cannot be simplified further and is still given by Eqs. (5.12) and (5.13). The normalization constant N_S can be determined by using Eq. (5.10) and is given by

$$
N_S = 2 \left\{ \frac{\left| a_S^L \eta_{S,\uparrow\downarrow}^L(\lambda_{S,+}^L) \right|^2}{2Re[\lambda_{S,+}^L]} + \frac{\left| b_S^L \eta_{S,\uparrow\downarrow}^L(\lambda_{S,-}^L) \right|^2}{2Re[\lambda_{S,-}^L]} + \frac{\left| a_S^R \right|^2}{2Re[\lambda_{S,+}^R]} + \frac{\left| b_S^R \right|^2}{2Re[\lambda_{S,-}^R]} \right.
$$
$$
\left. + 2Re \left[\frac{\left(a_S^L \eta_{S,\uparrow\downarrow}^L(\lambda_{S,+}^L) \right)^* b_S^L \eta_{S,\uparrow\downarrow}^L(\lambda_{S,-}^L)}{\left(\lambda_{S,+}^L \right)^* + \lambda_{S,-}^L} \right] + 2Re \left[\frac{\left(a_S^R \right)^* b_S^R}{\left(\lambda_{S,+}^R \right)^* + \lambda_{S,-}^R} \right] \right\} \tag{5.20}
$$

This result can be approximated when considering the following. In the limit $M_0^L \to \infty$ we recover open boundary conditions which require $\Psi(z = 0) = 0$, and the wavefunction is localized near the surface completely inside the TI. For finite $M_0^L > E$ the wavefunction decays exponentially into the trivial insulator with a decay length of $\sim \sqrt{M_1/M_0^L}$. Thus also for finite M_0^L the wavefunction is localized mainly inside the TI and we can write

$$N_S = \frac{\left| a_S^R \right|^2}{Re[\lambda_{S,+}^R]} + \frac{\left| b_S^R \right|^2}{Re[\lambda_{S,-}^R]} + 4Re \left[\frac{\left(a_S^R \right)^* b_S^R}{\left(\lambda_{S,+}^R \right)^* + \lambda_{S,-}^R} \right] + \mathcal{O}\left(\frac{B_0^2}{M_0^L M_1} \right). \tag{5.21}$$

5.1.2 *Bulk states*

For high energies $E > M_0^R$, i.e., for the bulk states, $\lambda_\pm$ given by Eq. (5.6) can have complex solutions as well as purely real or purely imaginary solutions, depending on the system parameters and the energy. Since we are not interested in photoemission, we study the limit of $M_0^L > E$, i.e., the energy lies within the

bulk gap of the normal insulator. Normalizability requires $\Psi_B^L(z \to -\infty) = 0$ and the wavefunction decays exponentially inside the trivial insulator. Two solutions for λ^L have a positive real part and two solutions have a negative real part, such that the bulk wavefunction in the trivial insulator takes the form

$$\Psi_{B,\uparrow\downarrow}^L = \begin{pmatrix} \pm i e^{-i\phi} \\ 1 \end{pmatrix} \otimes \Xi_{B,\uparrow\downarrow}^L \tag{5.22}$$

with

$$\Xi_{B,\uparrow\downarrow}^L = \frac{1}{\sqrt{N_B}} \left[a_B^L \, \chi_{B,\uparrow\downarrow}^L(\lambda_{B,+}^L) e^{\lambda_{B,+}^L z} + b_B^L \, \chi_{B,\uparrow\downarrow}^L(\lambda_{B,-}^L) e^{\lambda_{B,-}^L z} \right] \tag{5.23}$$

where $Re[\lambda_{B,\pm}^L] > 0$, N_B is the normalization constant, and a_B^L, b_B^L are complex coefficients.

In the topological insulator at $z > 0$, the wavefunction has two propagating solutions for $E > M_0^R$ corresponding to $\lambda_{B,-}^R = \pm i k_z$. The other two solutions are in general complex with finite, positive and negative real part, respectively. These solutions give exponentially decaying and increasing wavefunctions. Requiring normalizability the bulk states in the TI become

$$\Psi_{B,\uparrow\downarrow}^R = \begin{pmatrix} \pm i e^{-i\phi} \\ 1 \end{pmatrix} \otimes \Xi_{B,\uparrow\downarrow}^R \tag{5.24}$$

with

$$\begin{aligned} \Xi_{B,\uparrow\downarrow}^R = \frac{1}{\sqrt{N_B}} \Big[& a_B^R \, \chi_{B,\uparrow\downarrow}^R(-\lambda_{B,+}^R) e^{-\lambda_{B,+}^R z} + b_B^R \, \chi_{B,\uparrow\downarrow}^R(i k_z) e^{i k_z z} \\ & + c_B^R \, \chi_{B,\uparrow\downarrow}^R(-i k_z) e^{-i k_z z} \Big], \end{aligned} \tag{5.25}$$

where $Re[\lambda_{B,+}^R] > 0$, a_B^R, b_B^R, c_B^R are complex coefficients, and

$$\chi_{B,\uparrow\downarrow}^{L/R}(\lambda) = \begin{pmatrix} \frac{\pm A_0 k_\| - B_0 \lambda}{E_B - M_0^{L/R} + \lambda^2 M_1} \\ 1 \end{pmatrix}. \tag{5.26}$$

In addition to the boundary conditions given by Eqs. (5.8) and (5.9) the bulk state solution given by Eqs. (5.22)-(5.26) has to obey probability current conservation, i.e., $|b_B^R|^2 = |c_B^R|^2$. Together with Eqs. (5.8) and (5.9), this leads to five equations for the five unknown coefficients $a_B^{L/R}, b_B^{L/R}, c_B^R$. Solving the resulting equations yields

$$\begin{aligned} \Xi_{B,\uparrow\downarrow}^R = \frac{1}{\sqrt{N_B}} \Big[& a_B^R \, \chi_{B,\uparrow\downarrow}^R(-\lambda_{B,+}^R) e^{-\lambda_{B,+}^R z} + b_B^R \, \chi_{B,\uparrow\downarrow}^R(i k_z) e^{i k_z z} \\ & - (b_B^R)^* \, \chi_{B,\uparrow\downarrow}^R(-i k_z) e^{-i k_z z} \Big] \end{aligned} \tag{5.27}$$
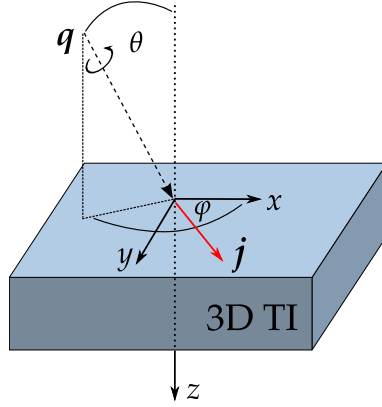
Figure 5.3: Light with wavevector q with an angle θ from the z-axis and azimuthal angle φ from the x-axis shines onto a 3D TI which occupies the half space $z < 0$. A photocurrent j is induced on the surface.

and $\Xi^L_{B,\uparrow\downarrow}$ is still given by Eq. (5.23). The expression for the coefficients $a^{L/R}_B, b^{L/R}_B$ do not give any further insight and can be found in App. C.2.

The bulk energy of the TI is given by

$$E_B = \pm\sqrt{A_0^2 k_\parallel^2 + B_0^2 k_z^2 + (M_0^R + M_1 k_z^2)^2} \tag{5.28}$$

and the states $\Psi_{B,\uparrow\downarrow}$ are degenerate.

In order to prove the orthogonality of the bulk states and determine the normalization constant N_B we have to evaluate Eq. (5.11), i.e.,

$$\int_{-\infty}^{\infty} dz\, \Psi_B^\dagger(k_z, z)\Psi_B(k'_z, z) = 2\left[\int_{-\infty}^{0} dz \left(\Xi^L_{B,\uparrow\downarrow}\right)^\dagger \Xi^L_{B,\uparrow\downarrow} + \int_{0}^{\infty} dz \left(\Xi^R_{B,\uparrow\downarrow}\right)^\dagger \Xi^R_{B,\uparrow\downarrow}\right], \tag{5.29}$$

where we already evaluated the spin overlaps. The first integral on the right hand side can be calculated in a straightforward manner since $\Xi^L_{B,\uparrow\downarrow}$ only contains exponentially decreasing functions. The second integral on the right hand side, however, contains functions of the form $e^{\pm ik_z z}$ which we need to treat carefully since we are only integrating over a semi-infinite interval. Using the relation

$$\int_{0}^{\infty} dz\, e^{\pm i\alpha z} = \lim_{\eta \to 0} \frac{\pm i}{\alpha \pm i\eta} = \pm iP\left(\frac{1}{\alpha}\right) + \pi\delta(\alpha), \tag{5.30}$$

where P denotes the Cauchy principal value, the second integral on the right hand side of Eq. (5.29) can be evaluated. After a lengthy but straightforward

calculation, we find that the bulk states are indeed orthonormal and that the normalization constant is given by

$$N_B = 4\pi \left| b_B^R \, \eta_{B,\uparrow\downarrow}^R (ik_z) \right|^2 . \tag{5.31}$$

The norm of the bulk wavefunctions is determined by the contribution from $z > 0$ only.

5.1.3 *Vector potential and interaction Hamiltonian*

As in the previous chapter, we are considering light incident onto the surface which lies in the xy-plane as illustrated in Fig. 5.3. For a polarization generated by a $\lambda/4$ wave plate rotated by an angle α and wavevector,

$$\boldsymbol{q} = q \begin{pmatrix} \sin\theta\cos\varphi \\ \sin\theta\sin\varphi \\ \cos\theta \end{pmatrix} . \tag{5.32}$$

the vector potential is given by

$$\boldsymbol{A}(t) = \frac{\mathcal{A}}{2} e^{-i\omega t + i\boldsymbol{q}\boldsymbol{r}} \begin{pmatrix} -\sin 2\alpha\sin\varphi + (i + \cos 2\alpha)\cos\theta\cos\varphi \\ \sin 2\alpha\cos\varphi + (i + \cos 2\alpha)\cos\theta\sin\varphi \\ (i + \cos 2\alpha)\sin\theta \end{pmatrix} + c.c. \tag{5.33}$$

Note that here we labeled the amplitude of the vector potential by $\mathcal{A}$ in contrast to the notation in Chap. 4 in order to avoid confusion with the parameter A_0 in the TI Hamiltonian in Eq. (5.1). The $\lambda/4$ wave plate changes the polarization of the light with a period of π from linearly P-polarized ($\alpha = 0$), to left-circularly polarized ($\alpha = \pi/4$), to P-polarized ($\alpha = \pi/2$), to right-circularly polarized ($\alpha = 3\pi/4$), and back to P-polarized ($\alpha = \pi$).

The interaction Hamiltonian is obtained by minimal coupling, $\boldsymbol{k} \to \boldsymbol{k} - (e/\hbar)\boldsymbol{A}$ in the Hamiltonian Eq. (5.1). The interaction Hamiltonian to first order in the vector potential can then be written as

$$H' = \frac{e}{\hbar} \left[-2M_1 A_z k_z \mathbf{1} \otimes \tau_z - B_0 A_z \mathbf{1} \otimes \tau_y - A_0(\sigma_x A_y - \sigma_y A_x) \otimes \tau_x \right] . \tag{5.34}$$

We only want to consider absorption processes and thus write the interaction Hamiltonian in the form $H' = H'_+ + H'_-$, where $H'_\pm \propto A_\pm = A_0 e^{\pm i\omega t}$ describes the emission and absorption of a photon, respectively.

5.2 CALCULATION OF THE PHOTOCURRENT

In calculating the photocurrent density, we again neglect the photon momentum and consider vertical transitions that conserve the in-plane momentum $k_\parallel$. The momentum perpendicular to the surface, k_z, is naturally not conserved but determined by energy conservation.

The allowed photoexcitation processes depend on the Fermi level. For a Fermi energy inside the BCB, the only allowed transitions between surface and bulk are from the surface states into the unoccupied BCB states [cf. Fig. 5.1]. For a Fermi energy in the BVB, we have to consider transitions from the BVB into the Dirac cone. In the following, we show the calculation of the photocurrent for excitations from the Dirac cone into the BCB. The photocurrent response from other processes can be calculated analogously.

The photocurrent density can be calculated analogously to the previous chapter [cf. Eq. (4.10)] and we again assume that the current relaxes on the scale of the momentum relaxation time τ_k,

$$j = - \frac{2\pi e \tau_k}{\hbar} \sum_{\alpha,\beta=\uparrow\downarrow} \sum_{k} (v_B - v_{S,\beta})$$

$$\times \left| \langle \Psi_{B,\alpha}(k_\parallel, k_z, z) | H'_-(k_z \to -i\partial_z) | \Psi_{S,\beta}(k_\parallel, z) \rangle \right|^2 \delta(E_B - E_S - \hbar\omega), \quad (5.35)$$

where the sum is over occupied surface and unoccupied bulk states, k is the 3D momentum, $E_S = A_0 k_\parallel$ for $\Psi_{S,\uparrow}$ and $E_S = -A_0 k_\parallel$ for $\Psi_{S,\downarrow}$. The velocities are given by

$$v_{S,\uparrow\downarrow} = \langle \Psi_{S,\uparrow\downarrow} | \frac{\partial H}{\partial k_\parallel} | \Psi_{S,\uparrow\downarrow} \rangle$$

$$= \pm \frac{A_0}{\hbar} \hat{k}_\parallel \quad (5.36)$$

and

$$v_{B,\uparrow\downarrow} = \langle \Psi_{B,\uparrow\downarrow} | \frac{\partial H}{\partial k} | \Psi_{B,\uparrow\downarrow} \rangle$$

$$= \frac{A_0^2 k_\parallel}{\hbar E_B} \hat{k}_\parallel. \quad (5.37)$$

The expectation value of the bulk velocity in the z-direction, i.e., perpendicular to the surface, vanishes. The reason is that the bulk states near the surface given

by Eq. (5.27) are a superposition of states that propagate in the $\pm z$-direction. This is a comforting results considering that we are interested in photocurrents on the surface. If the electrons excited from the surface into the bulk acquired a finite velocity perpendicular to the surface, they would quickly move into the bulk and be lost to the surface photocurrent response. Once the current is generated at the surface, electrons in the bulk states, of course, might drift or diffuse away from the surface leading to the relaxation of the surface photocurrent.

5.2.1 ϕ-integration

In order to calculate the photocurrent density given by Eq. (5.35) we start with the interaction matrix elements $\langle \Psi_B | H'_- | \Psi_S \rangle$. For a transition between the surface valence band (SVB) and the BCB we get

$$
|\langle \Psi_{B,\uparrow} | H'_- | \Psi_{S,\downarrow} \rangle|^2 = \left(\frac{2eA_0}{\hbar} \right)^2 \left| (A_{-,y} \cos\phi - A_{-,x} \sin\phi) \langle \Xi_{B,\uparrow} | \tau_x | \Xi_{S,\downarrow} \rangle \right|^2 .
$$

(5.38)

and

$$
|\langle \Psi_{B,\downarrow} | H'_- | \Psi_{S,\downarrow} \rangle|^2 = \Bigg| -\frac{2e}{\hbar} \langle \Xi_{B,\downarrow} | - 2iM_1 A_{-,z} \tau_z \partial_z + B_0 A_{-,z} \tau_y | \Xi_{S,\downarrow} \rangle
$$
$$
+ \frac{2eA_0}{\hbar} \left(A_{-,y} \sin\phi + A_{-,x} \cos\phi \right) \langle \Xi_{B,\downarrow} | \tau_x | \Xi_{S,\downarrow} \rangle \Bigg|^2 , \quad (5.39)
$$

where ϕ is the polar angle of the in-plane momentum with $\tan\phi = k_y / k_x$. $A_{-,i}$ describes the i-th component of the vector potential $\propto e^{-i\omega t}$ indicating that we are only considering absorption processes. From now on we will neglect the index $'-'$ in the vector potential components for brevity.

The orbital overlaps $\langle \Xi_{B,\uparrow\downarrow} | \tau_x | \Xi_{S,\downarrow} \rangle$ in Eqs. (5.38) and (5.39) are independent of ϕ. Through the summation over k_x and k_y, the photocurrent will eventually involve an integration over ϕ and the only other term in the integrand of Eq. (5.35), which depends on the polar angle, is the velocity $(v_B - v_S) \propto (\cos\phi\, \hat{x} + \sin\phi\, \hat{y})$. We can easily see that the induced photocurrent for transitions $\Psi_{S,\downarrow} \to \Psi_{B,\uparrow}$ vanishes since the ϕ-integration yields zero. The photocurrent induced by transitions from the SVB thus simplifies to

$$
j_\downarrow = -\frac{2\pi e \tau_k}{\hbar} \sum_k (v_B - v_{S,\downarrow}) \left| \langle \Psi_{B,\downarrow}(\mathbf{k}_\parallel, k_z, z) | H'_-(k_z \to -i\partial_z) | \Psi_{S,\downarrow}(\mathbf{k}_\parallel, z) \rangle \right|^2
$$
$$
\times \delta(E_B + A_0 k_\parallel - \hbar\omega) \tag{5.40}
$$

Analogously, one can see that for transitions from the surface conduction band (SCB) to the BCB only the transition $\Psi_{S,\uparrow} \to \Psi_{B,\uparrow}$ will give a contribution to the photocurrent, and we get

$$j_\uparrow = -\frac{2\pi e \tau_k}{\hbar} \sum_k (v_B - v_{S,\uparrow}) \left| \langle \Psi_{B,\uparrow}(\boldsymbol{k}_\|, k_z, z) | H'_-(k_z \to -i\partial_z) | \Psi_{S,\uparrow}(\boldsymbol{k}_\|, z) \rangle \right|^2$$
$$\times \delta(E_B - A_0 k_\| - \hbar\omega). \tag{5.41}$$

Only transitions between surface and bulk states with equal spin orientations contribute to the photocurrent response. The total photocurrent density is simply given by $j = j_\uparrow + j_\downarrow$. Looking at Eq. (5.39) and considering the ϕ-integration we can further simplify the expression for the photocurrent. For brevity we write

$$|\langle \Psi_{B,\uparrow\downarrow} | H'_- | \Psi_{S,\uparrow\downarrow} \rangle|^2 = \left(\frac{2e}{\hbar}\right)^2 \left| A_z O_{\uparrow\downarrow,yz} + (A_y \sin\phi + A_x \cos\phi) O_{\uparrow\downarrow,x} \right|^2 \tag{5.42}$$

with

$$O_{\uparrow\downarrow,yz} = -\langle \Xi_{B,\uparrow\downarrow} | - 2iM_1 \tau_z \partial_z + B_0 \tau_y | \Xi_{S,\uparrow\downarrow} \rangle \tag{5.43}$$
$$O_{\uparrow\downarrow,x} = \mp A_0 \langle \Xi_{B,\uparrow\downarrow} | \tau_x | \Xi_{S,\uparrow\downarrow} \rangle, \tag{5.44}$$

where in Eq. (5.44) the upper sign again corresponds to '$\uparrow$', i.e., excitations from the SCB, and the lower sign corresponds to '$\downarrow$', i.e., excitations from the SVB.

For the transitions $\Psi_{S,\downarrow} \to \Psi_{B,\downarrow}$ and $\Psi_{S,\uparrow} \to \Psi_{B,\uparrow}$ only terms $\propto O^*_{\uparrow\downarrow,yz} O_{\uparrow\downarrow,x} + c.c.$ can give a finite photocurrent. All other terms vanish when the ϕ-integration is performed. The contributions to the photocurrent thus simplify to

$$j_{\uparrow\downarrow} = -\frac{16\pi e^3 \tau_k}{\hbar^3} \sum_k \delta(E_B \mp A_0 k_\| - \hbar\omega)(v_B - v_{S,\uparrow\downarrow})$$

$$\times \left\{ \left(Re[O^*_{\uparrow\downarrow,yz} O_{\uparrow\downarrow,x}] Re[A_z^* A_x] - Im[O^*_{\uparrow\downarrow,yz} O_{\uparrow\downarrow,x}] Im[A_z^* A_x] \right) \cos^2\phi \, \hat{\boldsymbol{x}} \right.$$

$$\left. + \left(Re[O^*_{\uparrow\downarrow,yz} O_{\uparrow\downarrow,x}] Re[A_z^* A_y] - Im[O^*_{\uparrow\downarrow,yz} O_{\uparrow\downarrow x}] Im[A_z^* A_y] \right) \sin^2\phi \, \hat{\boldsymbol{y}} \right\}, \tag{5.45}$$

where we used Eqs. (5.36) and (5.37). The upper sign in the δ-function corresponds to $j_\uparrow$ and the lower sign to $j_\downarrow$.

Looking at Eq. (5.43) and (5.44) we can simplify the expression for the photocurrent even further. The bulk and surface wavefunctions can be chosen real

which leads to $O_{\uparrow\downarrow,yz}$ being purely imaginary and $O_{\uparrow\downarrow,x}$ being purely real. Thus $Re[O^*_{\uparrow\downarrow,yz}O_{\uparrow\downarrow,x}] = 0$ and the contributions to the photocurrent become

$$j_{\uparrow\downarrow} = \frac{16\pi e^3 \tau_k}{\hbar^3} \sum_k \delta(E_B \mp A_0 k_{\parallel} - \hbar\omega) Im[O^*_{\uparrow\downarrow,yz}O_{\uparrow\downarrow,x}](v_B - v_{S,\uparrow\downarrow})$$

$$\times \left\{ Im[A_z^* A_x] \cos^2 \phi \, \hat{x} + Im[A_z^* A_y] \sin^2 \phi \, \hat{y} \right\}. \tag{5.46}$$

From this expression we can already gain insight into the polarization dependence of the photocurrent. The vector potential components can be pulled in front of the sum and we can write

$$j \propto \begin{pmatrix} Im[A_z^* A_x] \\ Im[A_z^* A_y] \end{pmatrix}. \tag{5.47}$$

With the vector potential given by Eq. (5.33) this becomes

$$j \propto -\sin(2\alpha) \sin\theta \begin{pmatrix} -\sin\varphi \\ \cos\varphi \end{pmatrix}. \tag{5.48}$$

Thus, the current generated by optically induced transitions between surface and bulk states changes sign when switching the helicity of the light between left- ($\alpha = \pi/4$) and right-circular ($\alpha = 3\pi/4$) polarization, and vanishes for P-linear polarization ($\alpha = 0, \pi/2, \pi$). The photocurrent also vanishes for S-linearly polarized light since then $A_z = 0$. The current flows perpendicular to the plane of incidence of the light [cf. Eq. (5.32)] and vanishes for normal incidence, i.e., $\theta = 0$. This qualitative behavior of the photocurrent is in agreement with the crystal symmetry of Bi_2Se_3 and the symmetry analysis of the CPGE presented in Chap. 2 [cf. Eq. (2.45)]. We have seen in Chap. 2 that the crystal has a rotational symmetry around the z-direction, i.e., perpendicular to the surface. Thus the photocurrent has to vanish for normal incidence. Among others, the crystal surface also has a mirror axis along the y-direction. For light incident in a plane parallel to the mirror axis, reflection about the mirror axis changes the helicity of the light and changes the sign of a current in the x-direction. A current along the y-direction remains invariant. Thus, helicity-dependent currents have to flow perpendicular to the plane of incidence of the light.

5.2.2 $k_\parallel$-integration

Having established the helicity dependence of the photocurrent, we now turn to the explicit evaluation of Eq. (5.46). The ϕ-integration can be easily performed leaving us with an integration over $k_\parallel$ and k_z. The integral over $k_\parallel$ can be calculated using the δ-function. We are considering transitions into the bulk conduction band, i.e., $E_B > 0$, and can write

$$\delta(E_B - E_S - \hbar\omega) = 2E_B\delta\left(E_B^2 - (\hbar\omega + E_S)^2\right), \tag{5.49}$$

such that we get

$$\delta(E_B - A_0 k_\parallel - \hbar\omega) = \frac{E_B}{A_0 \hbar\omega}\delta\left(\frac{B_0^2 k_z^2 + (M_0^R + M_1 k_z^2)^2 - \hbar^2\omega^2}{2A_0\hbar\omega} - k_\parallel\right), \tag{5.50}$$

$$\delta(E_B + A_0 k_\parallel - \hbar\omega) = \frac{E_B}{A_0 \hbar\omega}\delta\left(\frac{-B_0^2 k_z^2 - (M_0^R + M_1 k_z^2)^2 + \hbar^2\omega^2}{2A_0\hbar\omega} - k_\parallel\right). \tag{5.51}$$

These δ-functions give a restriction for the k_z-integration interval because $k_\parallel \geq 0$.

Inserting the expression for the δ-function into Eq. (5.46) and performing the ϕ- and $k_\parallel$-integrations gives

$$j_{\uparrow\downarrow} = -D_{\uparrow\downarrow}\frac{e^3 \mathcal{E}_0^2 \tau_k A_0}{2\pi\hbar^3\omega}\sin(2\alpha)\sin\theta\begin{pmatrix} -\sin\varphi \\ \cos\varphi \end{pmatrix}, \tag{5.52}$$

where $\mathcal{E}_0$ is the electric field amplitude,

$$D_\uparrow = -\frac{1}{A_0\hbar\omega}\int_0^\infty dk_z\, \tilde{k}_{\parallel,\uparrow,x}\, Im[O_{\uparrow,yz}^* O_{\uparrow,x}]\Big|_{k_\parallel=\tilde{k}_{\parallel,\uparrow}(k_z)}\Theta\left(\tilde{k}_{\parallel,\uparrow}(k_z)\right)$$
$$\times \Theta\left(k_F - \tilde{k}_{\parallel,\uparrow}(k_z)\right) \tag{5.53}$$

and

$$D_\downarrow = \frac{1}{A_0\hbar\omega}\int_0^\infty dk_z\, \tilde{k}_{\parallel,\downarrow}(k_z)\, Im[O_{\downarrow,yz}^* O_{\downarrow,x}]\Big|_{k_\parallel=\tilde{k}_{\parallel,\downarrow}(k_z)}\Theta\left(\tilde{k}_{\parallel,\downarrow}(k_z)\right). \tag{5.54}$$

The overlaps $O_{\uparrow\downarrow,i}$ are given by Eqs. (5.43) and (5.44), $\Theta(x)$ denotes the Heaviside step function, and

$$\tilde{k}_{\parallel,\uparrow\downarrow}(k_z) = \pm\frac{B_0^2 k_z^2 + (M_0^R + M_1 k_z^2)^2 - \hbar^2\omega^2}{2A_0\hbar\omega}. \tag{5.55}$$

Eq. (5.52) is the final analytical expression for the photocurrent induced on the surface of a 3D TI by excitations from surface into bulk states.

A_0 (eV Å)	B_0 (eV Å)	M_0^R (eV)	M_1 (eV Å^2)
3.33	2.26	-0.28	6.86

Table 5.1: Numerical values for parameters of the bulk Hamiltonian given by Eq. (5.1) [Liu et al., 2010]

5.2.3 k_z-integration

In order to obtain a quantitative estimate of the magnitude of the photocurrent and the dependence on system parameters such as the bulk gap inside the normal insulator M_0^L or the photon energy $\hbar\omega$, we need to evaluate the coefficients $D_{\uparrow\downarrow}$. These can be obtained by numerical integration and the Θ-functions impose limits on the integration intervals. For transitions between the SCB and the BCB, energy conservation sets a minimum value for k_z, while the Fermi level gives an upper bound to the integration. For transitions from the SVB to the BCB we get a maximum value for k_z. Using the Θ-functions to cut off the semi-infinite integration intervals, we find

$$D_\uparrow = -\frac{1}{A_0\hbar\omega} \int_{k_{z,\min,\uparrow}}^{k_{z,\max,\uparrow}} dk_z\, \tilde{k}_{\|,\uparrow,x}\, Im[O_{\uparrow,yz}^* O_{\uparrow,x}]\Big|_{k_\|=\tilde{k}_{\|,\uparrow}(k_z)} \tag{5.56}$$

and

$$D_\downarrow = \frac{1}{A_0\hbar\omega} \int_0^{k_{z,\max,\downarrow}} dk_z\, \tilde{k}_{\|,\downarrow}(k_z)\, Im[O_{\downarrow,yz}^* O_{\downarrow,x}]\Big|_{k_\|=\tilde{k}_{\|,\downarrow}(k_z)} \tag{5.57}$$

with

$$k_{z,\min,\uparrow} = \sqrt{-\frac{B_0^2 + 2M_0^R M_1}{2M_1^2} + \sqrt{\left(\frac{B_0^2 + 2M_0^R M_1}{2M_1^2}\right)^2 + \frac{\hbar^2\omega^2 - (M_0^R)^2}{M_1^2}}}$$

$$= k_{z,\max,\downarrow} \tag{5.58}$$

and

$$k_{z,\max,\uparrow} = \left(-\frac{B_0^2 + 2M_0^R M_1}{2M_1^2} \right.$$

$$\left. + \sqrt{\left(\frac{B_0^2 + 2M_0^R M_1}{2M_1^2}\right)^2 + \frac{\hbar^2\omega^2 + 2A_0\hbar\omega k_F - (M_0^R)^2}{M_1^2}} \right)^{1/2} . \tag{5.59}$$

Before we can finally calculate the factors $D_{\uparrow\downarrow}$ we first need to evaluate the overlap integrals given by Eqs. (5.43) and (5.44), i.e.,

$$
O_{\uparrow\downarrow,yz} = -\left\{ \int_{-\infty}^{0} dz (\Xi_{B,\uparrow\downarrow}^{L})^{\dagger}(-2iM_1\tau_z\partial_z + B_0\tau_y)\Xi_{S,\uparrow\downarrow}^{L} \right.
$$
$$
\left. + \int_{0}^{\infty} dz (\Xi_{B,\uparrow\downarrow}^{R})^{\dagger}(-2iM_1\tau_z\partial_z + B_0\tau_y)\Xi_{S,\uparrow\downarrow}^{R} \right\} \tag{5.60}
$$
$$
O_{\uparrow\downarrow,x} = \mp\left\{ \int_{-\infty}^{0} dz (\Xi_{B,\uparrow\downarrow}^{L})^{\dagger}(A_0\tau_x)\Xi_{S,\uparrow\downarrow}^{L} + \int_{0}^{\infty} dz (\Xi_{B,\uparrow\downarrow}^{R})^{\dagger}(A_0\tau_x)\Xi_{S,\uparrow\downarrow}^{R} \right\} \tag{5.61}
$$

with $\Xi_{S,\uparrow\downarrow}^{L/R}$ given by Eqs. (5.13) and (5.18) and $\Xi_{B,\uparrow\downarrow}^{L/R}$ given by Eqs. (5.23) and (5.27). Although the calculation is lengthy, the integrals can be performed in a straightforward way since the surface state wavefunctions decay exponentially away from $z = 0$ and there is no problem with convergence. We find that to leading order in $1/M_0^L$ the factors $D_{\uparrow\downarrow}$ are solely determined by the overlap matrix elements of the TI wavefunctions at $z > 0$. The reason is the same as for the surface state norm above. For a large gap M_0^L the wavefunctions on side of the normal insulator fall off rapidly and their contribution to the transitions can be neglected. We can thus approximate

$$
O_{\uparrow\downarrow,yz} \simeq \int_{0}^{\infty} dz (\Xi_{B,\uparrow\downarrow}^{R})^{\dagger}(-2iM_1\tau_z\partial_z + B_0\tau_y)\Xi_{S,\uparrow\downarrow}^{R} \tag{5.62}
$$
$$
O_{\uparrow\downarrow,x} \simeq \int_{0}^{\infty} dz (\Xi_{B,\uparrow\downarrow}^{R})^{\dagger}(A_0\tau_x)\Xi_{S,\uparrow\downarrow}^{R}. \tag{5.63}
$$

Using Eqs. (5.58), (5.59), (5.62), and (5.63) we can now evaluate the coefficients $D_{\uparrow\downarrow}$ given by Eqs. (5.56) and (5.57).

5.3 NUMERICAL RESULTS

In this section we turn to numerically evaluating the coefficients $D_{\uparrow\downarrow}$ to obtain a quantitative estimate for the photocurrent. For the numerical results discussed we use the parameters obtained by Liu et al. [2010] and listed in Tab. 5.1. We, however, still have to determine an appropriate value for $M_0^L > 0$, i.e., the size of the band gap inside the trivial insulator. Considering transitions from the Dirac cone into the BCB, an electron can only be photoexcited within the TI but not photoemitted into the trivial insulator as long as $M_0^L > \hbar\omega + E_S$, where E_S is the surface state energy. If $M_0^L < \hbar\omega + E_S$ electrons could be emitted into the trivial
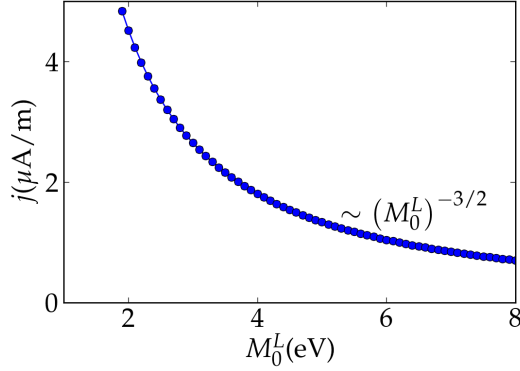
Figure 5.4: Photocurrent from transitions between the surface Dirac cone to the BCB as a function of the insulating gap M_0^L.

insulator. Thus M_0^L is similar to a work function of the TI and we choose $M_0^L = 6$ eV [Sobota et al., 2013].

An interesting result is that the photocurrent vanishes in the limit $M_0^L \to \infty$ as illustrated in Fig. 5.4. This implies that the photocurrent response vanishes for open boundary conditions, i.e., when the wavefunction is required to vanish at the surface. For large M_0^L we find a functional dependence of $j \sim \left(M_0^L\right)^{-3/2}$.

We would also like to understand the microscopic origin of the photocurrent in more detail. That a finite photocurrent is indeed generated tells us that photoinduced transitions between surface and bulk states take place asymmetrically in momentum space. We do not know, however, whether the photocurrent is dominated by excitations near the Dirac point, i.e., at small in-plane momenta $k_\parallel$, or whether transitions at larger $k_\parallel$ generate the main contribution to the photocurrent. We thus analyze the integrand of Eqs. (5.56) and (5.57) as a function of $k_\parallel$ as illustrated in Figs. 5.5 (a) and (b). For both kinds of transitions, i.e., from SVB to BCB and from SCB to BCB, we find significant contributions from large $k_\parallel$. For excitations from the SCB to the BCB the integrand increases linearly with $k_\parallel$ such that contributions from larger $k_\parallel$ clearly dominate. For transitions from the SVB to the BCB the integrand exhibits a maximum as a function of $k_\parallel$. The different behavior of the integrands for transitions from the SVB to the BCB and from the SCB to the BCB for large $k_\parallel$ reflect the different dependencies of the available phase space of transitions. For the case SVB $\to$ BCB, the phase space of allowed transitions vanishes once $A_0 k_\parallel + E_B > \hbar\omega$, i.e., the photon does not have enough energy to excite electrons into the bulk at such large $k_\parallel$. For the case SCB $\to$ BCB, on the other hand, the only restriction is the chosen Fermi momentum, i.e., $k_\parallel \leq k_F$. Thus when calculating the photocurrent one has to take
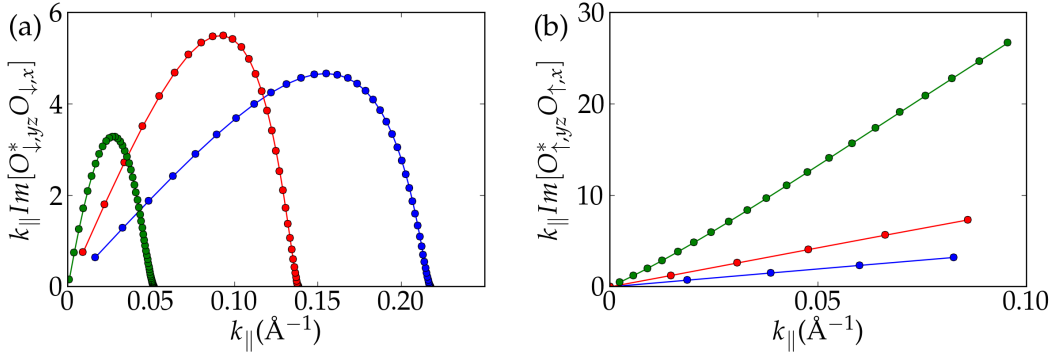
Figure 5.5: Integrands of (a) Eq. (5.56) and (b) Eq. (5.57). (a) Integrand for SVB → BCB as a function of $k_\parallel$ for $\hbar\omega = 1.5$ eV (blue), $\hbar\omega = 1.0$ eV (red), and $\hbar\omega = 0.5$ eV (green). (b) Analogous plot for the integrand for SCB → BCB. In both cases transitions at large $k_\parallel$ contribute significantly to the photocurrent.

into account transitions at all in-plane momenta $k_\parallel$ that are allowed by energy conservation.

As a function of Fermi momentum, we find that the current decreases as the Fermi level is lowered from inside the BCB towards the Dirac point and reverses sign for negative Fermi energy as illustrated in Fig. 5.6. The decrease in the photocurrent when lowering the Fermi level has two reasons. One, for smaller k_F the contribution to the photocurrent due to excitations from the SCB to the BCB band obviously decreases [cf. Fig. 5.7 (a)]. Second, as the Fermi level is lowered one also starts to allow transitions where an electron from the BVB is excited into the SCB as illustrated in Fig. 5.7 (b). This process results in a current that flows in the opposite direction as the current from transitions from the SVB or the SCB to the BCB. Thus lowering the Fermi level results in a cancellation between the photocurrent contributions due to transitions from the surface states into the BCB and transitions from the BVB into the surface states. Once the Fermi level is lowered below the Dirac point into the BVB, only transitions between the BVB and the surface states are allowed. The resulting photocurrent is of the same order of magnitude as the photocurrent for a Fermi level inside the BCB but flows in the opposite direction. This is illustrated in Fig. 5.5. For small Fermi momentum, we find that the photocurrent behaves as $\sim k_F^2$. That the current vanishes for a Fermi level directly at the Dirac point is due to the particle-hole symmetric model we are using. Fig. 5.7 (b) shows that for $k_F = 0$ electron and hole contributions to the current cancel exactly.
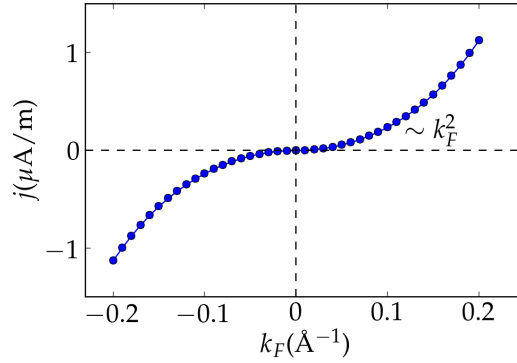
Figure 5.6: Photocurrent as a function of Fermi momentum, where negative k_F corresponds to a negative Fermi energy. The current switches sign for positive and negative Fermi level. For $k_F \to 0$ we find that the current vanishes as $\sim k_F^2$.

5.4 SUMMARY

We studied the surface photocurrent response of 3D TIs at large photon energies that make it necessary to account for bulk states. We find that photoinduced transitions between the Dirac surface states and the bulk states generate a finite photocurrent. This photocurrent is helicity-dependent, i.e., reverses its direction when the polarization of the light is switched between left- and right-circularly polarized. The current vanishes for linear polarization and for normal incidence of the light and flows perpendicular to the plane of incidence of the light. When lowering the Fermi level from the BCB towards the Dirac point, the current decreases, eventually flowing in the opposite direction when the Fermi level resides in the BVB.

We find that the photocurrent has significant contributions from transitions at large in-plane momenta $k_\parallel$, $k_\parallel \sim 0.2$ Å^{-1} for $\hbar\omega = 1.5$ eV. One should note that such large values of $k_\parallel$ strain the applicability of our model Hamiltonian, given by Eq. (5.1), to the specific TI Bi$_2$Se$_3$. We neglected terms quadratic in the in-plane momentum and the numerical values for the constant parameters where obtained from $\mathbf{k} \cdot \mathbf{p}$ theory which is only valid near the Dirac point [Liu et al., 2010]. Nevertheless, the model describes a 3D TI and thus our results give valuable insight into photocurrent generation on TI surfaces.

Even though our model might not quantitatively describe the 3D TI Bi$_2$Se$_3$, it is still interesting to compare our results to the experiment discussed in Chap. 3.
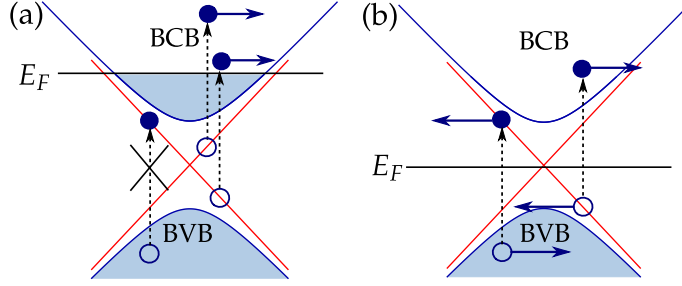
Figure 5.7: Possible photoexcitation processes for a Fermi level (a) inside BCB (b) directly at the Dirac point. Only excitations from the surface Dirac cone into the BCB are allowed generating a finite photocurrent. (b) Due to the particle-hole symmetry of our model, the electron and hole contributions to the current cancel leading to a vanishing photocurrent.

McIver et al. [2012] measured helicity-dependent and helicity-independent contributions to the photocurrent with a possible Dirac cone origin. Qualitatively, we find a helicity-dependent photocurrent perpendicular to the plane of incidence of the light as measured in the experiment. We do not, however, find any helicity-independent contributions to the current. Quantitatively, with a Fermi level near the bottom of the BCB, a laser power of 1 W/cm^2, and a photon energy of $\hbar\omega = 1.5$ eV as in the experiment, we find a photocurrent of order ~ 1 pA/(W/cm^2) as measured by McIver et al. [2012], when we assume a momentum relaxation time of $\tau_k = 10$ ps. The latter seems quite large as momentum relaxation times of the order of $0.01 - 0.1$ ps have been reported for the surface states of Bi$_2$Se$_3$ [Butch et al., 2010; Zhang et al., 2013].

One should note that the photocurrent generated on the surface of a TI by transitions between surface and bulk states is not necessarily protected against direct backscattering since part of the current is carried by electrons (or holes) in bulk states. Bulk states are spin degenerate and direct backscattering is not forbidden. In addition, the resulting current is not completely spin polarized, even though it is helicity-dependent. For a Fermi level inside the BCB at $k_F = 0.2$ Å^{-1}, $M_0^L = 6$ eV, and $\hbar\omega = 1.5$ eV, the degree of polarization is $(j_\downarrow - j_\uparrow)/(j_\downarrow + j_\uparrow) \sim 70$ %.

After providing a detailed analysis of photocurrent generation in TIs we proceed in the next chapter with the study of photocurrent relaxation in Dirac systems.

6

CURRENT AMPLIFICATION AND RELAXATION IN DIRAC SYSTEMS

In the previous chapters we gave a detailed analysis of photocurrent generation on TI surfaces but the magnitude of a photocurrent is, of course, not only determined by the amount of current that is generated but also by how fast it relaxes. The magnitude of the photoresponse is governed by a competition between optical excitation and subsequent relaxation of carriers and a complete understanding of the photoresponse of TIs requires the study of both effects. In this chapter, we extend our analysis of photocurrents and study the effect of relaxation of excited carriers on the current response in TIs.

The content and results of this chapter were previously published as [Junck et al., 2014].

6.1 INTRODUCTION

In the simplest picture, photocurrents are carried by highly excited electron-hole pairs with electron and hole moving in opposite directions. In principle, any scattering event that changes the direction of motion of the particles can relax the current. For a quadratic dispersion we know that any momentum conserving scattering event will not affect the current. In this case velocity is proportional to momentum and as the current is proportional to the velocity, the current is also proportional to momentum. Thus momentum conserving scattering events do not change the current. This argument breaks down when one considers linear dispersions as exhibited by the surface states of TIs. Here velocity is no longer proportional to momentum and even momentum conserving scattering events

can change the current. In this chapter we focus on the limit of a perfectly linear dispersion and our results can therefore also be applied to current relaxation in other linearly dispersing system such as graphene.

Relaxation of current can, in general, occur through electron-phonon, disorder, or electron-electron (e-e) scattering. In this chapter we consider a sufficiently clean regime such that we can neglect disorder scattering. For sufficiently low temperatures one expects that electron-electron scattering will dominate over electron-phonon scattering. In graphene at low temperatures, e-e scattering can be more effective than electron-phonon scattering in relaxing excited carriers when particles are excited below the optical phonon frequencies with low pump fluences [Winzer et al., 2010; Kim et al., 2011; Winzer and Malic, 2012; Song et al., 2013, 2011; Tani et al., 2012]. We will thus assume that e-e scattering provides the dominant relaxation mechanism.

Much work has already been done on energy relaxation of excited carriers in Dirac systems both theoretically [Cheianov and Fal'ko, 2006; Butscher et al., 2007; Stauber et al., 2007; Tse and Das Sarma, 2009; Winzer et al., 2010; Kim et al., 2011; Winzer and Malic, 2012; Song et al., 2013; Tomadin et al., 2013] and experimentally [Hsieh et al., 2011; Kumar et al., 2011; Breusing et al., 2011; Sobota et al., 2012; Hajlaoui et al., 2012; Tani et al., 2012; Gierz et al., 2013; Brida et al., 2013]. Specifically it was predicted [Malic et al., 2011] and experimentally observed [Mittendorff et al., 2014] that for an anisotropic photoexcited distribution in the Dirac cone, which is, however, symmetric in momentum space and thus carries no net current, e-e scattering tends to preserve the anisotropy over time scales of the order of $\gtrsim 100$ fs. Due to the helical spin structure of the Dirac electrons, direct backscattering is forbidden and Coulomb interaction is dominant for scattering events with small momentum transfer [Malic et al., 2011]. Another effect that is based on e-e scattering in Dirac systems is carrier multiplication [Winzer et al., 2010; Winzer and Malic, 2012; Song et al., 2013]. A highly excited electron relaxes in small energy steps, exciting a particle-hole pair in each step. This 'relaxation cascade' [Song et al., 2013] can produce a large number of excited carriers depending on the strength of the pump fluence. Experimentally, carrier multiplication has been observed in pump-probe experiments with low pump fluences [Tani et al., 2012; Tielrooij et al., 2013; Plötzing et al., 2014] but no evidence was found in time- and angle-resolved photoemission experiments using large pump fluences of the order of ~ 1 mJ/cm^2 [Gierz et al., 2013; Johannsen et al., 2013]. The reason is that for a high density of excited electrons relaxation processes that do not lead to carrier multiplication such as recombination of

electrons and holes or phonon scattering become more important [Winzer and Malic, 2012; Song et al., 2013].

While it has been studied that e-e interaction can lead to these interesting effects in signatures of energy relaxation, the question remains how e-e scattering affects the current in Dirac systems. Again, while e-e scattering cannot affect the current in quadratically dispersing systems, due to its momentum conserving character, the same is not true for systems with a linear dispersion. Velocity is no longer proportional to momentum and e-e scattering can change and relax the current [Müller and Sachdev, 2008]. In 2012, Sun et al. investigated the effect of a hot carrier background on the photocurrent and found that it effectively reduces the current, with the relaxation rate determined by the density of the thermal carrier background.

In this chapter, we study the effect of e-e scattering on the current in a very different regime. We consider a single excited electron, hole, or electron-hole pair undergoing scattering processes as the ones illustrated in Fig. 6.1. We give a detailed analysis of how these e-e scattering processes of highly excited particles in Dirac materials can affect current relaxation and obtain surprising results. For a photocurrent associated with a photoexcited electron-hole pair, the process of current relaxation occurs in a highly anisotropic manner for electron and hole. For a Fermi energy above the Dirac point, the current carried by a single electron actually increases due to e-e scattering, while the current carried by a single hole relaxes. In combination the current relaxation of zero-momentum electron-hole pairs is strongly suppressed as the amplification of the 'electron current' partially cancels the relaxation of the 'hole current'. Quantitatively we find that in the limit of large excitation energies ϵ_1 of the initially excited carriers, the rate of change of the electron and hole currents varies linearly with ϵ_F/ϵ_1, but with opposite signs. For the photocurrent carried by an electron-hole pair these two linear contributions cancel and the photocurrent relaxation is suppressed relative to the individual currents. The photocurrent is dominated by subleading contributions of the order of $\sim (\epsilon_F/\epsilon_1)^{3/2}$.

We will explain in detail the origin of the current amplification that occurs for a single initially excited carrier in the limit of a single scattering event and after full momentum-conserving equilibration, i.e., after many scattering events. We find that the change in current due to e-e scattering strongly depends on the position of the Fermi level. For a single excited electron, the current increases for a positive Fermi energy $\epsilon_F > 0$ and decreases for negative Fermi energy. For a single excited hole the picture is reversed. Here the current increases for a Fermi
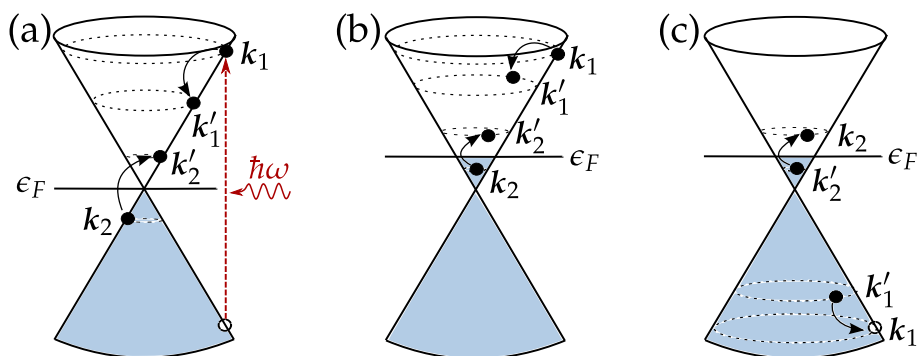
Figure 6.1: Absorption of a photon creates an electron-hole pair within the Dirac cone. The hot electron then relaxes by scattering off an electron in the Fermi sea and exciting an electron-hole pair. The dashed circles indicate constant energy contours and are a guide to the eye. (a) A possible relaxation process of the excited electron for $\epsilon_F = 0$ and (b) for $\epsilon_F > 0$. (c) A possible relaxation process of the excited hole for $\epsilon_F > 0$.

level below the Dirac point and decreases for a Fermi energy above the Dirac point. For a Fermi energy exactly at the Dirac point, the current is unaffected by e-e scattering and no current relaxation occurs.

6.2 MANY SCATTERING EVENTS

We will first consider the limit of many scattering events, when the system is fully equilibrated under the constraint of momentum conservation. Although this limit hides subtleties of the relaxation process it provides a platform to clearly demonstrate the intricacies of current relaxation due to e-e scattering. As explained above, assume that the sample is sufficiently clean and that temperatures are sufficiently low to neglect impurity and electron-phonon scattering. Then e-e collisions provide the dominant relaxation mechanism and many scattering events will lead to full equilibration of the system with the constraint that total momentum remains conserved during the relaxation process. With this information we can determine the final current that flows in the system after relaxation.

The picture is simplest when considering the photocurrent associated with a photoexcited electron-hole pair. Neglecting as usual the momentum change in the photon absorption process, the initial photoexcited state consisting of electron and hole has zero total momentum. Due to momentum conservation the

systems has to relax to a Fermi distribution with is centered at zero momentum which means that after many scattering events the photocurrent relaxes back to zero. While this result may seem obvious, there is actually a subtle structure underlying it that only becomes visible when considering the relaxation of the individual electron and hole currents separately.

Now consider the case of a single excited electron with initial energy $\epsilon_i > 0$. When this electron has completely relaxed by e-e collisions, momentum conservation tell us that the electron's initial momentum will be distributed over the entire Fermi sea. Thus we can determine the final current after complete momentum-conserving equilibration. For $\epsilon_F > 0$ and an initial momentum of the excited electron $\boldsymbol{k}_i = k_i \hat{\boldsymbol{x}}$, the final current is given by

$$j_f = -\frac{e\hbar v_F^2}{(2\pi)^2} \hat{\boldsymbol{k}}_i \int dk \, k \int d\phi \cos^2 \phi \, \Delta k \delta(\epsilon - \epsilon_F) \tag{6.1}$$

with $\Delta k = k_i/N$ the momentum shift per electron, $N = k_F^2 L^2/(4\pi)$ the number of electrons in the Fermi sea, k_F the Fermi momentum, and L^2 the system area. For a system with linear dispersion, the initial current, i.e., the current before any scattering events, is given by $j_i = -e v_F \hat{\boldsymbol{k}}_i/L^2$. The final current given by Eq. (6.1) can thus be written as

$$j_f = \frac{k_i}{k_F} j_i. \tag{6.2}$$

We can see that the final current is larger by a factor of $\epsilon_i/\epsilon_F > 1$ than the initial current carried by the single excited electron, i.e., the current is *amplified* by e-e scattering.

An argument for a quadratic dispersion yields the expected result $j_f = j_i$, i.e., e-e scattering leaves the current unaffected since momentum conservation implies current conservation for a quadratic dispersion. Indeed, this momentum-conservation argument can be extended in a straight-forward way to systems with arbitrary power-law dispersions. For a general dispersion $\epsilon \sim k^n$ the argument yields $j_f = j_i (k_1/k_F)^{2-n}$. For quadratic dispersions with $n = 2$ we recover the expected result $j_f = j_i$, while the current increases for systems with $n < 2$ and decreases for systems with $n > 2$. This general results also shows that higher order corrections to the perfectly linear Dirac dispersion will reduce the current amplification. Hexagonal warping, e.g., is cubic in momentum with $\mathcal{H}_w \sim \lambda k^3 \sigma_z$ for Bi_2Se_3. One can show, however, that in the case of warping, the resulting correction to the current amplification will be small as it is quadratic in the warping

strength λ. We will thus continue to focus on the case of a perfectly linear dispersion in the remainder of this chapter.

So far we have studied the case of $\epsilon_F > 0$ but this argument can also be applied to the case of negative Fermi energy. We again consider a single excited electron with initial energy $\epsilon_i > 0$ as before and assume that the Fermi energy is sufficiently negative so that after relaxation of the initially excited electron the conduction band of the Dirac system is completely empty. As the final carriers are all in the valence band, momentum and velocity of the particles will be antiparallel. Thus the final current is amplified in magnitude as before but actually flows in the direction opposite to the initial current, i.e.,

$$j_f^{(\epsilon_F < 0)} = -\frac{k_i}{k_F} j_i.$$

(6.3)

As we will see below [cf. Eq. (6.26)], this amplification of the current in the direction opposite to the initial current actually appears as a relaxation of the current when considering only a single scattering event.

An analogous argument can be used to study the effect of e-e scattering on the current carried by a single excited hole. Here the picture is just inverted and the hole current is amplified in the direction of the initial current for a Fermi energy below the Dirac point and opposite to the initial current for a Fermi energy above the Dirac point. In combination, this means that for a photoexcited electron-hole pair, the individual electron and hole currents are both amplified in magnitude by e-e scattering. This amplification, however, occurs in opposite directions leading to an overall photocurrent relaxation back to zero.

While this momentum conservation argument provides a simple way to demonstrate the surprising result of a current amplification due to e-e scattering, it actually hides many subtleties that only become apparent when studying the limit of a single scattering event. This is especially true for a photocurrent associated with a photoexcited electron-hole pair. The above argument only shows that the current will ultimately relax back to zero but the details of how this happens are hidden. As we will see below, the photocurrent relaxation is actually governed by a very subtle interplay between the electron and hole contributions and the underlying processes can only be understood when considering the effect of a single scattering process.

Also, even for relatively clean samples and low temperatures, electrons will not exclusively relax by e-e scattering but there will be a combination of e-e scattering with electron-phonon and electron-impurity scattering in the relaxation

momentum conservation $+$ energy conservation

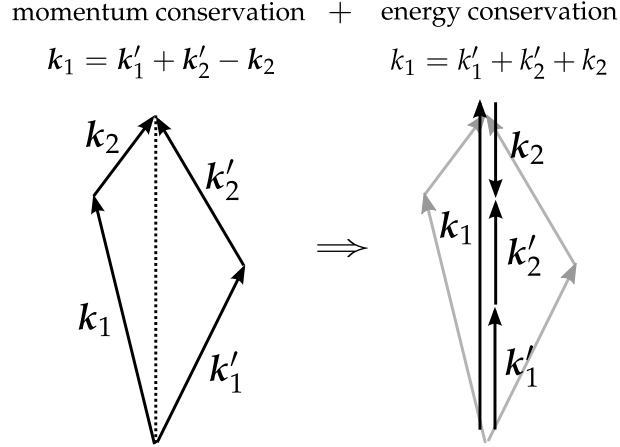$$k_1 = k_1' + k_2' - k_2 \qquad k_1 = k_1' + k_2' + k_2$$

Figure 6.2: The conditions of energy and momentum conservation for a Fermi energy at the Dirac point given by Eqs. (6.6) and (6.7) require that scattering is collinear.

process. Considering the cascade picture of Song et al. [2013] a highly excited electron might first relax by e-e scattering but will eventually also relax through momentum non-conserving processes such as impurity or phonon scattering. The above argument is no longer valid in this regime. Understanding what happens in the single scattering event picture, however, provides a way of estimating the combined effects of various relaxation mechanisms of the current relaxation.

In the next two sections we thus analyze in detail the effect of e-e scattering in the limit of a single scattering event.

6.3 INDIVIDUAL SCATTERING EVENTS

The surprising result that e-e scattering can lead to an increase in the current can also be seen for a single scattering process when analyzing the kinematic constraints, given by energy and momentum conservation,

$$\epsilon_{k_1} + \epsilon_{k_2} = \epsilon_{k_1'} + \epsilon_{k_2'}, \tag{6.4}$$

$$k_1 + k_2 = k_1' + k_2'. \tag{6.5}$$

Here, k_i (k_i') is the momentum of the initial (final) electrons and $\epsilon_k = \pm v_F k$ is the energy for the upper (conduction) and lower (valence) band, respectively. While the form of Eq. (6.5) is independent of the specific scattering process, Eq. (6.4)

expressed in terms of momentum, actually depends on whether the specific scattering process involves particles from the same band or from different band, i.e., whether the process is intraband or interband. Which scattering processes are allowed depends, of course, on the Fermi energy.

For a Fermi energy at the Dirac point, $\epsilon_F = 0$, the excited electron can only relax by scattering off electrons in the Fermi sea which is completely in the valence band. There is only a single kind of scattering process that is allowed as illustrated in Fig. 6.1 (a). The excited electron relaxes by interacting with the Fermi sea, creating a hole in the valence band and an additional electron in the conduction band. Taking into account that the electron in the Fermi sea has a negative energy, i.e, $\epsilon_{k_2} = -v_F k_2$, the condition of energy conservation given by Eq. (6.4) leads to $k_1 - k_2 = k_1' + k_2'$. Written a little differently this becomes together with Eq. (6.5)

$$k_1 = k_1' + k_2' + k_2 \tag{6.6}$$
$$\boldsymbol{k}_1 = \boldsymbol{k}_1' + \boldsymbol{k}_2' - \boldsymbol{k}_2. \tag{6.7}$$

Thus the length of the vector $\boldsymbol{k}_1$ has to be equal to the sum of the lengths of the remaining three vectors $\boldsymbol{k}_2$, $\boldsymbol{k}_1'$, and $\boldsymbol{k}_2'$. This can only be satisfied for collinear scattering, when $\boldsymbol{k}_1$ is parallel to $\boldsymbol{k}_1'$ and $\boldsymbol{k}_2'$ and antiparallel to $\boldsymbol{k}_2$ as illustrated in Fig. 6.2. Thus the initial and final states must have the same velocities, i.e., $v_1 = v_2 = v_1' = v_2'$, considering that velocity and momentum are antiparallel for states in the valence band. If, however, the initial and final velocities of the particles are all the same, the current is unaffected by the scattering event. For a Fermi energy directly at the Dirac point, e-e scattering therefore does not relax current in systems with linear dispersion.

When the Fermi energy lies above the Dirac point, i.e., $\epsilon_F > 0$, there are two kinds of allowed scattering processes. When the excited electron interacts with the Fermi sea, it can either scatter off an electron in the valence band ($-$) or off an electron in the conduction band ($+$) as illustrated in Fig. 6.1 (b). We will denote these processes as $(+, -) \rightarrow (+, +)$ or $(+, +) \rightarrow (+, +)$ respectively. We have seen above in the argument for the case of $\epsilon_F = 0$, that processes where the excited electron interacts with an electron in the valence band, i.e, processes like $(+, -) \rightarrow (+, +)$, are collinear and do not relax current. For a positive Fermi energy we therefore only need to consider intraband processes like $(+, +) \rightarrow (+, +)$ [see Fig. 6.1 (b)]. In this case, the energy conservation condition given by Eq. (6.4) becomes
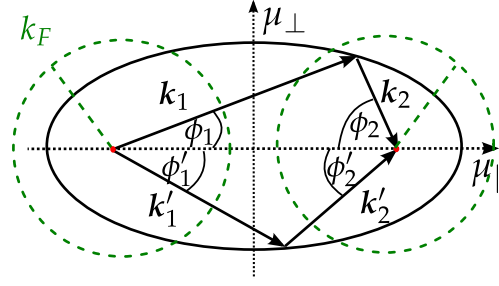
$$k_1 + k_2 = k_1' + k_2'. \tag{6.8}$$

Figure 6.3: Ellipse illustrating the kinematic constraints on the electron scattering process given by energy and momentum conservation for $\epsilon_i > 0$. The momenta k_1 and k_2 are drawn head-to-tail starting and ending at the left and right focal points (red dots). The distance between the focal points is given by $|k_1 + k_2|$ and $(k_1 + k_2)/2$ defines the length of the semi-major axis. When drawn in a similar fashion to k_1 and k_2, the allowed final momenta k_1' and k_2' have to touch at points that lie on the ellipse to ensure energy and momentum conservation. The Fermi momentum is indicated by the green dashed circle. Due to Pauli's principle we have $k_2 \leq k_F < k_2', k_1'$ and the point where k_1 is connected to k_2 lies on the ellipse inside one of the green dashes circle. The point of connection of k_1' and k_2' has to lie outside the green dashed circles on the ellipse.

This condition together with momentum conservation as given by Eq. (6.5) can be graphically interpreted by an ellipse. With the vectors drawn as illustrated in Fig. 6.3, the points of connection of vectors k_1 and k_2 and of vectors k_1' and k_2' that are allowed by momentum and energy conservation describe an ellipse. The semi-major axis is defined by the energy $k_1 + k_2 = k_1' + k_2' = const.$ and $|k_1 + k_2| = |k_1' + k_2'|$ is the distance between the focal points.

In order to show how this construction leads to the results that the current increases along the direction of the initial current $\hat{k}_1$, we will proceed in two steps. In the first step, we assume that k_2 is fixed in addition to k_1. k_1 itself is fixed by the initial condition. Then we have one unique ellipse that is defined by the axes $\hat{\mu}_{\parallel}(k_2)$ and $\hat{\mu}_{\perp}(k_2)$ [see Fig. 6.3]. To evaluate the effect of e-e scattering on the current we have to sum over all possible scattering events. The only variable factors are now k_1' and k_2' with the constraint that the point of connection of k_1' and k_2' has to lie on the ellipse. We will show that a summation over all k_1' and k_2' under this constraint leads to an increase in the current along $\hat{\mu}_{\parallel}$ and a change in current along the perpendicular direction $\hat{\mu}_{\perp}$. In the second step we sum over all allowed k_2, i.e., over all ellipses. Since the only directionality of the problem is given by the initial momentum k_1 the final current also has to flow along the axis defined by k_1. Indeed, the change in current along $\hat{\mu}_{\perp}$ averages
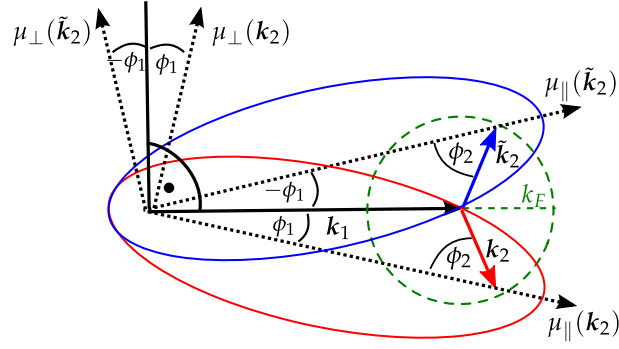
Figure 6.4: Each k_2 parametrizes a different ellipse, i.e., summing over all allowed momenta k_2 means summing over all possible ellipses. The green dashed circle again illustrates the Fermi momentum and the allowed values of k_2 have to lie inside this circle. For any k_2 and corresponding ellipse (blue) there exists a mirror image with respect to the axis defined by k_1, $\tilde{k}_2$ (blue ellipse). The current increase along $\hat{\mu}_{\parallel}$ thus averages to a current increase along k_1. In general there might also be a change of the current along the direction $\hat{\mu}_{\perp}$. As illustrated, the change of the component parallel to k_1 averages to zero when summing over all k_2, and the symmetry of the problem forbids any change of the current perpendicular to k_1. We can thus neglect changes of the current along $\hat{\mu}_{\perp}$.

to zero due to the rotational symmetry when summing over k_2. The increase of the current along the direction $\hat{\mu}_{\parallel}$ averages to an increase of the current along the direction of the initial current $\hat{k}_1$ and we recover the remarkable results of a current amplification discussed before.

Starting now with the first step we assume that k_2 is fixed. The initial and final currents before and after the scattering event along $\hat{\mu}_{\parallel}$ are given by ($v_F = 1$, $e = 1$ for brevity)

$$
\begin{align}
j_i &= (\hat{k}_1)_{\mu_{\parallel}} = \cos \phi_1 \tag{6.9} \\
j_f &= (\hat{k}_1' + \hat{k}_2' - \hat{k}_2)_{\mu_{\parallel}} = \cos \phi_1' + \cos \phi_2' - \cos \phi_2, \tag{6.10}
\end{align}
$$

where the angles are defined as in Fig. 6.3. To analyze how the current changes due to a single e-e scattering event we have to compare $\cos \phi_1 + \cos \phi_2$ to $\cos \phi_1' + \cos \phi_2'$. If $\cos \phi_1 + \cos \phi_2 < \cos \phi_1' + \cos \phi_2'$, the current would decrease while for $\cos \phi_1 + \cos \phi_2 > \cos \phi_1' + \cos \phi_2'$, the current would increase. Using the law of cosine we can write

$$
\cos \phi_1 + \cos \phi_2 = \frac{2a}{e} \left(1 - \frac{a^2 - e^2}{2ak_1 - k_1^2} \right), \tag{6.11}
$$

where $e = |\boldsymbol{k}_1 + \boldsymbol{k}_2|/2 = const.$ is the linear eccentricity of the ellipse and $a = (k_1 + k_2)/2 = const.$ the semi-major axis. One can easily verify that the expression given by Eq. (6.11) has a maximum for $k_1 = a$ and falls off monotonically away from $k_1 = a$. Thus $\cos\phi_1 + \cos\phi_2$ has a maximum for the symmetric case where $k_1 = k_2 = a$ and the point of connection of $\boldsymbol{k}_1$ and $\boldsymbol{k}_2$ lies on the axis $\hat{\mu}_\perp$. From Pauli's principle we know that $k_2 \leq k_F < k'_1, k'_2$. This requires that the point of connection of $\boldsymbol{k}_1$ and $\boldsymbol{k}_2$ has to lie inside the green dashed circle describing k_F as illustrated in Fig. 6.3. As $k'_1, k'_2 > k_F$ the point of connection of $\boldsymbol{k}'_1$ and $\boldsymbol{k}'_2$ has to lie outside the green dashed circle. Then necessarily the point of connection of $\boldsymbol{k}'_1$ and $\boldsymbol{k}_2$ is closer to the $\hat{\mu}_\perp$-axis than the point of connection of $\boldsymbol{k}_1$ and $\boldsymbol{k}_2$ leading to $j_\mathrm{f} \geq j_\mathrm{i}$ for any scattering event. The current increases along the direction given by $\hat{\mu}_\parallel$.

Now we proceed with the second step and sum over all possible $\boldsymbol{k}_2$. This means that we have to sum over all ellipses, i.e., over all possible $\hat{\mu}_\parallel$ and $\hat{\mu}_\perp$. For any given $\boldsymbol{k}_2$ there will also be a $\tilde{\boldsymbol{k}}_2$ which is the mirror image of $\boldsymbol{k}_2$ with respect to the axis defined by $\boldsymbol{k}_1$ as illustrated in Fig. 6.4. Thus for any $\hat{\mu}_\parallel(\boldsymbol{k}_2)$ we also have a $\hat{\mu}_\parallel(\tilde{\boldsymbol{k}}_2)$. We can now easily see that the current increase along $\hat{\mu}_\parallel$ discussed in the first step, averages to a current increase in the direction of $\boldsymbol{k}_1$ when summing over all possible $\boldsymbol{k}_2$. So far we have neglected the component of the current along $\hat{\mu}_\perp$ for a fixed $\boldsymbol{k}_2$ but we can easily see that this omission was justified. This contribution to the current has components parallel and perpendicular to $\boldsymbol{k}_1$. When summing over $\boldsymbol{k}_2$ the component parallel to $\boldsymbol{k}_1$ averages to zero as illustrated in Fig. 6.4 while the perpendicular component also vanishes since the symmetry of the problem requires that the final current has to flow along the axis defined by $\boldsymbol{k}_1$. Thus, we have shown by simple geometric considerations that e-e scattering increases the current carried by a single excited electron when the Fermi level lies above the Dirac point. A analogous argument showing that the current decreases for a Fermi level below the Dirac point, i.e., for $\epsilon_F < 0$, is given in App. D.1. Note, however, that what might look like a current relaxation for a single scattering event for $\epsilon_F < 0$ actually results - in the limit of many scattering events - in an increase in the current albeit in the direction opposite to the initial current.

6.4 QUANTITATIVE ANALYSIS FOR A SINGLE SCATTERING EVENT

Having established how e-e scattering qualitatively affects individual electron and hole currents, we would now like to obtain quantitative estimates of the

change in current and determine the combined effect of electron and hole when considering photocurrents. The rate of change of the current can be obtained within an approach based on Fermi's golden rule. Specifically we consider the surface states of the TI Bi_2Se_3, which are described by the second quantized Dirac Hamiltonian

$$H = \sum_k \Psi_k^\dagger \mathcal{H}_k \Psi_k + \frac{1}{2} \sum_{q,k_1,k_2} \Psi_{k_1+q}^\dagger \Psi_{k_2-q}^\dagger V(q) \Psi_{k_2} \Psi_{k_1}, \tag{6.12}$$

where $V(q) = e^2/2\varepsilon_0\varepsilon q$ is the Coulomb interaction with dielectric constants ε_0 and ε, and

$$\mathcal{H}_k = v_F(k_y\sigma_x - k_x\sigma_y) \tag{6.13}$$

describes the single-particle Dirac dispersion with eigenenergies $\epsilon_k = \pm v_F k$ and eigenstates $|k_i\rangle$.

The rate of change of a current can in general be written as

$$\frac{dj}{dt} = -e \sum_{k_1} v_{k_1} \frac{df_{k_1}}{dt}. \tag{6.14}$$

where f denotes the distribution function. In the absence of external fields, the rate of change of the distribution function is given by the collision integral according to the Boltzmann equation and we can write

$$\frac{df_{k_1}}{dt} = \sum_{k_2,k_1',k_2'} W_{k_1,k_2;k_1',k_2'} \left[f_{k_1'} f_{k_2'} (1 - f_{k_1})(1 - f_{k_2}) - f_{k_1} f_{k_2}(1 - f_{k_1'})(1 - f_{k_2'}) \right]. \tag{6.15}$$

Assuming that we initially have a single photoexcited electron-hole pair with fixed momentum k_1 [see Fig. 6.1 (a)], Eq. (6.14) simplifies to

$$\frac{dj^{(e/h)}}{dt} = \mp e v_{k_1} \frac{df_{k_1}^{(e/h)}}{dt} \tag{6.16}$$

for the individual electron and hole currents. Considering in addition that the transition rate given by Eq. (6.15) is symmetric when interchanging either the initial or final particles, the rate of change of the individual electron and hole currents can be written as

$$\frac{dj^{(e/h)}}{dt} = \mp e \sum_{k_2,k_1',k_2'} (v_1' + v_2' - v_1 - v_2) W_{k_1,k_2;k_1',k_2'}$$
$$\times f^{(e/h)}(\epsilon_{k_2})[1 - f^{(e/h)}(\epsilon_{k_1'})][1 - f^{(e/h)}(\epsilon_{k_2'})], \tag{6.17}$$

where the velocity is $v_i = v_F \text{sgn}(\epsilon_{k_i}) \hat{k}_i$ and $f^{(e/h)}(\epsilon_{k_i})$ denotes the Fermi distribution function of electrons and holes, respectively. The transition rate is given by

$$W_{k_1,k_2;k'_1,k'_2} = \frac{2\pi}{\hbar}|M|^2 \delta_{k_1+k_2,k'_1+k'_2} \delta(\epsilon_1 + \epsilon_2 - \epsilon'_1 - \epsilon'_2), \qquad (6.18)$$

with $\epsilon_i = \epsilon_{k_i}$ and interaction matrix element

$$M = \frac{1}{2L^2}[\langle k'_1|k_1\rangle\langle k'_2|k_2\rangle u(|k_1 - k'_1|) - (k'_1 \leftrightarrow k'_2)]. \qquad (6.19)$$

Here, L^2 is the surface area of the system and $u(q) = (e^2/2\varepsilon_0\varepsilon)/(q + q_{\text{TF}})$ the screened Coulomb interaction where $q_{\text{TF}} = \alpha k_F$ is the Thomas-Fermi wave vector with $\alpha = e^2/(4\pi\hbar v_F\varepsilon_0\varepsilon)$. As photoexcitation creates highly excited electron-hole pairs, the corrections to the Fermi distribution due to finite temperature become negligible and we can set $T = 0$.

In order to proceed we need to evaluate Eq. (6.17). At $T = 0$ the distribution functions become Heaviside θ-functions and the integrand can be simplified by introducing the momentum transfer $q = k_1 - k'_1 = k'_2 - k_2$. Using the identity

$$\delta(\epsilon_1 + \epsilon_2 - \epsilon'_1 - \epsilon'_2) = \int d\omega \delta(\epsilon_1 - \epsilon'_1 - \omega)\delta(\epsilon'_2 - \epsilon_2 - \omega) \qquad (6.20)$$

the two δ-functions can be used to eliminate two angular integrals (see App. D.2). This leaves us with a three-dimensional integral which can be solved numerically for general parameters and analytically in limiting cases such as large excitation energies, i.e., $\epsilon_1/\epsilon_F \ll 1$.

Before studying in detail the rate of change of the current given by Eq. (6.17) we want to estimate how much the current is changed by a single scattering event. Specifically we determine the mean change of current per scattering event for a single excited electron as illustrated in Fig. 6.5. The inset shows schematically how an e-e collision changes the current. The mean change in current is defined by

$$\frac{\langle \Delta j \rangle}{j_0} = \frac{1}{j_0 \Gamma}\frac{dj}{dt}, \qquad (6.21)$$

where Γ is the total scattering rate and j_0 the initial current carried by the excited electron. To make our results more realistic we include particle-hole asymmetry to the dispersion through $\epsilon_k = \pm v_F k + \xi k^2$. The total scattering rate Γ actually diverges for a perfectly linear dispersion since the phase space for collinear scattering becomes infinite. The physical particle-hole asymmetry regularizes this
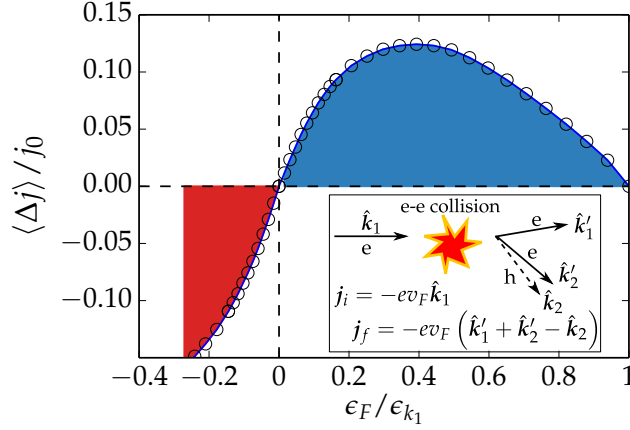
Figure 6.5: Mean change of the current per electron scattering event relative to the initial current j_0, $\langle \Delta j \rangle / j_0$, as a function of Fermi energy ϵ_F for fixed initial energy $\epsilon_{k_1} \approx 0.15$ eV. Regions of current amplification and relaxation are illustrated by the blue and red shaded areas, respectively. The rate of change of the current is normalized by the total scattering rate Γ [see Eq. (6.21)]. To obtain these results we used realistic parameters for Bi_2Se_3, including particle-hole asymmetry $\xi = 23.7$ eV Å^2, $v_F = 5 \cdot 10^5$ m/s [Liu et al., 2010], and $\alpha = 0.1$ (see text for definitions) where we assumed an average dielectric constant of air and Bi_2Se_3 of $\varepsilon \sim 50$ [Greenaway and Harbeke, 1965; Sandomirsky et al., 2001]. The inset shows a schematic scattering process where the initially excited electron excites an electron-hole pair, and the corresponding initial and final currents.

divergence. Since collinear scattering does not affect the current as we have seen above, the rate of change dj/dt would remain well defined even for a linear dispersion. There are also other ways to regularize Γ. For a perfectly linear dispersion the regularization can be done by dynamical screening within the random phase approximation [Song et al., 2013; Tomadin et al., 2013]. Note that when calculating the total scattering rate Γ one has to take into account all allowed scattering processes including processes that do not change the current.

As illustrated in Fig. 6.5, we qualitatively recover the results we obtained by analyzing the kinematic constraints. A single e-e collision decreases the current for negative Fermi energy and increases the current for positive energy. For zero energy the current remains unaffected by e-e scattering. For $\epsilon_F/\epsilon_1 \to 1$, the phase space for scattering vanishes and the change in current goes to zero. Quantitatively, we used an initial excitation energy of $\epsilon_1 \approx 0.15$ eV, particle-hole asymmetry $\xi = 23.7$ eV Å^2, and $v_F = 5 \cdot 10^5$ m/s [Liu et al., 2010]. For the Thomas-Fermi wave vector $q_{TF} = \alpha k_F$ we used $\alpha = 0.1$ where we assumed an

average dielectric constant of air and Bi_2Se_3 of $\varepsilon \sim 50$ [Greenaway and Harbeke, 1965; Sandomirsky et al., 2001]. With these parameters we find that the maximal current enhancement can be of the order of $\sim 10\%$ per scattering event.

We now study in detail the rate of change of the current given by Eq. (6.17). From now on we assume a perfectly linear dispersion, i.e., $\xi = 0$, because dj/dt is well behaved in that limit as explained above. We also choose $\epsilon_F > 0$ for definiteness, the case of negative Fermi energy follows by electron-hole symmetry. Numerical integration of Eq. (6.17) gives the rates of change of the individual electron and hole current and in combination also of the total current. The results are illustrated in Fig. 6.6 where the red squares describe the electron current, the green diamonds the hole current and the blue circles the total current. As we know by now, e-e scattering increases the electron current for a positive Fermi energy and decreases the hole current. For large Fermi energies $\epsilon_F/\epsilon_1 \rightarrow 1$ the electron current goes to zero while the hole current remains finite. The reason is the difference in the available phase space for scattering for the individual carriers. Fig. 6.1 (b) and (c) show the relevant scattering processes for electron and hole. For $\epsilon_F/\epsilon_1 \rightarrow 1$ the phase space for scattering of the electron clearly vanishes [Fig. 6.1 (b)], the phase space for scattering of the hole remains finite [Fig. 6.1 (c)]. Adding the two individual contributions, we see that the total current (blue circles) also relaxes by e-e scattering but also that there are significant cancellations between the electron and hole currents. The total current relaxes much slower. To understand and quantify this cancellation effect we study the asymptotic behavior of Eq. (6.17) in the limit of $\epsilon_F/\epsilon_1 \ll 1$ analytically.

We can neglect any collinear processes since those do not change the current as shown above. Remembering that we chose $\epsilon_F > 0$, for the electron current we thus only need to consider scattering processes within the conduction band, i.e., $(+, +) \rightarrow (+, +)$, as the one illustrated in Fig. 6.1 (b). For the hole there are two possible processes that can change the current. The hole can recombine with an electron from the valence band, thereby exciting an electron from the conduction band to above the Femi level, i.e, $(-, +) \rightarrow (-, +)$, as illustrated in Fig. 6.1 (c). In the other process, the hole can recombine with an electron in the conduction band, exciting an electron from the valence band to above the Fermi level, i.e., $(-, +) \rightarrow (+, -)$ [consider $k_1' \leftrightarrow k_2'$ in Fig. 6.1 (c)]. Other processes will be collinear and can be neglected.
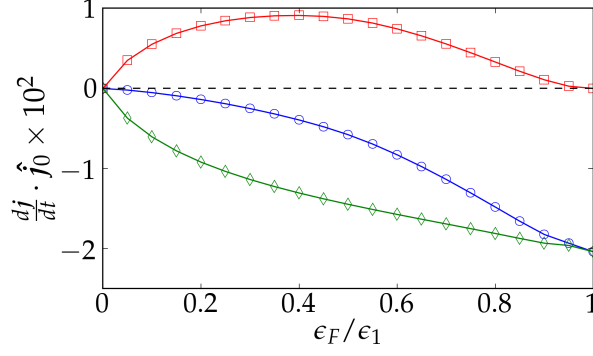
Figure 6.6: Rates of change of the electron (red squares), hole (green diamonds), and total (blue circles) currents obtained from Eqs. (6.22) and (6.23) and their sum. We used the same parameters as in Fig. 6.5 without electron-hole asymmetry. The relaxation of the total current (blue circles) is strongly suppressed due to cancellations between the electron and hole contributions. The results for $\epsilon_F < 0$ follow by electron-hole symmetry.

The rate of change of the electron and hole current according to Eq. (6.17) become

$$\frac{dj^e}{dt} = -e \frac{1}{4L^4} \frac{2\pi}{\hbar} \left(\frac{e^2}{2\epsilon_0 \epsilon}\right)^2 \sum_{k_2,k_2',k_1'} \delta(\epsilon_{k_1} + \epsilon_{k_2} - \epsilon_{k_1'} - \epsilon_{k_2'}) \left(\hat{k}_1' + \hat{k}_2' - \hat{k}_1 - \hat{k}_2\right)$$

$$\times \left| \frac{\langle k_1,+|k_1',+\rangle \langle k_2,+|k_2',+\rangle}{|k_1 - k_1'| + q_{TF}} - \frac{\langle k_1,+|k_2',+\rangle \langle k_2,+|k_1',+\rangle}{|k_1 - k_2'| + q_{TF}} \right|^2$$

$$\times \theta(\epsilon_F - \epsilon_{k_2})\theta(\epsilon_{k_2'} - \epsilon_F)\theta(\epsilon_{k_1'} - \epsilon_F) \tag{6.22}$$

and

$$\frac{dj^h}{dt} = 2e \frac{1}{4L^4} \frac{2\pi}{\hbar} \left(\frac{e^2}{2\epsilon_0 \epsilon}\right)^2 \sum_{k_2,k_2',k_1'} \delta(\epsilon_{k_1} + \epsilon_{k_2} - \epsilon_{k_1'} - \epsilon_{k_2'}) \left(-\hat{k}_1' + \hat{k}_2' + \hat{k}_1 - \hat{k}_2\right)$$

$$\times \left| \frac{\langle k_1,-|k_1',-\rangle \langle k_2,+|k_2',+\rangle}{|k_1 - k_1'| + q_{TF}} - \frac{\langle k_1,-|k_2',+\rangle \langle k_2,+|k_1',-\rangle}{|k_1 - k_2'| + q_{TF}} \right|^2$$

$$\times \theta(\epsilon_{k_2} - \epsilon_F)\theta(\epsilon_F - \epsilon_{k_2'}), \tag{6.23}$$

where $|k,\pm\rangle$ describes a state in the conduction or valence band respectively. For the hole current the sums are restricted to $\epsilon_{k_1'} < 0$ and $\epsilon_{k_2'} > 0$ and the additional factor of 2 accounts for the case $\epsilon_{k_1'} > 0$ and $\epsilon_{k_2'} < 0$. To simplify the calculation we introduce the momentum transfer $q = k_1 - k_1' = k_2' - k_2$. To leading order, the rates of change of the electron and hole currents, will be dominated by

scattering events with small momentum transfer $q \ll k_1$, because the Coulomb interaction scales as $\sim 1/(q + q_{\mathrm{TF}})$. With this we can, e.g, approximate

$$\hat{k}_1' - \hat{k}_1 = \frac{k_1 - q \cos \phi_q}{|\mathbf{k}_1 - \mathbf{q}|} - 1 \approx 0. \tag{6.24}$$

and

$$|\langle \mathbf{k}_1 | \mathbf{k}_1' \rangle|^2 = \frac{k_1 - q \cos \phi_q + |\mathbf{k}_1 - \mathbf{q}|}{2|\mathbf{k}_1 - \mathbf{q}|} \approx 1. \tag{6.25}$$

With the help of the identity (6.20), Eqs. (6.22) and (6.23) can now be evaluated analytically for $k_F \ll k_1$. The details of the calculation can be found in App. D.4. We find that the asymptotic behavior of the rate of change of the electron and hole currents is given by

$$\frac{d\mathbf{j}^{(e/h)}}{dt} \approx \pm C \alpha^2 \frac{\epsilon_F}{\hbar} \mathbf{j_0}, \tag{6.26}$$

where $C \approx 0.3$ (see App. D.4), $\pm$ stands for the electron and hole current respectively, and $\mathbf{j_0}$ is the initial current of magnitude $j_0 = e v_F$ of the photoexcited carrier.

This results has several interesting aspects. First, we see that the rate of change of the individual electron and hole currents is actually independent of the excitation energy ϵ_1 even though we are considering the limit of large $\epsilon_1 / \epsilon_F \gg 1$. The reason is that Eq. (6.26) is solely determined by e-e scattering events with small energy transfer of the order of $\sim \epsilon_F$ independent of the excitation energy [see Figs. 6.1 (b) and (c)]. Secondly, to this order the rates of change of the electron and hole currents only differ in their signs. Thus, this leading order exactly cancels when considering the rate of change of the current associated with a photoexcited electron-hole pair. In agreement with our numerical analysis [see. Fig. 6.6] we indeed find that the rate of change of the total current of a photoexcited electron-hole pair is smaller than the individual contributions and must scale with a higher power of ϵ_F / ϵ_1. Calculating Eqs. (6.22) and (6.23) as outlined above to higher order (see App. D.4), we find that

$$\frac{d\mathbf{j}^{(\mathrm{tot})}}{dt} = \frac{d\mathbf{j}^{(e)}}{dt} + \frac{d\mathbf{j}^{(h)}}{dt} \approx -\frac{\alpha^2}{9} \frac{\epsilon_F}{\hbar} \left(\frac{\epsilon_F}{\epsilon_1} \right)^{1/2} \mathbf{j_0}. \tag{6.27}$$

In contrast to Eq. (6.26), we see that the rate of change of the total current depends on the large excitation energy ϵ_1 and even vanishes in the limit $\epsilon_1 \to \infty$. For small ϵ_F / ϵ_1 the relaxation of the total current is suppressed. Fig. 6.7 (a) shows the asymptotic behavior of the rate of change of the total current given by Eq. (6.27) (red solid line) and the result determined by numerically integrating Eq. (6.17) (blue circles),
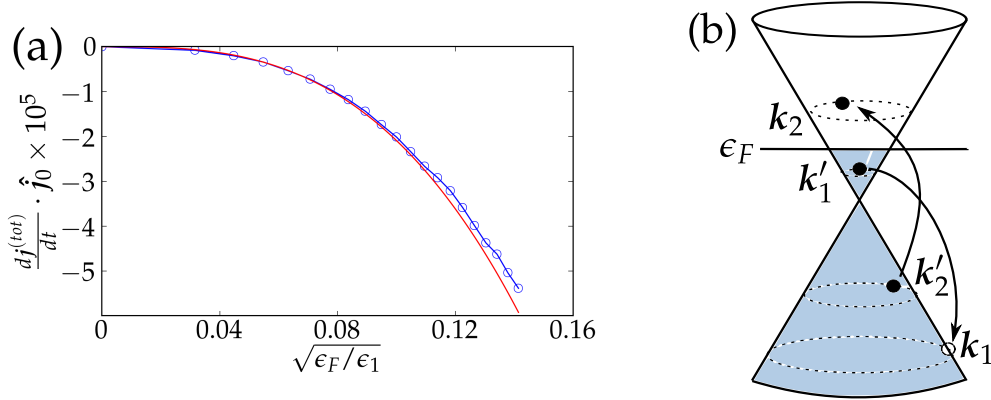
Figure 6.7: (a) Rate of change of the total current (blue circles) [from Eq. (6.17)] and the asymptotic behavior $\sim (\epsilon_F/\epsilon_1)^{3/2}$ given by Eq. (6.27) (red). (b) To leading order the relaxation of the total current current is governed by the illustrated scattering process of the excited hole. These scattering processes involve a large energy transfer explaining the observed suppression of the relaxation rate.

The distinctly different relaxation behaviors of the total current and the individual electron and hole currents are rooted in the underlying scattering processes. The amplification and relaxation of the electron and hole current respectively are dominated by scattering processes with small momentum transfer, and thus small energy transfer, of the order of the Fermi energy. This is not a surprising result as Coulomb interaction is inversely proportional to the momentum transfer and will thus be dominant for small momentum transfer. For energy relaxation of excited electrons in Dirac systems, it was found that the electron relaxation occurs through a cascade of scattering processes losing in each step an energy of the order of ϵ_F [Song et al., 2013].

For the relaxation of the total current the picture drastically changes. In the limit $\epsilon_1/\epsilon_F \gg 1$ the contributions from scattering with small energy transfer of the individual electron and hole currents cancel exactly to the order considered. The relaxation of the total current given by Eq. (6.27) is solely governed by scattering processes with large energy transfer of the order of ϵ_1. In addition scattering processes of the excited electron actually only have a subleading effect. To leading order, the relaxation of the total current is caused by scattering of the photoexcited hole, specifically the scattering processes $(-,+) \rightarrow (+,-)$ illustrated in Fig. 6.7 (b). Here the photoexcited hole recombines with an electron from the valence band, thereby exciting an electron from the conduction band to above the Fermi sea. This collision involves a large energy transfer of the order of ϵ_1

which also explains why the relaxation of the total current vanishes in the limit of $\epsilon_1 \to \infty$.

6.5 EXPERIMENTAL SIGNATURES OF THE AMPLIFICATION EFFECT

Naturally the amplification effect has important implications for photocurrent measurements. Photocurrents are carried by electron-hole pairs and the amplification effect for the electron current results in the strong suppression of the rate of change of the photocurrents due to e-e scattering [see Eq. (6.27)], which is indeed interesting for time-resolved photocurrent measurements.

One might also want search for a way to directly observe the amplification effect for a single excited electron, which could, however, prove difficult. First, one needs to inject electrons of a certain energy and momentum into a Dirac system. One possible way to achieve this is to let electrons tunnel from a nanotube to graphene such that momentum is conserved. Here, an advantage of graphene over 3D TIs is that the 2D nature of graphene protects us from any unwanted bulk contributions which are often present in 3D TIs [Taskin and Ando, 2009; Checkelsky et al., 2009; Peng et al., 2010; Analytis et al., 2010]. In addition graphene can be made remarkably clean reducing the disturbing effect of impurities.

Consider the setup illustrated in Fig. 6.8 (a), where an array of nanotubes is placed above a graphene sheet such that the nanotubes are parallel to the direction between the K and K' points of graphene, i.e., parallel to a zigzag edge. The graphene sheet and the nanotube array can be gated independently and a bias applied between them such that in momentum space we will have two Dirac cones (one 1D and one 2D) which are shifted in energy as illustrated in Fig. 6.8 (b). In order to measure the amplification effect the graphene sheet has to be gated to a small positive Fermi energy. We will apply an additional source-drain voltage to the nanotube array that will give us a different chemical potential for right and left movers inside the nanotubes. The idea is that the gate and source-drain voltages applied to the nanotubes are adjusted such that, e.g., only left moving states in the nanotubes are occupied in the region where they overlap with states in the graphene sheet, i.e., where momentum conserving tunneling is allowed, indicated by red color in Fig. 6.8 (b). The corresponding right moving states are unoccupied, so only left movers can tunnel into graphene. Of course this implies that the nanotubes are short enough that there is no equi-

libration between left and right movers. It has been shown that in certain 1D systems, equilibration between left and right movers can be remarkably slow [Karzig et al., 2010]. The tunneling electrons conserve their energy and momentum along the nanotubes (e.g. the x-direction), i.e., electrons with energies in the interval $[\epsilon_c, \epsilon_c + \mu_L]$ can tunnel into graphene. Electrons with energy $> \epsilon_c$ will acquire a finite k_y-component to satisfy energy conservation. Because of symmetry the final current injected into the graphene sheet, of course, flows along the direction of the nanotubes.

Even in this straightforward setup, measuring the amplification of the current turns out to be quite subtle. The advantage of the given setup is, that by measuring the tunneling current one also directly determines the current that flows in the graphene sheet before any scattering events occur. This is, however, not the current one measures. The measurable quantity is the final current after e-e relaxation [see Eq. (6.1)]. This final current is the same for linear, $\epsilon = v_F k$, or quadratic, $\epsilon = k^2/(2m)$, dispersion under the substitution $v_F = k_F/m$. The two dispersions only differ in the way this final current develops after the injection of the initial current. For a quadratic dispersion the final current is obtained immediately after injection and e-e scattering does not affect the current. For a linear dispersion, however, the final current consists of a contribution that exists immediately after injection and the subsequent increase of this current (for $\epsilon_F > 0$) due to partial energy relaxation by e-e scattering. The current only assumes its final value in two steps, namely tunneling and subsequent carrier relaxation, with possibly very different time scales. Thus comparing the tunneling current to the measured current in graphene should reveal the differences in the two dispersions and show the amplification effect for linear dispersion, when one neglects any resistance or scattering effects due to the leads.

In addition to exploring the amplification effect by comparison with the initially injected current, the proposed setup results in a current whose magnitude can be controlled by tuning the bias and gate voltages applied to graphene. When varying the chemical potential in graphene within the conduction band, a sample with a quadratic dispersion would lead to a gate-independent current. Tuning the gate voltage of graphene we can not only control the magnitude of the final current but also its sign. While for a Fermi energy in the conduction band the final current is flowing in the same direction as the initially injected current, for a Fermi energy in the valence band (and fixed initial energy) e-e scattering leads to a reversal of the direction of the current in addition to the amplification [see Sec. 6.2]. Thus the ratio of injected to final measured current should change sign

when the Fermi energy crosses the Dirac point. This is a distinct signature as no equivalent effect exists for a quadratic dispersion.

Another even more direct signature of the proposed amplification effect might be obtained by a time-resolved measurement. Taking into account that electrons might be injected into the graphene sheet by a pulse that is short compared to the time scale for relaxation, a time-resolved measurement might reveal how the current is amplified over time. The necessary femtosecond time-resolution has already been demonstrated in experiments on graphene [Breusing et al., 2011; Sun et al., 2012; Brida et al., 2013].

Quantitatively, in order to compare a measured final current to the initially injected current, we need to determine this initial current. An advantage of the proposed setup is that we can theoretically determine the current flowing in the graphene sheet immediately after injection. To calculate the initial current, we first consider a small positive Fermi energy $\epsilon_F > 0$ inside graphene and assume that the Fermi velocity v_F is the same for nanotubes and graphene. A single electron of energy $\epsilon_i = 2\epsilon_c - v_F k_i$ and momentum $\mathbf{k}_i = k_i \hat{\mathbf{k}}_x$ in a nanotube with $\epsilon_c < \epsilon_i < \mu_L$ can tunnel into graphene [cf. Fig. 6.8 (b)]. Conservation of energy and momentum along the nanotubes require that electrons with $\epsilon_i > \epsilon_c$ acquire a finite k_y-component with $k_y = \pm[(2\epsilon_c/v_F)^2 - 4\epsilon_c k_i/v_F]^{1/2}$ when tunneling into graphene with equal probability for $\pm|k_y|$. The initial current in graphene is then the average of the currents produced by two particles at $\mathbf{k}_\pm = (k_i, \pm|k_y|)$, i.e.,

$$j_i = -\frac{ev_F}{A}\frac{\hat{\mathbf{k}}_+ + \hat{\mathbf{k}}_-}{2} = -\frac{ev_F}{A}\frac{v_F k_i}{\epsilon_i}\hat{\mathbf{k}}_x. \tag{6.28}$$

Of course, there will be more than just a single electron tunneling from the nanotubes into graphene. We can define a tunneling current $j_T = ev_F N_T \hat{\mathbf{k}}_x/A$, where N_T is the number of tunneling electrons and A the area of the graphene sheet, which can be measured experimentally. Assuming electrons within the energy interval $[\epsilon_c, \epsilon_c + \mu_L]$ tunnel with equal probability, the initial current inside graphene is given by

$$j_i = -\frac{v_F \langle k_i \rangle}{\langle \epsilon_i \rangle} j_T, \tag{6.29}$$

where $\langle k_i \rangle = (3\epsilon_c - \mu_L)/(2v_F)$ and $\langle \epsilon_i \rangle = 2\epsilon_c - v_F\langle k_i \rangle$ are the average momentum and energy of the tunneling electrons. This expression simplifies in the limit $\mu_L \to \epsilon_c$ to $j_i = -j_T$. The current flowing from the nanotube onto the graphene sheet is in total transformed into a current in graphene which moves in the opposite direction but is of the same magnitude. In general this is not true since
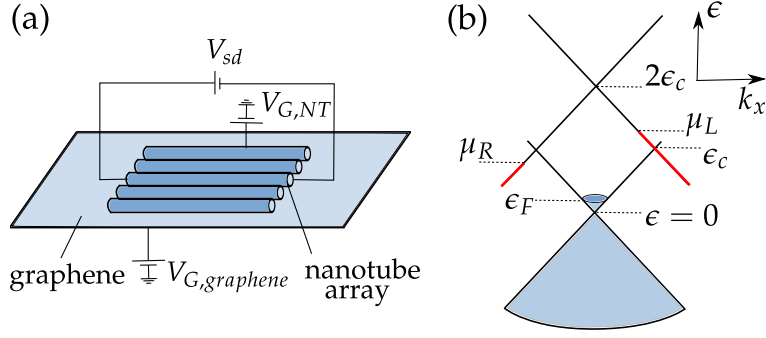
Figure 6.8: (a) Schematic illustration of the proposed experimental setup with a nanotube array on top of a graphene sheet. The effect in principle would also work for a single nanotube but using an array instead might be advantageous in terms of gating. The nanotube array and the graphene sheet will be gated independently with $V_{G,graphene}$ and $V_{G,NT}$ respectively, such that we have two shifted Dirac cones in momentum space as illustrated in (b). A bias between right and left movers in the nanotubes is induced by the source-drain voltage V_{sd}. (b) Two shifted Dirac cones for the graphene sheet (bottom cone, 2D) and for the nanotubes (top cone, 1D), assuming that graphene and the nanotubes have the same Fermi velocity. Since we only want to have, e.g., left moving electrons tunneling into graphene, the gate and source-drain voltages have to be adjusted such that $\mu_L > \epsilon_c > \mu_R$. Occupied states in the nanotubes are indicated by red color.

tunneling does not necessarily result in electrons that all move in the same direction as for this limiting case. For a linear dispersion, the final measured current is then amplified with respect to the initial current,

$$j_f = \frac{\langle \epsilon_i \rangle}{\epsilon_F} j_i. \tag{6.30}$$

So far we assumed that in the proposed experiment relaxation only occurs through e-e scattering. Generally this might not be true and competing relaxation processes such as electron-phonon or impurity scattering might contribute. We note that our calculation of the current increase per e-e scattering event (see Fig. 6.5) can be used to estimate the final current produced in a tunneling experiment when e-e scattering competes with other relaxation processes. Specifically, e-e collisions relax a highly excited electron via a cascade of scattering processes in each of which the electron loses an energy of the order of ϵ_F [Song et al., 2013]. The mean change of the current per scattering event as a function of Fermi energy illustrated in Fig. 6.5 describes the current increase (or decrease for negative Fermi energy) for each of these scattering steps. If in a tunneling ex-

periment as described above, the excited electron now relaxes not only through e-e scattering but also through phonon or impurity scattering one can estimate the current as follows. If the non-Coulomb relaxation processes do not allow full relaxation through e-e scattering but only allow $N < \epsilon_1/\epsilon_F$ e-e scattering events, then the measured current amplification would be proportional to the sum of the amplification curve for electrons in Fig. 6.5 at values $\epsilon_F/\epsilon = \epsilon_F/(\epsilon_1 - n\epsilon_F)$ for $0 \leq n < N$.

6.6 SUMMARY

We performed a detailed analysis of the relaxation dynamics of photocurrents in clean Dirac systems and uncovered surprising results. An excited electron-hole pair associated with the photocurrent exhibits strongly asymmetric behavior of the individual carriers. For a Fermi energy above the Dirac point, a single e-e scattering event actually increases the 'electron current', while the 'hole current' decreases. The behavior is reversed for negative Fermi energy. The current is unaffected by e-e scattering for a Fermi energy directly at the Dirac point. The highly asymmetric contributions of electron and hole partially cancel when studying their combined effect, leading to a strong suppression of the relaxation of the total photocurrent.

This suppression of photocurrent relaxation is rooted in the underlying scattering processes which reveal that there are distinct differences in the mechanisms for energy and current relaxation. Energy relaxation of excited particles in Dirac systems for positive Fermi energy is predicted to be dominated by scattering events with small energy transfer. The relaxation then occurs through a cascade of scattering events in each of which the excited particle loses a small energy of the order of the Fermi energy [Song et al., 2013]. For a single excited electron or hole, current relaxation is also dominated by scattering events with small energy transfer of the order of the Fermi energy, similar to the case of energy relaxation. For a photocurrent consisting of an excited electron-hole pair, however, the contributions governed by scattering events with small energy transfer cancel to leading order. The relaxation of the photocurrent is thus actually dominated by scattering events with large energy transfer of the order of the initial excitation energy which is quite different from the energy relaxation picture. Analyzing the relaxation process in detail, we find that the initial relaxation rate of the photocurrent scales as $\sim \epsilon_F^{3/2}$. The amplification or relaxation of the individual electron or hole currents on the other hand scales as $\sim \epsilon_F$.

While we argued that e-e scattering provides the dominant relaxation mechanism, there will be additional non-Coulomb mechanisms that become important when studying the complete energy relaxation. Combing our results of the change in current per e-e scattering event with the energy relaxation cascade-picture [Song et al., 2013], our analysis also provides a way to estimate the photocurrent response when such non-Coulomb relaxation mechanisms are present.

Our calculation of the mean change in current per scattering event also shows that the surprising increase in the electron current by a single collision for positive Fermi energy is quite substantial for realistic parameters. Once the excited electron has fully relaxed, i.e., once partial equilibrium is reached, after many scattering events, the current is even amplified by a factor of ϵ_1/ϵ_F when other relaxation mechanisms are neglected. The amplification will, of course, be reduced when additional non-Coulomb processes, like electron-phonon or impurity scattering become important. A large density of excited electrons and phonons due to a high radiation intensity will also lead to a reduction of the effect [Winzer and Malic, 2012; Song et al., 2013; Song, 2014]. The amplification effect should thus be strongest when the excited electrons have an energy below the optical phonon frequencies (≈ 200 meV for graphene) and when low-intensity radiation is used.

Our results provide important insights into the relaxation dynamics of photocurrents and we also discuss how the amplification effect might be measured in experiment. We find that a direct observation of this effect in graphene requires ultrafast femtosecond time-resolution which has already been achieved in optical measurements [Breusing et al., 2011; Sun et al., 2012; Brida et al., 2013]. In addition we propose an experimental setup where the amplification effect can be observed by comparing the final measured current after relaxation of carriers to the theoretically calculated initial current. This setup could also probe the Fermi energy dependence of the effect, i.e, the change in sign when the Fermi energy crosses the Dirac point, by varying the applied gate voltage. There might also be other ways to observe the amplification effect. Since highly excited electrons lead to an increase in the current, the photoconductivity, i.e., the electron conductivity in the presence of light, might also be enhanced. Increasing the energy $\hbar\omega$ of the irradiating light should increase the enhancement of the photocurrent. Again, due to the strong increase in current a strong non-linear signature in the IV characteristics might also be expected. Other types of systems might also be promising candidates for studying the amplification effect as, e.g., cold atom systems allow one to tune the interactions.

7

CONCLUSIONS AND OUTLOOK

In this thesis we presented a theoretical study of the generation and relaxation of photocurrents in TIs. Due to the helical spin structure of the surface states, TIs are expected to show a unique response to the illumination by light. Motivated by experimental observations of surface photocurrents in the 3D TI Bi_2Se_3 [McIver et al., 2012; Duan et al., 2014] we analyzed the surface photocurrent in TIs generated by asymmetric excitations in momentum space. The surface Dirac electrons in TIs are helical, i.e., electron spin and momentum are locked perpendicular to each other such that each surface momentum corresponds to a unique spin direction. Circularly polarized light preferably interacts with spins that are either aligned or antialigned to the wavevector of the light. Obliquely incident circularly polarized light, exciting electrons within the surface Dirac cone, is thus expected to excite carriers asymmetrically in momentum space leading to a finite photocurrent. Changing the helicity of the light would change the sign of the induced current.

Motivated by this intuitive picture, we first studied the photocurrent response of TIs within a pure surface state model. We studied how photon absorption can lead to an asymmetric excited carrier distribution and thus a photocurrent. We surprisingly found that, within the pure surface model, minimal coupling between light and electrons does not induce a photocurrent. Even though the crystal symmetry of 3D TIs such as Bi_2Se_3 allows surface photocurrents, e.g., from the CPGE, a 2D surface model neglects the bulk and leads to a vanishing photocurrent. A current can, however, be induced by considering the small Zeeman coupling between light and electron spin and we analyzed the polarization dependence of the resulting photocurrents for arbitrary angles of incidence of the light. Since Zeeman coupling is required, these currents are very small and especially the helicity-dependent contribution is unlikely to be measurable in ex-

periment. Even including an external in-plane magnetic field, a finite photocurrent from pure orbital coupling requires various perturbations to the perfectly linear Dirac dispersion, such as warping and a finite band curvature.

Since we found that either Zeeman coupling or an external magnetic field is needed to induce a photocurrent within the pure surface state model, we also took into account the low-energy bulk states. While the photocurrent response of 3D TIs deep in the bulk is expected to vanish due to the crystal inversion symmetry and the spin-degeneracy of the bulk states should preclude a helicity-dependent current response, these arguments do not hold in the vicinity of the surface where inversion symmetry is broken. Indeed, experimental measurements of surface photocurrents used photon energies that exceeded the bulk band gap [McIver et al., 2012; Duan et al., 2014]. We included the low-energy bulk states within a four-band model [Liu et al., 2010; Zhang et al., 2009a] and found that obliquely incident light can indeed lead to excitations between surface and bulk states that occur asymmetrically in momentum space. An analysis of the polarization dependence of the resulting photocurrent revealed that it is helicity-dependent and vanishes for linearly polarized light. In the considered particle-hole symmetric model, the photocurrent has opposite sign for positive and negative Fermi energy and vanishes for a Fermi level directly at the Dirac point.

In order to provide a full analysis of the the photocurrent response of TI surface states we also studied current relaxation. In a clean system at very low temperatures electron-electron scattering should be the dominant relaxation mechanism, and we thus analyzed the effect of carrier-carrier scattering on the photocurrent response in linearly dispersing systems. We considered a single excited electron-hole pair and found remarkable results. For a positive Fermi energy a single scattering event actually increases the electron contribution to the current while the hole current decreases. The picture reverses for a negative Fermi energy and current is independent of electron-electron scattering for a Fermi level directly at the Dirac point. In the limit where the excited electron has completely relaxed under the constraint of momentum conservation, the amplification factor for a positive Fermi energy is as large as ϵ_1/ϵ_F, where ϵ_1 is the initial excitation energy. For small Fermi energies we found that the rate of change of the 'electron current' and the 'hole current' both scale as $\sim \epsilon_F$ but with opposite sign. This leads to the result that the relaxation of the total current is actually suppressed and the rate of change of the total current scales as $\sim \epsilon_F^{3/2}$. Microscopically, the current relaxation for a single excited electron or hole is governed by relaxation processes with small energy transfer. Due to the cancellation between

electron and hole contributions, however, the relaxation of the total current is dominated by scattering events with a large energy transfer $\sim \epsilon_1$ which is quite different from the case of energy relaxation of excited carriers [Song et al., 2013]. We also discussed how this surprising effect of current amplification might be measured in experiment and found that a direct observation in systems like graphene would require an ultrafast femtosecond time-resolution. Such a high time-resolution has already been achieved in optical measurements [Breusing et al., 2011; Sun et al., 2012; Brida et al., 2013] and observing the amplification effect in experiments might thus be possible.

Our findings can also be compared to experiment. Photocurrents have been observed on the surface of the 3D TI Bi_2Se_3 with laser energies larger than the bulk band gap which lead to photoexcitation processes between surface and bulk states [McIver et al., 2012; Duan et al., 2014]. While the experiments showed helicity-dependent as well as helicity-independent photocurrents with surface state origin, our analysis revealed only a helicity-dependent contribution. Quantitatively, this helicity-dependent current is several orders of magnitude larger than the helicity-dependent current from the pure surface state model. Nevertheless, it is only consistent with the experimental observation if we assume a momentum relaxation time of $\tau_k = 10$ ps which seems quite large. Reported spin relaxation times for Bi_2Se_3 are of the order of ~ 0.1 ps [Hsieh et al., 2011; Zhang and Wu, 2013].

We thus conclude that in order to fully explain the experimental observations one has to take into account other processes that might generate a photocurrent response. Bi_2Se_3 exhibits a second Dirac cone at around 1.8 eV [Sobota et al., 2013]. For a Fermi level in the bulk conduction band and a laser energy of 1.5 eV as used in the experiment [McIver et al., 2012], one might thus also induce transitions between the bulk conduction band and the second Dirac cone which could contribute to the photocurrent. In addition, even if excitations occur symmetrically in momentum space, possible asymmetric scattering processes might lead to a finite photocurrent. The linear photogalvanic effect occurs for symmetric excitations due to asymmetric scattering of carriers on phonons or defects [Ganichev and Prettl, 2003] and might be the origin for the helicity-independent surface contribution observed in experiment.

Higher order effects such as the photon drag effect, where current is induced by the transfer of momentum from photons to electrons, might also generate a helicity-dependent and -independent response in TIs. The so-called circular photon drag effect was observed in quantum well structures and attributed to an

interplay between spin-dependent excitation and subsequent asymmetric spin relaxation in spin-split bands that drives a current through the spin-galvanic effect [Shalygin et al., 2006]. On the surface of Bi_2Se_3 the necessary spin-splitting would be provided by the Dirac cone or possibly the spin-split bands of the 2DEG in the inversion layer. Recently, there have also been attempts to measure the photon drag effect in TIs [Onishi et al., 2014].

The 3D TI Bi_2Se_3 is also a good thermoelectric material and thermoelectric effects due to laser heating might be important. For graphene it was actually predicted [Song et al., 2011] and experimentally observed [Gabor et al., 2011] that under certain conditions thermoelectric currents can dominate the photoresponse. Photoexcitation with low pump fluence and energies below the optical phonon frequency can lead to efficient carrier multiplication and hot electrons.

Our analysis of how a single e-e scattering event affects the current also provides a way to combine the effect of e-e scattering with other processes such as electron-phonon or electron-impurity scattering. This way it is also possible to estimate the current relaxation dynamics in systems where other scattering mechanisms compete with e-e interactions. As we have shown, a photocurrent can also be generated by excitations from the Dirac cone into the bulk conduction band. It would thus also be interesting to study the relaxation dynamics including bulk contributions. While e-e scattering cannot relax current in quadratically dispersing systems, experimental evidence suggests a strong coupling between the bulk conduction band and the surface Dirac cone [Sobota et al., 2012]. Exciting electrons into the bulk leads to a long-lived surface-state population (> 10 ps) by subsequent relaxation of carriers from the bulk conduction band into the surface Dirac cone [Sobota et al., 2012]. It would be interesting to understand how this strong surface-bulk coupling affects the photocurrent response.

LIGHT POLARIZATION USING A $\lambda/4$ WAVEPLATE

In this section we will determine the electric field that passes through a $\lambda/4$ waveplate rotated at an angle α as illustrated in Fig. A.1. Consider an electric field that is linearly polarized along the x-axis. For simplicity we work with complex amplitudes and take the real part in the end, i.e.,

$$\mathcal{E} = E_0 e^{i\omega t} \hat{x}. \tag{A.1}$$

When passing through the waveplate the electric field components acquire a phase shift, described by a matrix

$$W_{\pi/4} = \begin{pmatrix} e^{i\frac{\pi}{4}} & 0 \\ 0 & e^{-i\frac{\pi}{4}} \end{pmatrix}. \tag{A.2}$$

Thus, after it has passed through the rotated quarter-wave plate, the complex electric field is given by

$$\begin{aligned} \mathcal{E}_\alpha &= R(-\alpha) W_{\pi/4} R(\alpha) \mathcal{E}_\alpha \\ &= \frac{E_0}{\sqrt{2}} e^{i\omega t} \begin{pmatrix} 1 + i\cos 2\alpha \\ -i\sin 2\alpha \end{pmatrix}, \end{aligned} \tag{A.3}$$

where we used

$$R(\alpha) = \begin{pmatrix} \cos\alpha & -\sin\alpha \\ \sin\alpha & \cos\alpha \end{pmatrix}. \tag{A.4}$$

For light obliquely incident onto the xy-plane, the wavevector is given by

$$\boldsymbol{q} = -q \begin{pmatrix} \sin\theta\cos\varphi \\ \sin\theta\sin\varphi \\ \cos\theta \end{pmatrix} \tag{A.5}$$

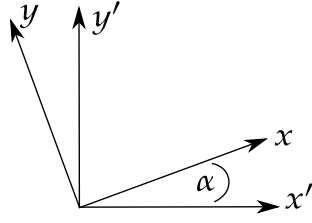Figure A.1: Coordinate systems of the electric field and the waveplate rotated by an angle α.

with polar angle θ from the z-axis and azimuthal angle φ from the x-axis. The corresponding complex electric field is found by applying a rotation around the y-axis followed by a rotation around the z-axis, i.e.,

$$
\begin{aligned}
\mathcal{E}'_\alpha &= R_z(\varphi)R_y(-\theta)\mathcal{E}_\alpha \\
&= \frac{E_0}{\sqrt{2}}e^{i\omega t}
\begin{pmatrix}
\cos\theta\cos\varphi(1+i\cos 2\alpha)+i\sin\varphi\sin 2\alpha \\
\cos\theta\sin\varphi(1+i\cos 2\alpha)-i\cos\varphi\sin 2\alpha \\
-(1+i\cos 2\alpha)\sin\theta.
\end{pmatrix},
\end{aligned}
\tag{A.6}
$$

where we used

$$
R_y(\theta) =
\begin{pmatrix}
\cos\theta & 0 & -\sin\theta \\
0 & 1 & 0 \\
\sin\theta & 0 & \cos\theta
\end{pmatrix}, \quad
R_z(\varphi) =
\begin{pmatrix}
\cos\varphi & -\sin\varphi & 0 \\
\sin\varphi & \cos\varphi & 0 \\
0 & 0 & 1
\end{pmatrix}.
\tag{A.7}
$$

The real electric field is then given by

$$
\mathcal{E}''_\alpha = E_0
\begin{pmatrix}
-\sin 2\alpha\sin\varphi\sin(\omega t)+\cos\theta\cos\varphi\left[\cos(\omega t)-\cos 2\alpha\sin(\omega t)\right] \\
\sin 2\alpha\cos\varphi\sin(\omega t)+\cos\theta\sin\varphi\left[\cos(\omega t)-\cos 2\alpha\sin(\omega t)\right] \\
\sin\theta\left[-\cos(\omega t)+\cos 2\alpha\sin(\omega t)\right]
\end{pmatrix}.
\tag{A.8}
$$

The real vector potential can be obtained using $\mathcal{E}=-\partial_t A$,

$$
A = \frac{A_0}{2}e^{-i\omega t}
\begin{pmatrix}
-\sin 2\alpha\sin\varphi-(i+\cos 2\alpha)\cos\theta\cos\varphi \\
\sin 2\alpha\cos\varphi-(i+\cos 2\alpha)\cos\theta\sin\varphi \\
(i+\cos 2\alpha)\sin\theta
\end{pmatrix} + c.c.,
\tag{A.9}
$$

where $c.c.$ denotes complex conjugation.

B

APPENDIX TO CHAPTER 4

In the main text, we presented the calculation of the photocurrent given by Eq. (4.10),

$$j = -\frac{4\pi e\tau_p}{\hbar}\sum_{p} v_{p,+}|\langle p,+|H'_{-}|p,-\rangle|^2\delta(2E - \hbar\omega), \tag{B.1}$$

for a specific angle of incidence of the light in the yz-plane. Here, we give the details of the calculation for arbitrary angles of incidence.

As in the main text, we start by studying the integrand $v_{p,+}|\langle p,+|H'_{-}|p,-\rangle|^2$. The velocity operator is independent of the specifics of the vector potential and we only need to consider the interaction Hamiltonian H' given by Eq. (4.18),

$$H' = -e\frac{\partial H}{\partial p}\cdot A - g_s\mu_B(\nabla \times A)\cdot\hat{\sigma}. \tag{B.2}$$

For the usual definitions of the azimuthal angle φ and the polar angle θ, the vector potential in spherical coordinates can be written as

$$A(t) = \frac{A_0}{2}e^{-i\omega t + iqr}(\hat{\boldsymbol{\varphi}} - i\hat{\boldsymbol{\theta}}) + c.c, \tag{B.3}$$

with

$$\hat{\boldsymbol{\varphi}} = \begin{pmatrix} -\sin\varphi \\ \cos\varphi \\ 0 \end{pmatrix}, \qquad \hat{\boldsymbol{\theta}} = \begin{pmatrix} \cos\theta\cos\varphi \\ \cos\theta\sin\varphi \\ -\sin\theta \end{pmatrix}. \tag{B.4}$$

Note that for the results obtained in the main text, we redefined $\varphi \to 3\pi/2 - \varphi$ so the light is incident in the yz-plane for $\varphi = 0$.

From this we can read off the orbital-coupling contribution to the interaction Hamiltonian,

$$\frac{\partial H}{\partial p_x} A_x(t) + \frac{\partial H}{\partial p_y} A_y(t) = \frac{1}{2}\big\{A_-\left[v_x(\hat{\varphi}_x - i\hat{\theta}_x) + v_y(\hat{\varphi}_y - i\hat{\theta}_y)\right] + c.c.\big\}$$

$$= \frac{1}{2}\big\{A_-\left[v_x(-\sin\varphi - i\cos\theta\cos\varphi)\right.$$

$$\left. +v_y(\cos\varphi - i\cos\theta\sin\varphi)\right] + c.c.\big\}, \qquad (B.5)$$

where again $v_x = \partial H/\partial p_x$, $v_y = \partial H/\partial p_y$, and $A_\pm = A_0 e^{\pm i\omega t}$.

Next we proceed with the Zeeman coupling and evaluate

$$\nabla \times \boldsymbol{A} = \frac{1}{2}\left[iA_-\boldsymbol{q} \times (\hat{\boldsymbol{\varphi}} - i\hat{\boldsymbol{\theta}}) + c.c.\right]$$

$$= \frac{1}{2}\left[-A_-q(\hat{\boldsymbol{\varphi}} - i\hat{\boldsymbol{\theta}}) + c.c.\right]$$

$$= -q\boldsymbol{A}, \qquad (B.6)$$

where in the second step we used that $\boldsymbol{q} = -q\hat{\boldsymbol{r}}$ with $\hat{\boldsymbol{r}}$ the position vector in spherical coordinates. Note that for right circularly polarized light we would get the opposite sign in the last line of Eq. (B.6), i.e., $\nabla \times \boldsymbol{A}_{\text{RCP}} = q\boldsymbol{A}_{\text{RCP}}$. With Eq. (B.6) the Zeeman coupling can be written as

$$(\nabla \times \boldsymbol{A}) \cdot \hat{\boldsymbol{\sigma}} = -\frac{q}{2}\big\{A_-\left[(\hat{\varphi}_x - i\hat{\theta}_x)\sigma_x + (\hat{\varphi}_y - i\hat{\theta}_y)\sigma_y - i\hat{\theta}_z\sigma_z\right] + c.c.\big\}$$

$$= -\frac{q}{2}\big\{A_-\left[(-\sin\varphi - i\cos\theta\cos\varphi)\sigma_x\right.$$

$$\left. +(\cos\varphi - i\cos\theta\sin\varphi)\sigma_y + i\sin\theta\sigma_z\right] + c.c.\big\}. \qquad (B.7)$$

Inserting Eqs. (B.5) and (B.7) into the interaction Hamiltonian given by Eq. (B.2), we obtain

$$H' = -\frac{e}{2}A_-\Big\{\left[v_x(-\sin\varphi - i\cos\theta\cos\varphi) + v_y(\cos\varphi - i\cos\theta\sin\varphi)\right]$$

$$- v_Z\left[\sigma_x(-\sin\varphi - i\cos\theta\cos\varphi) + \sigma_y(\cos\varphi - i\cos\theta\sin\varphi) + i\sin\theta\sigma_z)\right]\Big\}$$

$$+ c.c., \qquad (B.8)$$

where $v_Z = \frac{g_s\hbar\omega}{2mc}$.

The calculation then proceeds as presented in the main text. The interaction Hamiltonian given by Eq. (B.8) is inserted into the expression for the photocurrent given by Eq. (B.1) and the integral can be evaluated analogously to the analysis given in the main text.

APPENDIX TO CHAPTER 5

C.1 COEFFICIENTS OF THE SURFACE WAVEFUNCTION

The surface wavefunctions and bulk wavefunctions near the surface have to obey the boundary conditions given by Eqs. (5.8) and (5.9) in the main text and rewritten here for convenience,

$$\Psi^L(z=0) = \Psi^R(z=0) \qquad \text{and} \qquad \left.\frac{d\Psi^L}{dz}\right|_{z=0} = \left.\frac{d\Psi^R}{dz}\right|_{z=0}. \qquad (C.1)$$

Inserting the general expression for the surface state wavefunction given by Eqs. (5.12)-(5.16) into the boundary conditions, with the condition that $E_S = \pm A_0 k$, we find the following coefficients

$$a_S^R = -\eta_{S,\uparrow\downarrow}^L(\lambda_{S,+}^L)\left(\lambda_{S,-}^L + \lambda_{S,-}^R\right) + \eta_{S,\uparrow\downarrow}^L(\lambda_{S,-}^L)\left(\lambda_{S,+}^L + \lambda_{S,-}^R\right) + \lambda_{S,-}^L - \lambda_{S,+}^L \tag{C.2}$$

$$b_S^R = \eta_{S,\uparrow\downarrow}^L(\lambda_{S,+}^L)\left(\lambda_{S,-}^L + \lambda_{S,+}^R\right) - \eta_{S,\uparrow\downarrow}^L(\lambda_{S,-}^L)\left(\lambda_{S,+}^L + \lambda_{S,+}^R\right) + \lambda_{S,+}^L - \lambda_{S,-}^L$$
$$= -a_S^R(\lambda_{S,-}^R \leftrightarrow \lambda_{S,+}^R) \tag{C.3}$$

$$a_S^L = \left(1 - \eta_{S,\uparrow\downarrow}^L(\lambda_{S,-}^L)\right)\left(\lambda_{S,+}^R - \lambda_{S,-}^R\right) \tag{C.4}$$

$$b_S^L = -\left(1 - \eta_{S,\uparrow\downarrow}^L(\lambda_{S,+}^L)\right)\left(\lambda_{S,+}^R - \lambda_{S,-}^R\right)$$
$$= -a_S^L(\lambda_{S,-}^L \leftrightarrow \lambda_{S,+}^L), \tag{C.5}$$

where

$$\eta_{S,\uparrow\downarrow}^{L/R}(\lambda) = \frac{\pm A_0 k_\parallel - B_0\lambda}{E_S - M_0^{L/R} + \lambda^2 M_1} \tag{C.6}$$

is the first component of the spinor $\chi_{S,\uparrow\downarrow}^{L/R}$ given by Eq. (5.16) in the main text.

C.2 COEFFICIENTS OF THE BULK WAVEFUNCTION

In order to obtain the coefficients of the bulk wavefunctions given by Eqs. (5.22)-(5.26), we need to use that the wavefunction also obeys probability current conservation which requires $|b_B^R|^2 = |c_B^R|^2$. In combination with the boundary conditions given by Eqs. (5.8) and (5.9) in the main text, we can solve for the coefficients and obtain

$$
\begin{aligned}
a_B^R = & \left[\lambda_{S,+}^L \eta_{B,\uparrow\downarrow}^L(\lambda_{S,+}^L)\left(\lambda_{S,-}^L - ik_z\right) + \lambda_{S,-}^L \eta_{B,\uparrow\downarrow}^L(\lambda_{S,-}^L)\left(ik_z - \lambda_{S,+}^L\right)\right. \\
& \left. - ik_z \eta_{B,\uparrow\downarrow}^R(ik_z)\left(\lambda_{S,-}^L - \lambda_{S,+}^L\right)\right]\left[-\eta_{B,\uparrow\downarrow}^L(\lambda_{S,-}^L)\left(\lambda_{S,+}^L + ik_z\right)\right. \\
& \left. + \eta_{B,\uparrow\downarrow}^L(\lambda_{S,+}^L)\left(\lambda_{S,-}^L + ik_z\right) + \eta_{B,\uparrow\downarrow}^R(-ik_z)\left(\lambda_{S,-}^L - \lambda_{S,+}^L\right)\right] \\
& - (ik_z \leftrightarrow -ik_z),
\end{aligned}
$$ (C.7)

$$
\begin{aligned}
b_B^R = & \left[-\lambda_{S,-}^L \eta_{B,\uparrow\downarrow}^L(\lambda_{S,-}^L)\left(\lambda_{S,+}^L + ik_z\right) + \lambda_{S,+}^L \eta_{B,\uparrow\downarrow}^L(\lambda_{S,+}^L)\left(\lambda_{S,-}^L + ik_z\right)\right. \\
& \left. + ik_z \eta_{B,\uparrow\downarrow}^R(-ik_z)\left(\lambda_{S,-}^L - \lambda_{S,+}^L\right)\right]\left[-\eta_{B,\uparrow\downarrow}^L(\lambda_{S,-}^L)\left(\lambda_{S,+}^L + \lambda_{S,+}^R\right)\right. \\
& \left. + \eta_{B,\uparrow\downarrow}^L(\lambda_{S,+}^L)\left(\lambda_{S,-}^L + \lambda_{S,+}^R\right) - \eta_{B,\uparrow\downarrow}^R(-\lambda_{S,+}^R)\left(\lambda_{S,-}^L - \lambda_{S,+}^L\right)\right] \\
& - (\lambda_{S,+}^R \leftrightarrow ik_z),
\end{aligned}
$$ (C.8)

and

$$
a_B^L = \frac{a_B^R\left(\lambda_{S,-}^L + \lambda_{S,+}^R\right) + b_B^R\left(\lambda_{S,-}^L - ik_z\right) - (b_B^R)^*\left(\lambda_{S,-}^L + ik_z\right)}{\lambda_{S,-}^L - \lambda_{S,+}^L}
$$ (C.9)

$$
b_B^L = \frac{-a_B^R\left(\lambda_{S,+}^L + \lambda_{S,+}^R\right) - b_B^R\left(\lambda_{S,+}^L - ik_z\right) + (b_B^R)^*\left(\lambda_{S,+}^L + ik_z\right)}{\lambda_{S,-}^L - \lambda_{S,+}^L}
$$ (C.10)

where

$$
\eta_{B,\uparrow\downarrow}^{L/R}(\lambda) = \frac{\pm A_0 k_\parallel - B_0 \lambda}{E_B - M_0^{L/R} + \lambda^2 M_1}.
$$ (C.11)

The bulk energy E_B is given by Eq. (5.28) in the main text.

D

D.1 ANALYSIS OF KINEMATIC CONSTRAINTS

Here, we present an analogous argument to the one in the main text, showing that a single e-e scattering event leads to a current decrease in the case of $\epsilon_F < 0$ for a single highly excited electron in the conduction band. For a negative Fermi energy, the excited electron scatters off an electron in the Fermi sea in the valence band. We have shown in the main text, that in this case scattering processes only affect the current if the final electrons occupy states in different bands. Otherwise the scattering event is collinear and the current remains unchanged. The scattering process that we need to consider is illustrated in Fig. D.1 (a), i.e., $(+,-) \to (+,-)$. Written in the following way

$$k_1 + k_2' = k_1' + k_2 \tag{D.1}$$

$$\boldsymbol{k}_1 - \boldsymbol{k}_2' = \boldsymbol{k}_1' - \boldsymbol{k}_2, \tag{D.2}$$

the energy and momentum conservation condition can again be interpreted by an ellipse as illustrated in Fig. D.1 (b). Note that the position and orientation of vectors $\boldsymbol{k}_2$ and $\boldsymbol{k}_2'$ are different from Fig. 6.3 in the main text. Pauli's principle requires $k_2' < k_F \leq k_2$ such that the point of connection of $\boldsymbol{k}_1$ and $\boldsymbol{k}_2'$ has to lie inside the green dashed circle while the point of connection of $\boldsymbol{k}_1'$ and $\boldsymbol{k}_2$ has to lie outside the circle [see Fig. D.1 (b)]. The initial and final currents along $\hat{\mu}_{\parallel}(\boldsymbol{k}_2')$ that we need to compare are

$$j_i = \cos\phi_1 \tag{D.3}$$

$$j_f = \cos\phi_1' - \cos\phi_2' + \cos\phi_2, \tag{D.4}$$

such that we have to compare $\cos\phi_1' + \cos\phi_2$ and $\cos\phi_1 + \cos\phi_2'$, to see whether the current increases or decreases due to an e-e scattering event. Analogous to
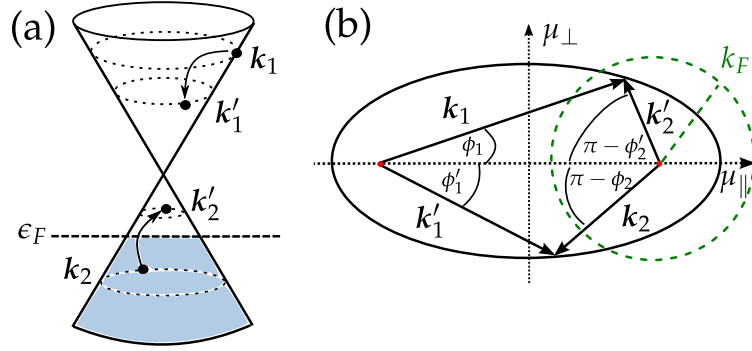
Figure D.1: (a) Schematic illustration of a scattering process where an excited electron relaxes by creating an electron-hole pair for $\epsilon_F < 0$. Scattering processes where the final states k'_1 and k'_2 are both in the same band, i.e., both either in the conduction or valence band, have to be collinear and do not change the current. (b) As for the case of $\epsilon_F > 0$, the allowed scattering processes can be represented by an ellipse. Now, $|k_1 - k'_2|$ is the distance between the focal points and $(k_1 + k'_2)/2$ defines the length of the semi-major axis. The green dashed circle again indicates the Fermi momentum. Because of Pauli's principle we have $k'_2 < k_F \leq k_2$.

the argument in the main text, it can be shown by simple geometry that for this particular ellipse $j_f - j_i \leq 0$ for any scattering event. Therefore the current decreases along $\hat{\mu}_\parallel$. Analogous to the argument for the case of $\epsilon_F > 0$, averaging over all ellipses, i.e., over all k'_2, leads to a current decrease due to e-e scattering for $\epsilon_F < 0$.

D.2 EVALUATION OF THE ENERGY CONSERVATION δ-FUNCTION

We first introduce the momentum transfer $q = k_1 - k'_1 = k'_2 - k_2$. Then the energy conservation δ-function can be written as

$$\delta(\epsilon_{k_1} + \epsilon_{k_2} - \epsilon_{k_1-q} - \epsilon_{k_2+q}) = \frac{1}{\hbar v_F} \int dp\, \delta(k_1 - |k_1 - q| - p)$$
$$\times \delta(|k_2 + q| - k_2 - p), \qquad (D.5)$$

where $\hbar v_F p$ is the difference between the energy of the initial and final scattering states. Using the relation $\delta(a - b) = 2a\delta(a^2 - b^2)$ with $a, b > 0$, we can write

$$
\delta(k_1 - |\boldsymbol{k}_1 - \boldsymbol{q}| - p) = 2(k_1 - p)\delta((k_1 - p)^2 - |\boldsymbol{k}_1 - \boldsymbol{q}|^2)
$$

$$
= \frac{(k_1 - p)}{k_1 q}\delta(\cos\phi_q - \frac{q^2 - p^2 + 2k_1 p}{2k_1 q})
$$

$$
\times \theta\left(1 - \left|\frac{q^2 - p^2 + 2k_1 p}{2k_1 q}\right|\right) \tag{D.6}
$$

where ϕ_q is the angle between $\boldsymbol{k}_1$ and $\boldsymbol{q}$, such that

$$
\int_0^{2\pi} d\phi_q f(\cos\phi_q)\delta(k_1 - |\boldsymbol{k}_1 - \boldsymbol{q}| - p)
$$

$$
= 2(k_1 - p)\int_0^{2\pi} d\phi_q f(\cos\phi_q)\delta(-2k_1 p + p^2 - q^2 + 2k_1 q \cos\phi_q)
$$

$$
= 2\frac{(k_1 - p)}{k_1 q}\frac{f\left(\frac{q^2 - p^2 + 2k_1 p}{2k_1 q}\right)}{\sqrt{1 - (\frac{q^2 - p^2 + 2k_1 p}{2k_1 q})^2}}\theta\left(1 - \left|\frac{q^2 - p^2 + 2k_1 p}{2k_1 q}\right|\right) \tag{D.7}
$$

where the factor of 2 comes from the fact that $\cos\phi - a$ has two zeroes in the interval $[0, 2\pi]$ with $|a| \leq 1$. Analogously, the ϕ_2-integration can be performed evaluating $\delta(|\boldsymbol{k}_2 + \boldsymbol{q}| - k_2 - p)$.

D.3   IDENTIFICATION OF DISTINCT SCATTERING PROCESSES

In this section, we identify the scattering processes that dominate the amplification or relaxation behavior of the current. We focus on the case of $\epsilon_F > 0$ and start with scattering processes of the excited electron, where we only need to consider processes like the one illustrated in Fig. D.2 (a). Here, the excited electron scatters off an electron in the Fermi sea in the conduction band. Other
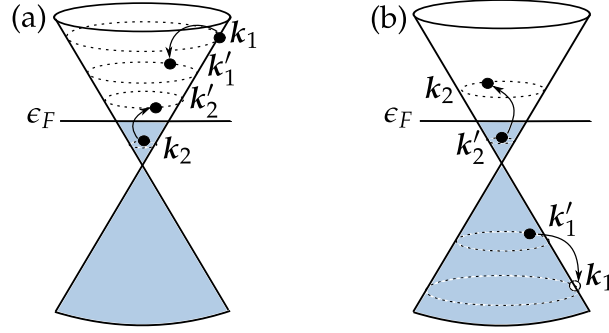
Figure D.2: Possible scattering process of (a) the excited electron and (b) the excited hole for the case of $\epsilon_F > 0$. (a) Scattering processes where the state k_2 is in the valence band are collinear and will not change the current. (b) Scattering processes where the states k_1' and k_2' are in the same band are also collinear.

allowed process will be collinear as shown in the main text and therefore do not affect the current. The rate of change of the electron current is then given by

$$
\frac{d\boldsymbol{j}^e}{dt} = -e\frac{1}{4L^4}\frac{2\pi}{\hbar}\left(\frac{e^2}{2\epsilon_0\epsilon}\right)^2 \sum_{k_2,k_2',k_1'} \delta(\epsilon_{k_1}+\epsilon_{k_2}-\epsilon_{k_1'}-\epsilon_{k_2'})\left(\hat{k}_1'+\hat{k}_2'-\hat{k}_1-\hat{k}_2\right)
$$

$$
\times \left|\frac{\langle k_1,+|k_1',+\rangle\langle k_2,+|k_2',+\rangle}{|k_1-k_1'|+q_{TF}} - \frac{\langle k_1,+|k_2',+\rangle\langle k_2,+|k_1',+\rangle}{|k_1-k_2'|+q_{TF}}\right|^2
$$

$$
\times \theta(\epsilon_F-\epsilon_{k_2})\theta(\epsilon_{k_2'}-\epsilon_F)\theta(\epsilon_{k_1'}-\epsilon_F)
$$

$$
= -e\frac{1}{4L^4}\frac{2\pi}{\hbar}\left(\frac{e^2}{2\epsilon_0\epsilon}\right)^2 \sum_{k_2,k_2',k_1'} \delta(\epsilon_{k_1}+\epsilon_{k_2}-\epsilon_{k_1'}-\epsilon_{k_2'})\left(\hat{k}_1'+\hat{k}_2'-\hat{k}_1-\hat{k}_2\right)
$$

$$
\times \left(\left|M_d^e - M_{ex}^e\right|^2\right)\theta(\epsilon_F-\epsilon_{k_2})\theta(\epsilon_{k_2'}-\epsilon_F)\theta(\epsilon_{k_1'}-\epsilon_F), \tag{D.8}
$$

with

$$
M_d^e = \frac{\langle k_1,+|k_1',+\rangle\langle k_2,+|k_2',+\rangle}{|k_1-k_1'|+q_{TF}}, \tag{D.9}
$$

$$
M_{ex}^e = \frac{\langle k_1,+|k_2',+\rangle\langle k_2,+|k_1',+\rangle}{|k_1-k_2'|+q_{TF}}, \tag{D.10}
$$

the 'direct' and 'exchange' part of the interaction matrix element, respectively. The sum is over states with positive energy only. One can see that the contributions from $|M_d^e|^2$ and $|M_{ex}^e|^2$ are equal, when switching the labels $k_1' \leftrightarrow k_2'$ in one of the two terms. We name the contributions to the rate of change of the current accordingly, i.e., $d\boldsymbol{j}_d^e/dt$ and $d\boldsymbol{j}_{ex}^e/dt$, respectively, with $d\boldsymbol{j}_d^e/dt = d\boldsymbol{j}_{ex}^e/dt$. The remaining contribution from the interference term proportional to $2Re[M_d^e(M_{ex}^e)^*]$, we call $d\boldsymbol{j}_{inter}^e/dt$.

Studying the hole current, we only need to consider processes like the one illustrated in Fig. D.2 (b). The excited hole can either recombine with an electron in the valence band, exciting an electron from the conduction band to above the Fermi energy, or the hole can recombine with an electron in the conduction band, exciting an electron from the valence band to above the Fermi energy. Processes where the states $|k'_1\rangle$, $|k'_2\rangle$ are in the same band are collinear and thus do not change the current. The rate of change of the hole current can be written as

$$\frac{dj^h}{dt} = 2e \frac{1}{4L^4} \frac{2\pi}{\hbar} \left(\frac{e^2}{2\epsilon_0 \epsilon}\right)^2 \sum_{k_2, k'_2, k'_1} \delta(\epsilon_{k_1} + \epsilon_{k_2} - \epsilon_{k'_1} - \epsilon_{k'_2}) \left(-\hat{k}'_1 + \hat{k}'_2 + \hat{k}_1 - \hat{k}_2\right)$$

$$\times \left| \frac{\langle k_1, -|k'_1, -\rangle \langle k_2, +|k'_2, +\rangle}{|k_1 - k'_1| + q_{TF}} - \frac{\langle k_1, -|k'_2, +\rangle \langle k_2, +|k'_1, -\rangle}{|k_1 - k'_2| + q_{TF}} \right|^2$$

$$\times \, \theta(\epsilon_{k_2} - \epsilon_F)\theta(\epsilon_F - \epsilon_{k'_2})$$

$$= 2e \frac{1}{4L^4} \frac{2\pi}{\hbar} \left(\frac{e^2}{2\epsilon_0 \epsilon}\right)^2 \sum_{k_2, k'_2, k'_1} \delta(\epsilon_{k_1} + \epsilon_{k_2} - \epsilon_{k'_1} - \epsilon_{k'_2}) \left(-\hat{k}'_1 + \hat{k}'_2 + \hat{k}_1 - \hat{k}_2\right)$$

$$\times \left(|M^h_d - M^h_{ex}|^2 \right) \theta(\epsilon_{k_2} - \epsilon_F)\theta(\epsilon_F - \epsilon_{k'_2}), \tag{D.11}$$

with

$$M^h_d = \frac{\langle k_1, -|k'_1, -\rangle \langle k_2, +|k'_2, +\rangle}{|k_1 - k'_1| + q_{TF}}, \tag{D.12}$$

$$M^h_{ex} = \frac{\langle k_1, -|k'_2, +\rangle \langle k_2, +|k'_1, -\rangle}{|k_1 - k'_2| + q_{TF}}. \tag{D.13}$$

The sum is restricted to $\epsilon_{k'_1} < 0$ and $\epsilon_{k'_2} > 0$ and the additional factor of 2 in front accounts for the other half of the sum. Analogous to the electron case we, name the first part of the interaction matrix element 'direct' and the second 'exchange'. The contributions to the rate of change of the current are named accordingly, i.e, dj^h_d/dt and dj^h_{ex}/dt, and dj^h_{inter}/dt for the interference term, analogous to the electron case. Here the 'direct' and 'exchange' terms are not equal since the states $|k'_1\rangle$ and $|k'_2\rangle$ are in different bands. Simply switching the labels does not transform one term into the other.

In the next section, we analyze the asymptotic behavior of the rate of change of the current, i.e., the behavior in the limit of large excitation energies, i.e., $\epsilon_F/\epsilon_1 \ll 1$. To lowest order we find that

$$\frac{dj^e_d}{dt} + \frac{dj^e_{ex}}{dt} \approx -\frac{dj^h_d}{dt}, \tag{D.14}$$

$$\frac{dj^e_{\text{inter}}}{dt} \approx -\frac{dj^h_{\text{inter}}}{dt}. \tag{D.15}$$

When combining the electron and hole contributions to study the current associated with the excited electron-hole pair, there are significant cancellations. To leading order the rate of the change of the total current is just given by

$$\frac{d\boldsymbol{j}^{\text{tot}}}{dt} = \frac{d\boldsymbol{j}^e}{dt} + \frac{d\boldsymbol{j}^h}{dt} \approx \frac{d\boldsymbol{j}^h_{ex}}{dt}.$$ (D.16)

$d\boldsymbol{j}^h_{ex}/dt$ is governed by the interaction matrix element

$$|M^h_{ex}|^2 = \left| \frac{\langle \boldsymbol{k}_1, -|\boldsymbol{k}'_2, +\rangle \langle \boldsymbol{k}_2, +|\boldsymbol{k}'_1, -\rangle}{|\boldsymbol{k}_1 - \boldsymbol{k}'_2| + q_{TF}} \right|^2,$$ (D.17)

which describes processes in which the excited hole recombines with an electron from the conduction band, exciting an electron from the valence band above the Fermi energy [see Fig. D.2 (b)]. These scattering processes obviously involve large energy transfers which are of the order of the initial excitation energy ϵ_1. To leading order, the rate of change of the photocurrent associated with an excited electron-hole pair is therefore governed by scattering processes with large energy transfer of the order of ϵ_1.

D.4 ASYMPTOTIC BEHAVIOR OF THE RATE OF CHANGE OF THE CURRENT

In this section, we calculate the asymptotic behavior of the rate of change of the current in the limit of large excitation energies $\epsilon_1/\epsilon_F \gg 1$. We discuss the individual electron and hole currents as well as the total current. We show in detail the calculation for $d\boldsymbol{j}^e_d/dt$ [see App. D.3] while the calculation of the remaining contributions follows analogously.

We thus need to evaluate $d\boldsymbol{j}^e_d/dt$ [see Eq. (D.8)]. As written in the main text, we first introduce the momentum transfer $\boldsymbol{q} = \boldsymbol{k}_1 - \boldsymbol{k}'_1 = \boldsymbol{k}'_2 - \boldsymbol{k}_2$. The Coulomb interaction is is proportional to $\sim 1/(q + q_{TF})$ and the 'direct' term will be dominated by scattering processes with small momentum transfer $q \ll k_1$. We fix the initial momentum of the excited electron-hole pair $\boldsymbol{k}_1$ such that the initial current is given by $\boldsymbol{j}_0 = -2ev_F\hat{\boldsymbol{k}}_1$. As written in the main text, we can now approximate

$$\hat{\boldsymbol{k}}'_1 - \hat{\boldsymbol{k}}_1 = \frac{k_1 - q\cos\phi_q}{|\boldsymbol{k}_1 - \boldsymbol{q}|} - 1 \approx 0$$ (D.18)

and

$$|\langle \boldsymbol{k}_1|\boldsymbol{k}'_1\rangle|^2 = \frac{k_1 - q\cos\phi_q + |\boldsymbol{k}_1 - \boldsymbol{q}|}{2|\boldsymbol{k}_1 - \boldsymbol{q}|} \approx 1.$$ (D.19)

Due to the rotational symmetry of the problem the initial and final currents flow along the same axis defined by $\hat{\jmath}_0$. Thus the rate of change of the current also points along this axis and we can write

$$\frac{dj_d^e}{dt} + \frac{dj_{ex}^e}{dt} = -ev_F \frac{1}{2L^4} \frac{2\pi}{\hbar} \left(\frac{e^2}{2\epsilon_0 \epsilon} \right)^2 \sum_{k_2, q} \frac{1}{\hbar v_F} \delta(k_1 + k_2 - |\boldsymbol{k}_1 - \boldsymbol{q}| - |\boldsymbol{k}_2 + \boldsymbol{q}|)$$

$$\times \left(\frac{k_2 \cos(\phi_2 + \phi_q) + q \cos \phi_q}{|\boldsymbol{k}_2 + \boldsymbol{q}|} - \cos(\phi_2 + \phi_q) \right)$$

$$\times \left(\frac{k_2 + q \cos \phi_2 + |\boldsymbol{k}_2 + \boldsymbol{q}|}{2|\boldsymbol{k}_2 + \boldsymbol{q}|(q + \alpha k_F)^2} \right) \theta(k_F - k_2)\theta(|\boldsymbol{k}_2 + \boldsymbol{q}| - k_F), \quad \text{(D.20)}$$

where $\alpha = e^2/(4\pi \hbar v_F \epsilon_0 \epsilon)$ is defined by $q_{\mathrm{TF}} = \alpha k_F$. The ϕ_2 and ϕ_q integrals can be evaluated using the identity

$$\delta(k_1 + k_2 - |\boldsymbol{k}_1 - \boldsymbol{q}| - |\boldsymbol{k}_2 + \boldsymbol{q}|) = \int dp\, \delta(k_1 - |\boldsymbol{k}_1 - \boldsymbol{q}| - p)\delta(|\boldsymbol{k}_2 + \boldsymbol{q}| - k_2 - p)$$

$$\text{(D.21)}$$

as shown in Eqs. (D.6) and (D.7). In Eq. (D.20), however, in addition to terms with $\cos \phi_2$ and $\cos \phi_q$ there are also terms that contain $\sin \phi_2 \sin \phi_q$. Depending on the values of ϕ_2 and ϕ_q, we can write

$$\sin \phi_2 \sin \phi_q = \pm \sqrt{1 - \cos^2 \phi_2} \sqrt{1 - \cos^2 \phi_q}. \qquad \text{(D.22)}$$

We have to integrate both ϕ_2 and ϕ_q from 0 to 2π, and we see that the integration of the terms proportional to $\sin \phi_2 \sin \phi_q$ gives zero. Thus, in the integrand of Eq. (D.20) we can neglect the terms proportional to $\sin \phi_2 \sin \phi_q$, leaving us with a function that only depends on $\cos \phi_2$ and $\cos \phi_q$. Evaluating the ϕ_2 and ϕ_q integrals using Eq. (D.7) and simplifying the result, yields

$$\frac{dj_d^e}{dt} + \frac{dj_{ex}^e}{dt} = -ev_F \frac{1}{2} \frac{2\pi}{\hbar} \left(\frac{e^2}{2\epsilon_0 \epsilon} \right)^2 \frac{1}{\hbar v_F} \frac{1}{(2\pi)^4}$$

$$\times \left(\int_0^{k_F} dp \int_{k_F - p}^{k_F} dk_2 + \int_{k_F}^{k_1 - k_F} dp \int_0^{k_F} dk_2 \right) \int_p^{2k_2 + p} dq\, (k_1 - p)$$

$$\times \frac{\sqrt{(2k_2 + p)^2 - q^2}}{\sqrt{(2k_1 - p)^2 - q^2}} \left(\frac{q^2 - p^2 + 2k_1 p}{k_1 q} \right) \frac{1}{(q + \alpha k_F)^2} \frac{(2k_2 + p)}{k_2(k_2 + p)}$$

$$= I_{p \ll k_1} + I_{p \sim k_1}. \qquad \text{(D.23)}$$

Notice that we split the integral over p into a part for small $p \leq k_F$, $I_{p \ll k_1}$, and a part for large p, $I_{p \sim k_1}$. For the integral over small we have $p \ll k_1$, and we

can approximate the integrand further. Introducing dimensionless parameters $\bar{p} = p/k_F$, $\bar{q} = q/k_F$, and $\bar{k}_2 = k_2/k_F$ and shifting the integration variable $k_2 \to k_2 + p/2$, we obtain

$$
\begin{aligned}
I_{p \ll k_1} &= -\frac{D}{4\pi}\frac{\epsilon_F}{\epsilon_1} \int_0^1 d\bar{p} \int_{1-\bar{p}/2}^{1+\bar{p}/2} d\bar{k}_2 \int_{\bar{p}}^{2\bar{k}_2} d\bar{q} \sqrt{(2\bar{k}_2)^2 - \bar{q}^2} \left(\frac{\bar{p}}{\bar{q}}\right) \frac{1}{(\bar{q}+\alpha)^2} \frac{2\bar{k}_2}{\bar{k}_2^2 - \frac{\bar{p}^2}{4}} \\
&\approx -\gamma \frac{D}{4\pi}\frac{\epsilon_F}{\epsilon_1}.
\end{aligned} \tag{D.24}
$$

with $\gamma \approx 1.17$ from numerical integration, $D = ev_F\alpha^2\epsilon_1/\hbar$ and $\alpha = 0.1$ as in the main text.

The remaining integral over large p contains contributions with $p \sim k_1$. If this integral converges, the integrand has to go to zero faster than $1/p$. If this is true, than we can neglect the contributions from large p and are still allowed to use the approximation $p \ll k_1$. With the same dimensionless parameters $\bar{p}$, $\bar{q}$, and $\bar{k}_2$ as above, the integral becomes

$$
\begin{aligned}
I_{p \sim k_1} &= -\frac{D}{4\pi}\frac{\epsilon_F}{\epsilon_1} \int_1^{k_1/k_F-1} dp \int_0^1 d\bar{k}_2 \int_{\bar{p}}^{2\bar{k}_2+\bar{p}} dq \sqrt{2p} \sqrt{2\bar{k}_2 + \bar{p} - \bar{q}} \left(\frac{\bar{p}}{\bar{q}}\right) \\
&\quad \times \frac{1}{(\bar{q}+\alpha)^2} \frac{(2\bar{k}_2+\bar{p})}{\bar{k}_2(\bar{k}_2+\bar{p})}.
\end{aligned} \tag{D.25}
$$

Since we are studying the limit of large excitation energies, we are interested in the limit $k_1/k_F \to \infty$. We avoid numerical integration up to infinity by using that for the region $p \gg k_2$ we can approximate $p \approx q$ and get

$$
\begin{aligned}
I_> &= -\frac{D}{4\pi}\frac{\epsilon_F}{\epsilon_1} \int_\Lambda^\infty d\bar{p} \int_0^1 d\bar{k}_2 \int_{\bar{p}}^{2\bar{k}_2+\bar{p}} d\bar{q} \sqrt{2\bar{p}} \sqrt{2\bar{k}_2 + \bar{p} - \bar{q}} \frac{1}{\bar{p}^2} \frac{1}{\bar{k}_2} \\
&= -\frac{D}{4\pi}\frac{8}{3}\frac{2}{3}\frac{\epsilon_F}{\epsilon_1} \int_\Lambda^\infty d\bar{p} \frac{1}{\bar{p}^{3/2}}.
\end{aligned} \tag{D.26}
$$

Λ is a cutoff that ensures that the approximation $p \gg k_2$ is valid. The remaining part of the integral cannot be approximated further and we have to numerically integrate

$$
\begin{aligned}
I_< &= -\frac{D}{4\pi}\frac{\epsilon_F}{\epsilon_1} \int_1^\Lambda d\bar{p} \int_0^1 d\bar{k}_2 \int_{\bar{p}}^{2\bar{k}_2+\bar{p}} d\bar{q} \sqrt{2\bar{p}} \sqrt{2\bar{k}_2 + \bar{p} - \bar{q}} \left(\frac{\bar{p}}{\bar{q}}\right) \\
&\quad \times \frac{1}{(\bar{q}+\alpha)^2} \frac{(2\bar{k}_2+\bar{p})}{\bar{k}_2(\bar{k}_2+\bar{p})}.
\end{aligned} \tag{D.27}
$$

Evaluating the remaining integrals for a cutoff $\Lambda > 10$, the result is independent of Λ,

$$\frac{dj_d^e}{dt} + \frac{dj_{ex}^e}{dt} \approx 4.2 \frac{D}{4\pi} \frac{\epsilon_F}{\epsilon_1} \hat{j}_0 \approx 0.3 e v_F \alpha^2 \frac{\epsilon_F}{\hbar} \hat{j}_0. \tag{D.28}$$

The asymptotic behavior of the 'interference' term can be obtained analogously and we find $\frac{dj_{inter}^e}{dt} \sim -D/(4\pi)(\epsilon_F/\epsilon_1)^{3/2}$, which is of higher order. Similarly the contributions for the hole can be determined.

To lowest order in ϵ_F/ϵ_1, $(dj_d^e/dt) + (dj_{ex}^e/dt)$ and (dj_d^h/dt) just differ by a sign. This can easily be seen by the following argument. In Fig. D.2 (b), labeling the initial states by k_1, k_2' and the final states by k_1', k_2, i.e., switching $k_2 \leftrightarrow k_2'$, and making use of the approximations (D.18) and (D.19), the direct term of the hole current can be written as

$$\frac{dj_d^h}{dt} \approx 2e \frac{1}{4L^4} \frac{2\pi}{\hbar} \left(\frac{e^2}{2\epsilon_0\epsilon} \right)^2 \sum_{k_2,k_2',k_1'} \delta(\epsilon_{k_1} + \epsilon_{k_2'} - \epsilon_{k_1'} - \epsilon_{k_2}) \left(\hat{k}_2 - \hat{k}_2' \right)$$

$$\times \left| \frac{\langle k_2', +|k_2, +\rangle}{|k_1 - k_1'| + q_{TF}} \right|^2 \theta(\epsilon_{k_2'} - \epsilon_F)\theta(\epsilon_F - \epsilon_{k_2}), \tag{D.29}$$

where $k_2' = k_2 - q$. The transformation $\phi_2 \to \phi_2 + \pi$, leads to $k_2 \to -k_2$ and $k_2 - q \to -(k_2 + q)$. With $|-k, \pm\rangle = |k, \mp\rangle$ and $|\langle k, +|k', +\rangle|^2 = |\langle k, -|k', -\rangle|^2$, we find to lowest order that

$$\frac{dj_d^h}{dt} = - \left(\frac{dj_d^e}{dt} + \frac{dj_{ex}^e}{dt} \right). \tag{D.30}$$

Analogous calculations to the one presented above for dj_d^e/dt lead to

$$\frac{dj_{inter}^e}{dt} \sim \frac{D}{4\pi} \left(\frac{\epsilon_F}{\epsilon_1} \right)^{3/2} \hat{j}_0$$

$$\frac{dj_{inter}^h}{dt} \sim -\frac{D}{4\pi} \left(\frac{\epsilon_F}{\epsilon_1} \right)^{3/2} \hat{j}_0$$

$$\frac{dj_{inter}^e}{dt} + \frac{dj_{inter}^h}{dt} \sim -\frac{D}{4\pi} \left(\frac{\epsilon_F}{\epsilon_1} \right)^{2} \hat{j}_0$$

$$\frac{dj_d^e}{dt} + \frac{dj_{ex}^e}{dt} + \frac{dj_d^h}{dt} \sim -\frac{D}{4\pi} \left(\frac{\epsilon_F}{\epsilon_1} \right)^{5/2} \hat{j}_0$$

$$\frac{dj_{ex}^h}{dt} \approx -\frac{D}{9} \left(\frac{\epsilon_F}{\epsilon_1} \right)^{3/2} \hat{j}_0. \tag{D.31}$$

For the rate of change of the total current, we thus find the asymptotic behavior in the limit $\epsilon_F \ll \epsilon_1$,

$$
\begin{aligned}
\frac{d\boldsymbol{j}^{(\text{tot})}}{dt} &= \frac{d\boldsymbol{j}_d^e}{dt} + \frac{d\boldsymbol{j}_{ex}^e}{dt} + \frac{d\boldsymbol{j}_d^h}{dt} - \left(\frac{d\boldsymbol{j}_{\text{inter}}^e}{dt} + \frac{d\boldsymbol{j}_{\text{inter}}^h}{dt} \right) + \frac{d\boldsymbol{j}_{ex}^h}{dt} \\
&\approx \frac{d\boldsymbol{j}_{ex}^h}{dt} + \mathcal{O}\left[\left(\frac{\epsilon_F}{\epsilon_1} \right)^2 \right] \\
&\approx -\frac{D}{9} \left(\frac{\epsilon_F}{\epsilon_1} \right)^{3/2} \hat{\boldsymbol{j}}_0 + \mathcal{O}\left[\left(\frac{\epsilon_F}{\epsilon_1} \right)^2 \right].
\end{aligned}
\tag{D.32}
$$

BIBLIOGRAPHY

Z. Alpichshev, J. G. Analytis, J.-H. Chu, I. R. Fisher, Y. L. Chen, Z. X. Shen, A. Fang, and A. Kapitulnik. *STM imaging of electronic waves on the surface of Bi_2Te_3: Topologically protected surface states and hexagonal warping effects*. Phys. Rev. Lett. **104**, 016401 (2010).

J. G. Analytis, J.-H. Chu, Y. Chen, F. Corredor, R. D. McDonald, Z. X. Shen, and I. R. Fisher. *Bulk fermi surface coexistence with dirac surface state in Bi_2Se_3: A comparison of photoemission and Shubnikov–de Haas measurements*. Phys. Rev. B **81**, 205407 (2010).

S. Basak, H. Lin, L. A. Wray, S.-Y. Xu, L. Fu, M. Z. Hasan, and A. Bansil. *Spin texture on the warped Dirac-cone surface states in topological insulators*. Phys. Rev. B **84**, 121401 (2011).

V. I. Belinicher and B. I. Sturman. *The photogalvanic effect in media lacking a center of symmetry*. Usp. Fiz. Nauk **130**, 415 (1980).

B. A. Bernevig, T. L. Hughes, and S.-C. Zhang. *Quantum spin Hall effect and topological phase transition in HgTe quantum wells*. Science **314**, 1757 (2006).

M. Bianchi, D. Guan, S. Bao, J. Mi, B. Brummerstedt Iversen, P. D. C. King, and P. Hofmann. *Coexistence of the topological state and a two-dimensional electron gas on the surface of Bi_2Se_3*. Nat. Commun. **1**, 128 (2010).

F. Bloch. *Über die Quantenmechanik der Elektronen in Kristallgittern*. Z. Phys. **52**, 555 (1929).

M. Breusing, S. Kuehn, T. Winzer, E. Malic, F. Milde, N. Severin, J. P. Rabe, C. Ropers, A. Knorr, and T. Elsaesser. *Ultrafast nonequilibrium carrier dynamics in a single graphene layer*. Phys. Rev. B **83**, 153410 (2011).

D. Brida, A. Tomadin, C. Manzoni, Y. J. Kim, A. Lombardo, S. Milana, R. R. Nair, K. S. Novoselov, A. C. Ferrari, G. Cerullo, and M. Polini. *Ultrafast collinear*

scattering and carrier multiplication in graphene. Nat. Commun. **4**, 1987 (2013).

N. P. Butch, K. Kirshenbaum, P. Syers, A. B. Sushkov, G. S. Jenkins, H. D. Drew, and J. Paglione. *Strong surface scattering in ultrahigh-mobility bi$_2$se$_3$ topological insulator crystals.* Phys. Rev. B **81**, 241301 (2010).

S. Butscher, F. Milde, M. Hirtschulz, E. Malic, and A. Knorr. *Hot electron relaxation and phonon dynamics in graphene.* Appl. Phys. Lett. **91**, 203103 (2007).

J. G. Checkelsky, Y. S. Hor, M.-H. Liu, D.-X. Qu, R. J. Cava, and N. P. Ong. *Quantum interference in macroscopic crystals of nonmetallic Bi$_2$Se$_3$.* Phys. Rev. Lett. **103**, 246601 (2009).

V. V. Cheianov and V. I. Fal'ko. *Friedel oscillations, impurity scattering, and temperature dependence of resistivity in graphene.* Phys. Rev. Lett. **97**, 226801 (2006).

J. Chen, H. J. Qin, F. Yang, J. Liu, T. Guan, F. M. Qu, G. H. Zhang, J. R. Shi, X. C. Xie, C. L. Yang, K. H. Wu, Y. Q. Li, and L. Lu. *Gate-voltage control of chemical potential and weak antilocalization in Bi$_2$Se$_3$.* Phys. Rev. Lett. **105**, 176602 (2010).

Y. L. Chen, J. G. Analytis, J.-H. Chu, Z. K. Liu, S.-K. Mo, X. L. Qi, H. J. Zhang, D. H. Lu, X. Dai, Z. Fang, S. C. Zhang, I. R. Fisher, Z. Hussain, and Z.-X. Shen. *Experimental realization of a three-dimensional topological insulator, Bi$_2$Te$_3$.* Science **325**, 178 (2009).

J. Duan, N. Tang, X. He, Y. Yan, S. Zhang, X. Qin, X. Wang, X. Yang, F. Xu, Y. Chen, W. Ge, and B. Shen. *Identification of helicity-dependent photocurrents from topological insulator surface states in Bi$_2$Se$_3$ gated by ionic liquid.* Sci. Rep. **4**, 4889 (2014).

L. Fu. *Hexagonal warping effects in the surface states of the topological insulator Bi$_2$Te$_3$.* Phys. Rev. Lett. **103**, 266801 (2009).

L. Fu and C. L. Kane. *Topological insulators with inversion symmetry.* Phys. Rev. B **76**, 045302 (2007).

L. Fu and C. L. Kane. *Superconducting proximity effect and Majorana fermions at the surface of a topological insulator.* Phys. Rev. Lett. **100**, 096407 (2008).

L. Fu, C. L. Kane, and E. J. Mele. *Topological insulators in three dimensions.* Phys. Rev. Lett. **98**, 106803 (2007).

N. M. Gabor, J. C. W. Song, Q. Ma, N. L. Nair, T. Taychatanapat, K. Watanabe, T. Taniguchi, L. S. Levitov, and P. Jarillo-Herrero. *Hot carrier-assisted intrinsic photoresponse in graphene.* Science **334**, 648 (2011).

S. D. Ganichev and W. Prettl. *Spin photocurrents in quantum wells.* J. Phys.: Condens. Matter **15**, R935 (2003).

I. Gierz, J. C. Petersen, M. Mitrano, C. Cacho, I. C. E. Turcu, E. Springate, A. Stör, K. Axel, U. Starke, and A. Cavalleri. *Snapshots of non-equilibrium Dirac carrier distributions in graphene.* Nature Mater. **12**, 1119 (2013).

D. Greenaway and G. Harbeke. *Band structure of bismuth telluride, bismuth selenide and their respective alloys.* J. Phys. Chem. Solids **26**, 1585 (1965).

M. Hajlaoui, E. Papalazarou, J. Mauchain, G. Lantz, N. Moisan, D. Boschetto, Z. Jiang, I. Miotkowski, Y. P. Chen, A. Taleb-Ibrahimi, L. Perfetti, and M. Marsi. *Ultrafast surface carrier dynamics in the topological insulator Bi_2Te_3.* Nano Lett. **12**, 3532 (2012).

F. D. M. Haldane. *Model for a quantum Hall effect without Landau levels: Condensed-matter realization of the "parity anomaly".* Phys. Rev. Lett. **61**, 2015 (1988).

B. I. Halperin. *Quantized hall conductance, current-carrying edge states, and the existence of extended states in a two-dimensional disordered potential.* Phys. Rev. B **25**, 2185 (1982).

M. Z. Hasan and C. L. Kane. *Colloquium: Topological insulators.* Rev. Mod. Phys. **82**, 3045 (2010).

E. Hecht. *Optics.* Addison Wesley, 3rd edition (1998).

P. Hosur. *Circular photogalvanic effect on topological insulator surfaces: Berry-curvature-dependent response.* Phys. Rev. B **83**, 035309 (2011).

D. Hsieh, D. Qian, L. Wray, Y. Xia, Y. S. Hor, R. J. Cava, and M. Z. Hasan. *A topological Dirac insulator in a quantum spin Hall phase.* Nature **452**, 970–974 (2008).

D. Hsieh, Y. Xia, D. Qian, L. Wray, J. H. Dil, F. Meier, J. Osterwalder, L. Patthey, J. G. Checkelsky, N. P. Ong, A. V. Fedorov, H. Lin, A. Bansil, D. Grauer, Y. S.

Hor, R. J. Cava, and M. Z. Hasan. *A tunable topological insulator in the spin helical Dirac transport regime*. Nature **460**, 1101 (2009a).

D. Hsieh, Y. Xia, D. Qian, L. Wray, F. Meier, J. H. Dil, J. Osterwalder, L. Patthey, A. V. Fedorov, H. Lin, A. Bansil, D. Grauer, Y. S. Hor, R. J. Cava, and M. Z. Hasan. *Observation of time-reversal-protected single-Dirac-cone topological-insulator states in Bi_2Te_3 and Sb_2Te_3*. Phys. Rev. Lett. **103**, 146401 (2009b).

D. Hsieh, F. Mahmood, J. W. McIver, D. R. Gardner, Y. S. Lee, and N. Gedik. *Selective probing of photoinduced charge and spin dynamics in the bulk and surface of a topological insulator*. Phys. Rev. Lett. **107**, 077401 (2011).

D. Huertas-Hernando, F. Guinea, and A. Brataas. *Spin-orbit coupling in curved graphene, fullerenes, nanotubes, and nanotube caps*. Phys. Rev. B **74**, 155426 (2006).

E. L. Ivchenko and S. D. Ganichev. *Spin-photogalvanics*. In M. Dyakonov, editor, *Spin Physics in Semiconductors*, volume 157 of Springer Ser. Solid-State Sci., pages 245–277. Springer Berlin Heidelberg (2008).

E. L. Ivchenko and G. E. Pikus. *Superlattices and Other Heterostructures. Symmetry and Optical Phenomena*. Springer Berlin Heidelberg (1997).

J. C. Johannsen, S. Ulstrup, F. Cilento, A. Crepaldi, M. Zacchigna, C. Cacho, I. C. E. Turcu, E. Springate, F. Fromm, C. Raidel, T. Seyller, F. Parmigiani, M. Grioni, and P. Hofmann. *Direct view of hot carrier dynamics in graphene*. Phys. Rev. Lett. **111**, 027403 (2013).

A. Junck, G. Refael, and F. v. Oppen. *Photocurrent response of topological insulator surface states*. Phys. Rev. B **88**, 075144 (2013).

A. Junck, G. Refael, and F. v. Oppen. *Current amplification and relaxation in Dirac systems*. Phys. Rev. B **90**, 245110 (2014).

C. L. Kane and E. J. Mele. *Quantum spin Hall effect in graphene*. Phys. Rev. Lett. **95**, 226801 (2005).

T. Karzig, L. I. Glazman, and F. v. Oppen. *Energy relaxation and thermalization of hot electrons in quantum wires*. Phys. Rev. Lett. **105**, 226407 (2010).

C. Kastl, T. Guan, X. Y. He, K. H. Wu, Y. Q. Li, and A. W. Holleitner. *Local photocurrent generation in thin films of the topological insulator Bi_2Se_3*. Appl. Phys. Lett. **101**, 251110 (2012).

C. Kastl, C. Karnetzky, H. Karl, and A. W. Holleitner. *Ultrafast helicity control of surface currents in topological insulators with near-unity fidelity*. arXiv:1501.07784 (2015a).

C. Kastl, P. Seifert, X. He, K. Wu, Y. Li, and A. W. Holleitner. *Chemical potential fluctuations in topological insulator $(Bi_{0.5}Sb_{0.5})_2Te_3$ films visualized by photocurrent spectroscopy*. arXiv:1501.07844 (2015b).

R. Kim, V. Perebeinos, and P. Avouris. *Relaxation of optically excited carriers in graphene*. Phys. Rev. B **84**, 075449 (2011).

K. v. Klitzing, G. Dorda, and M. Pepper. *New method for high-accuracy determination of the fine-structure constant based on quantized Hall resistance*. Phys. Rev. Lett. **45**, 494 (1980).

M. König, S. Wiedmann, C. Brüne, A. Roth, H. Buhmann, L. W. Molenkamp, X.-L. Qi, and S.-C. Zhang. *Quantum spin Hall insulator state in HgTe quantum wells*. Science **318**, 766 (2007).

N. Kumar, B. A. Ruzicka, N. P. Butch, P. Syers, K. Kirshenbaum, J. Paglione, and H. Zhao. *Spatially resolved femtosecond pump-probe study of topological insulator Bi_2Se_3*. Phys. Rev. B **83**, 235306 (2011).

R. B. Laughlin. *Quantized hall conductivity in two dimensions*. Phys. Rev. B **23**, 5632 (1981).

P. Lautenschlager, M. Garriga, L. Vina, and M. Cardona. *Temperature dependence of the dielectric function and interband critical points in silicon*. Phys. Rev. B **36**, 4821 (1987).

C.-X. Liu, X.-L. Qi, H. Zhang, X. Dai, Z. Fang, and S.-C. Zhang. *Model hamiltonian for topological insulators*. Phys. Rev. B **82**, 045122 (2010).

E. Malic, T. Winzer, E. Bobkin, and A. Knorr. *Microscopic theory of absorption and ultrafast many-particle kinetics in graphene*. Phys. Rev. B **84**, 205406 (2011).

J. W. McIver, D. Hsieh, H. Steinberg, P. Jarillo-Herrero, and N. Gedik. *Control over topological insulator photocurrents with light polarization*. Nature Nanotech. **7**, 96 (2012).

F. Meier and B. Zakharchenya. *Optical Orientation*. Elsevier (1984).

A. R. Mellnik, J. S. Lee, A. Richardella, J. L. Grab, P. J. Mintun, M. H. Fischer, A. Vaezi, A. Manchon, E.-A. Kim, N. Samarth, and D. C. Ralph. *Spin-transfer torque generated by a topological insulator*. Nature **511**, 449 (2014).

H. Min, J. E. Hill, N. A. Sinitsyn, B. R. Sahu, L. Kleinman, and A. H. MacDonald. *Intrinsic and Rashba spin-orbit interactions in graphene sheets*. Phys. Rev. B **74**, 165310 (2006).

M. Mittendorff, T. Winzer, E. Malic, A. Knorr, C. Berger, W. A. d. Heer, H. Schneider, M. Helm, and S. Winnerl. *Anisotropy of excitation and relaxation of photogenerated charge carriers in graphene*. Nano Lett. **14**, 1504 (2014).

J. E. Moore. *The birth of topological insulators*. Nature **464**, 194 (2010).

J. E. Moore. *Topological insulators: The next generation*. Nature Phys. **5**, 378 (2009).

M. Müller and S. Sachdev. *Collective cyclotron motion of the relativistic plasma in graphene*. Phys. Rev. B **78**, 115419 (2008).

Y. Onishi, Z. Ren, M. Novak, K. Segawa, Y. Ando, and K. Tanaka. *Real-time detection of photon drag surface currents in topological insulators*. arxiv:1403.2492v2 (2014).

S. R. Park, W. S. Jung, C. Kim, D. J. Song, C. Kim, S. Kimura, K. D. Lee, and N. Hur. *Quasiparticle scattering and the protected nature of the topological states in a parent topological insulator Bi_2Se_3*. Phys. Rev. B **81**, 041405 (2010).

H. Peng, K. Lai, D. Kong, S. Meister, Y. Chen, X.-L. Qi, S.-C. Zhang, Z.-X. Shen, and Y. Cui. *Aharonov-Bohm interference in topological insulator nanoribbons*. Nature Mater. **9**, 225 (2010).

H. Peng, W. Dang, J. Cao, Y. Chen, D. Wu, W. Zheng, H. Li, Z.-X. Shen, and Z. Liu. *Topological insulator nanostructures for near-infrared transparent flexible electrodes*. Nature Chem. **4**, 281 (2012).

T. Plötzing, T. Winzer, E. Malic, D. Neumaier, A. Knorr, and H. Kurz. *Experimental verification of carrier multiplication in graphene.* Nano Lett. **14**, 5371 (2014).

S. Raghu, S. B. Chung, X.-L. Qi, and S.-C. Zhang. *Collective modes of a helical liquid.* Phys. Rev. Lett. **104**, 116401 (2010).

V. Sandomirsky, A. V. Butenko, R. Levin, and Y. Schlesinger. *Electric-field-effect thermoelectrics.* J. Appl. Phys. **90**, 2370 (2001).

V. A. Shalygin, H. Diehl, C. Hoffmann, S. N. Danilov, T. Herrle, S. A. Tarasenko, D. Schuh, C. Gerl, W. Wegschneider, W. Prettl, and S. D. Ganichev. *Spin photocurrents and the circular photon drag effect in (110)-grown quantum well structures.* JETP Lett. **84**, 570 (2006).

W.-Y. Shan, H.-Z. Lu, and S.-Q. Shen. *Effective continuous model for surface states and thin films of three-dimensional topological insulators.* New J. Phys. **12**, 043048 (2010).

J. A. Sobota, S. Yang, J. G. Analytis, Y. L. Chen, I. R. Fisher, P. S. Kirchmann, and Z.-X. Shen. *Ultrafast optical excitation of a persistent surface-state population in the topological insulator Bi_2Se_3.* Phys. Rev. Lett. **108**, 117403 (2012).

J. A. Sobota, S.-L. Yang, A. F. Kemper, J. J. Lee, F. T. Schmitt, W. Li, R. G. Moore, J. G. Analytis, I. R. Fisher, P. S. Kirchmann, T. P. Devereaux, and Z.-X. Shen. *Direct optical coupling to an unoccupied Dirac surface state in the topological insulator Bi_2Se_3.* Phys. Rev. Lett. **111**, 136802 (2013).

J. C. W. Song. *(private communication)* (2014).

J. C. W. Song, M. S. Rudner, C. M. Marcus, and L. S. Levitov. *Hot carrier transport and photocurrent response in graphene.* Nano Lett. **11**, 4688 (2011).

J. C. W. Song, K. J. Tielrooij, F. H. L. Koppens, and L. S. Levitov. *Photoexcited carrier dynamics and impact-excitation cascade in graphene.* Phys. Rev. B **87**, 155429 (2013).

T. Stauber, N. M. R. Peres, and F. Guinea. *Electronic transport in graphene: A semiclassical approach including midgap states.* Phys. Rev. B **76**, 205423 (2007).

B. I. Sturman and V. M. Fridkin. *The Photovoltaic and Photorefractive Effects in Non-Centrosymmetric Materials.* Gordon and Breach New York (1992).

D. Sun, C. Divin, M. Mihnev, T. Winzer, E. Malic, A. Knorr, J. E. Sipe, C. Berger, W. A. d. Heer, P. N. First, and T. B. Norris. *Current relaxation due to hot carrier scattering in graphene.* New J. Phys. **14**, 105012 (2012).

S. Tani, F. Blanchard, and K. Tanaka. *Ultrafast carrier dynamics in graphene under a high electric field.* Phys. Rev. Lett. **109**, 166603 (2012).

A. A. Taskin and Y. Ando. *Quantum oscillations in a topological insulator $Bi_{1-x}Sb_x$.* Phys. Rev. B **80**, 085303 (2009).

K. J. Tielrooij, J. C. W. Song, S. A. Jensen, A. Centeno, A. Pesquera, A. Zurutuza Elorza, M. Bonn, L. S. Levitov, and F. H. L. Koppens. *Photoexcitation cascade and multiple hot-carrier generation in graphene.* Nature Phys. **9**, 248 (2013).

A. Tomadin, D. Brida, G. Cerullo, A. C. Ferrari, and M. Polini. *Nonequilibrium dynamics of photoexcited electrons in graphene: Collinear scattering, auger processes, and the impact of screening.* Phys. Rev. B **88**, 035430 (2013).

W.-K. Tse and S. Das Sarma. *Energy relaxation of hot Dirac fermions in graphene.* Phys. Rev. B **79**, 235406 (2009).

W.-K. Tse and A. H. MacDonald. *Giant magneto-optical Kerr effect and universal Faraday effect in thin-film topological insulators.* Phys. Rev. Lett. **105**, 057401 (2010).

Y. H. Wang, D. Hsieh, D. Pilon, L. Fu, D. R. Gardner, Y. S. Lee, and N. Gedik. *Observation of a warped helical spin texture in Bi_2Se_3 from circular dichroism Angle-Resolved photoemission spectroscopy.* Phys. Rev. Lett. **107**, 207602 (2011).

T. Winzer and E. Malic. *Impact of auger processes on carrier dynamics in graphene.* Phys. Rev. B **85**, 241404 (2012).

T. Winzer, A. Knorr, and E. Malic. *Carrier multiplication in graphene.* Nano Lett. **10**, 4839 (2010).

B. Wittmann, S. N. Danilov, V. V. Bel'kov, S. A. Tarasenko, E. G. Novik, H. Buhmann, C. Brüne, L. W. Molenkamp, Z. D. Kvon, N. N. Mikhailov, S. A. Dvoretsky, N. Q. Vinh, A. F. G. v. d. Meer, B. Murdin, and S. D. Ganichev. *Circular photogalvanic effect in HgTe/CdHgTe quantum well structures.* Semicond. Sci. Technol. **25**, 095005 (2010).

Y. Xia, D. Qian, D. Hsieh, L. Wray, A. Pal, H. Lin, A. Bansil, D. Grauer, Y. S. Hor, R. J. Cava, and M. Z. Hasan. *Observation of a large-gap topological-insulator class with a single Dirac cone on the surface*. Nature Phys. **5**, 398 (2009).

B. Yan, H.-J. Zhang, C.-X. Liu, X.-L. Qi, T. Frauenheim, and S.-C. Zhang. *Theoretical prediction of topological insulator in ternary rare earth chalcogenides*. Phys. Rev. B **82**, 161108 (2010).

Y. Yao, F. Ye, X.-L. Qi, S.-C. Zhang, and Z. Fang. *Spin-orbit gap of graphene: First-principles calculations*. Phys. Rev. B **75**, 041401 (2007).

O. V. Yazyev, J. E. Moore, and S. G. Louie. *Spin polarization and transport of surface states in the topological insulators Bi_2Se_3 andBi_2Te_3 from first principles*. Phys. Rev. Lett. **105**, 266806 (2010).

H. Zhang, C.-X. Liu, X.-L. Qi, X. Dai, Z. Fang, and S.-C. Zhang. *Topological insulators in Bi_2Se_3, Bi_2Te_3 and Sb_2Te_3 with a single Dirac cone on the surface*. Nature Phys. **5**, 438 (2009a).

H. Zhang, C.-X. Liu, and S.-C. Zhang. *Spin-orbital texture in topological insulators*. Phys. Rev. Lett. **111**, 066801 (2013).

P. Zhang and M. W. Wu. *Hot-carrier transport and spin relaxation on the surface of topological insulator*. Phys. Rev. B **87**, 085319 (2013).

T. Zhang, P. Cheng, X. Chen, J.-F. Jia, X. Ma, K. He, L. Wang, H. Zhang, X. Dai, Z. Fang, X. Xie, and Q.-K. Xue. *Experimental demonstration of topological surface states protected by time-reversal symmetry*. Phys. Rev. Lett. **103**, 266803 (2009b).

W. Zhang, R. Yu, H.-J. Zhang, X. Dai, and Z. Fang. *First-principles studies of the three-dimensional strong topological insulators Bi_2Te_3, Bi_2Se_3 and Sb_2Te_3*. New J. Phys. **12**, 065013 (2010a).

X. Zhang, J. Wang, and S.-C. Zhang. *Topological insulators for high-performance terahertz to infrared applications*. Phys. Rev. B **82**, 245107 (2010b).

Z.-H. Zhu, C. N. Veenstra, G. Levy, A. Ubaldini, P. Syers, N. P. Butch, J. Paglione, M. W. Haverkort, I. S. Elfimov, and A. Damascelli. *Layer-by-layer entangled spin-orbital texture of the topological surface state in Bi_2Se_3*. Phys. Rev. Lett. **110**, 216401 (2013).

ACKNOWLEDGMENTS

PUBLICATIONS

This thesis is based on the following publications:

- *Photocurrent response of topological insulator surface states*
  Phys. Rev. B **88**, 075144 (2013)
  http://dx.doi.org/10.1103/PhysRevB.88.075144
  A. Junck, G. Refael, and F. v. Oppen

- *Current amplification and relaxation in Dirac systems*
  Phys. Rev. B **90**, 245110 (2014)
  http://dx.doi.org/10.1103/PhysRevB.90.245110
  A. Junck, G. Refael, and F. v. Oppen

The following publication is unrelated to this thesis:

- *Transport through a disordered topological-metal strip*
  Phys. Rev. B **87**, 235114 (2013)
  A. Junck, K. W. Kim, D. L. Bergman, T. Pereg-Barnea, and G. Refael

CURRICULUM VITAE

For reasons of data protection,
the *curriculum vitae* is not included in the online version of this thesis.

ERKLÄRUNG

Hiermit versichere ich, dass ich die vorliegende Dissertation sebständig ange-
fertigt und hierfür keine anderen als die angegebenen Hilfsmittel und Hilfen
verwendet habe. Diese Arbeit ist weder in einem früheren Promotionsverfahren
angenommen noch als ungenügend bewertet worden.

Berlin, den 9. März 2015

<div style="text-align:right">

_____

Alexandra Junck

</div>